

University of Texas at Arlington

**MavMatrix**

---

Mechanical and Aerospace Engineering  
Dissertations

Mechanical and Aerospace Engineering  
Department

---

2023

## COMPLIANT ROBOT MANIPULATOR FOR TRANSURETHRAL DIAGNOSIS

Samson A. Adejokun

Follow this and additional works at: [https://mavmatrix.uta.edu/mechaerospace\\_dissertations](https://mavmatrix.uta.edu/mechaerospace_dissertations)



Part of the [Aerospace Engineering Commons](#), and the [Mechanical Engineering Commons](#)

---

### Recommended Citation

Adejokun, Samson A., "COMPLIANT ROBOT MANIPULATOR FOR TRANSURETHRAL DIAGNOSIS" (2023).  
*Mechanical and Aerospace Engineering Dissertations*. 313.  
[https://mavmatrix.uta.edu/mechaerospace\\_dissertations/313](https://mavmatrix.uta.edu/mechaerospace_dissertations/313)

This Dissertation is brought to you for free and open access by the Mechanical and Aerospace Engineering Department at MavMatrix. It has been accepted for inclusion in Mechanical and Aerospace Engineering Dissertations by an authorized administrator of MavMatrix. For more information, please contact [leah.mccurdy@uta.edu](mailto:leah.mccurdy@uta.edu), [erica.rousseau@uta.edu](mailto:erica.rousseau@uta.edu), [vanessa.garrett@uta.edu](mailto:vanessa.garrett@uta.edu).

COMPLIANT ROBOT MANIPULATOR FOR TRANSURETHRAL DIAGNOSIS

by

SAMSON ABIMBOLA ADEJOKUN

Presented to the Faculty of the Graduate School of  
The University of Texas at Arlington in Partial Fulfillment  
of the Requirements  
for the Degree of

DOCTOR OF PHILOSOPHY

THE UNIVERSITY OF TEXAS AT ARLINGTON

May 2023

Copyright © by SAMSON ABIMBOLA ADEJOKUN 2023

All Rights Reserved

To my father, Adesegun, and my mother, Omolara

for their sacrifice.

## ACKNOWLEDGEMENTS

I would like to thank my supervising professor Dr. Panayiotis S. Shiakolas for his invaluable guidance during the course of my doctoral studies. I wish to thank my committee members, Dr. Alan Bowling, Dr. Bo P. Wang, Dr. Christopher McMurrough, and Dr. Prashanth Ravi for their interest in my research and for taking the time to serve on my dissertation committee.

I would also like to extend my appreciation to the staff and faculty of the Mechanical Engineering department, University of Texas at Arlington for the various support I received during my doctoral studies. I wish to thank Mr. Rex Winfrey for his assistance in the manufacturing of designs used in my research and Ms. Wendy Ryan for her administrative assistance.

I am especially grateful to Tushar Saini and Rohanfor Bhandikeri for the helpful discussions and invaluable comments that contributed to the success of my research. I am also grateful to my MARS Lab family (Shashank Kumat, Sudip Hazra, Abdul Hafiz Abdul Rahaman)

Finally, I would like to express my deep gratitude to my wife for her friendship, the many encouragements, and support. I am extremely fortunate to have my father and mother who have encouraged and helped nurture my education and career ambitions by sacrificing their all. I also like to express my deepest gratitude to my brothers and sisters who have also done the same.

May 3, 2023

## ABSTRACT

### COMPLIANT ROBOT MANIPULATOR FOR TRANSURETHRAL DIAGNOSIS

SAMSON ABIMBOLA ADEJOKUN, Ph.D.

The University of Texas at Arlington, 2023

Supervising Professor: Dr. Panayiotis S. Shiakolas

Minimally invasive procedures employ continuum manipulators, however, the internal human anatomy presents challenges relating to size, dexterity, and workspace for these manipulators. This research presents modeling, kinematic analysis, limited prototyping, and characterization of a micro-robotic manipulator to assess viscoelastic tissue properties of the bladder through transurethral palpation towards the diagnosis of bladder dysfunction, urinary incontinence, and early-stage bladder cancer.

The proposed micro-robot consists of two subsystems; a unique  $4mm$  outer diameter tendon-driven continuum segment from assembled “vertebrae” components with male and female snap-in features for joint assembly, an elastic tube encompassing each joint for controlled compliance and structural integrity that enters the bladder through the urethral, and an external segment with prismatic and hyper-spherical joints to ensure higher dexterity and manipulability. The developed kinematic analyses avoid motion discontinuities and singularities for the desired poses anywhere in the confined space of the interior of the bladder wall.

The compliance of the tendon-driven proposed joint architecture was characterized as a function of the encompassing tube geometry and material properties using different modeling approaches (a strain energy model, a quasi-static model, and the principle of virtual work) and then applied to a multi-joint continuum segment.

Limited functionality continuum modules with different joint lengths and multiple joints were prototyped for tension-bend angle characterization using a computer vision outfitted experimental setup. A comparison of the results from the experimental analysis and theoretical models shows high fidelity in predicting the continuum robot behavior. In addition, multiple existing polymer-based additive manufacturing technologies were investigated for improving the fabrication quality of the continuum segment components while the pose error is evaluated using geometric manufacturing uncertainties.

This research demonstrates the proposed novel continuum segment module and its characterization for use in confined spaces in the human body for diagnostics purposes, employing the presented modeling approaches corroborated with experimental results.

## TABLE OF CONTENTS

ACKNOWLEDGEMENTS . . . . .	iv
ABSTRACT . . . . .	v
LIST OF ILLUSTRATIONS . . . . .	x
LIST OF TABLES . . . . .	xvi
Chapter	Page
1. INTRODUCTION . . . . .	1
1.1 Motivation . . . . .	2
1.2 State of the Art of Transurethral Manipulators . . . . .	3
1.3 Significance and Contributions of Research . . . . .	6
1.4 Dissertation Outline . . . . .	6
2. ROBOT DESIGN AND PROTOTYPING . . . . .	8
2.1 Operational Environment, Design Constraint, and Specifications of Proposed Robot . . . . .	8
2.2 Intended <i>in vivo</i> Operation of Proposed Robot . . . . .	10
2.3 Conceptual Design of Proposed Robot . . . . .	12
2.3.1 Original Conceptual Design . . . . .	12
2.3.2 Design Iterations and Improvement of Robot Continuum Segment . . . . .	15
2.3.3 Current Robot Conceptual Design . . . . .	19
2.4 Structural Analysis of the Continuum Segment . . . . .	23
2.4.1 Static Failure Analysis for Improved Mechanical Strength of the Robot Continuum Segment Joints . . . . .	23



2.5	Geometric Optimization of Robot Continuum Segment Module for Maximum Tension-Bend Angle Sensitivity . . . . .	43
2.5.1	Geometric Design Optimization Formulation . . . . .	44
2.5.2	Establishing Constraints . . . . .	46
2.6	Initial Prototyping of Robot Continuum Segment . . . . .	52
2.7	Continuum Segment Manufacturing: Investigation into Rapid Prototyping . . . . .	55
2.7.1	Experimental Methods and Methodology . . . . .	60
2.7.2	Evaluation of Geometric Responses due to Process Parameters . . . . .	66
2.7.3	Results and Discussion . . . . .	66
3.	MATHEMATICAL MODELING . . . . .	74
3.1	Forward Kinematics . . . . .	74
3.1.1	Robot Pose and Workspace Visualization . . . . .	75
3.1.2	Kinematic Pose Error due to Manufacturing Uncertainties . . . . .	77
3.2	Inverse Kinematics . . . . .	82
3.2.1	Mathematical Modeling Approach . . . . .	82
3.2.2	Performance of IK Formulation . . . . .	86
3.2.3	Singularity and Manipulability . . . . .	89
3.3	Quasi-Static Formulation of Continuum Segment . . . . .	93
3.3.1	Joint Compliance Modeling . . . . .	93
3.3.2	Joint Compliance Numerical Analysis . . . . .	97
3.4	Principle of Virtual Work: Multi-Module Continuum Segment Model . . . . .	101
3.4.1	Ideal Virtual Work Formulation . . . . .	102
3.4.2	Virtual Work Formulation Considering Frictional Cases . . . . .	104
3.4.3	Evaluation of Virtual Work Formulation . . . . .	107
3.4.4	Discussion on Virtual Work Model Analysis for Multi-Joint Continuum Segment Modules . . . . .	111

4. EXPERIMENTAL ANALYSIS: INITIAL TENDON-BEND ANGLE CHARACTERIZATION . . . . .	115
4.1 Experimental Setup . . . . .	115
4.1.1 Bend Angle Measurement using Computer Vision . . . . .	116
4.2 Single Continuum Module Equivalent Shear Modulus Estimation . . . . .	119
4.3 Experimental and Quasi-Static Model Tension-Bend Angle Results of a Single Continuum Module . . . . .	121
4.4 Multi-Module Continuum Segment Prototyping and Initial Characterization	125
4.4.1 Experimental Analysis with Multi-Joint Continuum Segment Modules Discussions . . . . .	128
5. CONCLUSIONS . . . . .	130
REFERENCES . . . . .	133
BIOGRAPHICAL STATEMENT . . . . .	147

## LIST OF ILLUSTRATIONS

Figure	Page
2.1 A. Male Urological Anatomy, B. Female Urological Anatomy, C. Interior Bladder Wall showing Internal Urethral Opening and Trigone Area [1] . . .	8
2.2 Illustrations of a Cystoscopy Performed by a Physician [2] A. Male Patient, B. Female Patient . . . . .	11
2.3 Proposed Micro Robotic System Components with the Robot Manipulator Components Highlighted in a Red Box. The Master Control Console serves as the User Interface with Visual Feedback of the Bladder [3, 4] . . . . .	12
2.4 Original Proposed Robot CAD Assembly (Masters Thesis) [5] . . . . .	14
2.5 Original Proposed Robot Flexible Continuum Segment Design (Masters Thesis) [5] . . . . .	14
2.6 Proposed Robot Model; $\theta_{R1}, \theta_P, \theta_Y, \theta_{R2}$ are revolute joint, $D_P$ is the prismatic joint, and $\theta$ is the whole continuum bend. . . . .	19
2.7 A. 3D Model of the Continuum Segment, ① Force Sensor Power and Signal Wires, ② Flexion and Extension Tendons, ③ Rigid Guide Tube, ④ Vertebra, ⑤ Snap-Fit Joint, ⑥ Force Sensor, ⑦ Joint Tubes, B. 3D Model of an Actuated Single Module with the Joint Tube . . . . .	20
2.8 3D Model of the Continuum Segment Vertebra . . . . .	21
2.9 Orientation Based Contact Force Schematic for a Single Module. A. Vertebrae at $0^\circ$ , B. Vertebrae at $90^\circ$ . . . . .	24
2.10 Design 2: Boundary Conditions for Vertebrae 1 and 2. . . . .	25
2.11 Design 2: Stress Analysis Results for Vertebrae 1 and 2. . . . .	26

2.12	Design 2: Deflection for Vertebrae 1 and 2 due to Vertical Loading. . . . .	26
2.13	Design 2: Stress Analysis for Vertebrae due to Lateral Loading. . . . .	27
2.14	Design 3: Boundary Conditions for Vertebrae 1 and 2 (Vertical and Side Loading). . . . .	28
2.15	Design 3: Stress Analysis for Vertebrae 1 and 2 (Vertical and Side Loading).	29
2.16	Design 3: Deflection for Vertebrae 1 and 2 (Vertical and Side Loading). . . .	29
2.17	Design 4: Boundary Conditions. A. Vertebra 1, B. Vertebra 2, C. Joint Pin for a $1N$ Reaction Load at $0^\circ$ Bend Angle. . . . .	32
2.18	Design 4: Stresses. A. Vertebra 1, B. Vertebra 2, C. Joint Pin for a $1N$ Reaction Load at $0^\circ$ Bend Angle. . . . .	33
2.19	Design 4: Deformation. A. Vertebra 1, B. Vertebra 2 for a $1N$ Reaction Load at $0^\circ$ Bend Angle. . . . .	33
2.20	Design 4: Boundary Conditions. A. Vertebra 1, B. Vertebra 2 for a $1N$ Reaction Load at $90^\circ$ Bend Angle. . . . .	35
2.21	Design 4: Stresses. A. Vertebra 1, B. Vertebra 2 for a $1N$ Reaction Load at $90^\circ$ Bend Angle. . . . .	35
2.22	Design 4: Deformation. A. Vertebra 1, B. Vertebra 2 for a $1N$ Reaction Load at $90^\circ$ Bend Angle. . . . .	36
2.23	Design 5 at $0^\circ$ Bend Angle. A. Vertebra Boundary Conditions, B. Vertebra Stresses for a $1N$ Reaction Load at $0^\circ$ Bend Angle, C. Vertebra Deformation.	37
2.24	Design 5 at $90^\circ$ Bend Angle. Vertebra Boundary Conditions, B. Vertebra Stresses for a $1N$ Reaction Load at $90^\circ$ Bend Angle, C. Vertebra Deformation.	37
2.25	Design 6: Boundary Conditions. A. Vertebra 1, B. Vertebra 2 for a $1N$ Reaction Load at $0^\circ$ Bend Angle. . . . .	38
2.26	Design 6: Stresses. A. Vertebra 1, B. Vertebra 2 for a $1N$ Reaction Load at $0^\circ$ Bend Angle. . . . .	39

2.27 Design 6: Deformation. A. Vertebra 1, B. Vertebra 2 for a 1 <i>N</i> Reaction Load at 0° Bend Angle. . . . .	39
2.28 Design 6: Boundary Conditions. A. Vertebra 1, B. Vertebra 2 for a 1 <i>N</i> Reaction Load at 90° Bend Angle. . . . .	41
2.29 Design 6: Stresses. A. Vertebra 1, B. Vertebra 2 for a 1 <i>N</i> Reaction Load at 90° Bend Angle. . . . .	41
2.30 Design 6: Deformation. A. Vertebra 1, B. Vertebra 2 for a 1 <i>N</i> Reaction Load at 90° Bend Angle. . . . .	42
2.31 Design 7. A. Boundary Conditions, B. Stresses, C. Deformation for 1 <i>N</i> Reaction Load at 0° Bend Angle. . . . .	43
2.32 Design 7. A. Boundary Conditions, B. Stresses, C. Deformation for 1 <i>N</i> Reaction Load at 90° Bend Angle. . . . .	44
2.33 Schematic of Single Module Showing Geometric Design Variables. . . . .	47
2.34 Kinematics of 2–vertebrae for bending angle $\theta = 0^0$ . . . . .	48
2.35 Kinematics of 2–Vertebrae for Bending Angle, $\theta = 0^0 : 90^0$ using $d = 2.07l_1$ , $l_1 = l_2$ , and $r_{FC} = 990\mu m$ . . . . .	49
2.36 Design Variable Iteration History for $\mu = 0.22Nmm^{-2}$ . . . . .	52
2.37 Design Variable Iteration History for $\mu = 2Nmm^{-2}$ . . . . .	52
2.38 Vertebrae Fabrication Steps. A. CAD Vertebra Model, B. Print Settings in Photon™ Workshop, C. Vertebrae Oriented with Support and Sliced, D. Vertebrae on the Build Platform after Printing, E. Vertebrae Washed and Cured using the Washing and Cure Machine, F. Vertebrae Assembly for a 3 Joint Continuum Module. . . . .	54

2.39	Vertebra with 3mm Joint Length features. A. Tendon Channels, B. Male and Female Snap-in Features, C. Key Dimensions Indicated as (1, 2, 3, 4, 5, 6) are (2.1, 7.4, 1.4, 2.9, 2.3, 2.6)mm as Measured Respectively. Compared to (2.2, 7.7, 1.5, 3.0, 2.7, 2.7)mm as designed. . . . .	55
2.40	Schematic Showing Possible Manufacturing Defects and Dimensional Variations. A-I. As-Designed Tendon Channel, A-II. Impacted Tendon Channel, B-I. As-Designed Continuum Module Joint with vertebra prong, Male and Female Snap-in Features, B-II. Continuum Module Joint with Dimensional Variation in Male Snap-in Feature. . . . .	57
2.41	Solid Models of the 6mm Joint Length Vertebrae with Different Tendon Channel Diameters . . . . .	61
2.42	Multi-Model Vertebrae Setup in Chitubox™ . . . . .	62
2.43	Sample Manufactured Parts After Processing in Anycubic Wash Station . . . .	64
2.44	Sampled Imaged Vertebrae using ImageJ . . . . .	65
2.45	Effect of Factors on the Features of Interest . . . . .	72
2.46	Effect of Multiple Factors on the Various Geometries of Interest . . . . .	73
3.1	Robot Joint Representation and Frames According to the MDH Convention . .	74
3.2	Sample Robot Poses in the “Bladder Workspace”; Motion A: All Joint Parameters Initialized to Zero. Motion B: Continuum Segment Bending Angle of $\theta = 150^\circ$ . Motion C: Continuum Segment bend Angle, $\theta = 50^\circ$ , Pitch Angle, $\theta_P = 30^\circ$ , and Prismatic Joint $D_p = 30mm$ . . . . .	76
3.3	Vertebra Showing Geometry of Interest . . . . .	78
3.4	Robot Inverse Kinematics Evaluated Poses for Arbitrarily Selected Bladder Contact Locations. Note: Axes have same length for visualization purposes. .	87
3.5	Inverse Kinematics Iterative Solution Set for Selected Poses. . . . .	88

3.6	Singularity and Manipulability Measures for Motions Evaluated in Section 3.2.2 . . . . .	92
3.7	Flexible Tube Circular Cross Section. . . . .	95
3.8	A. Schematic for a Single Module with Flexible Tube over the Joint, B. Free Body Diagram of Vertebra 1, and C. Free Body Diagram of Vertebra 2. . . .	96
3.9	Single Module Tube Applied Tension as a Function of Bend Angle for Different Joint Lengths $L = (3, 6, 9, 12)mm$ with all other Parameters Assigned their Nominal Values. . . . .	99
3.10	Single Module Tube Applied Tension as a Function of Bend Angle for Different Shear Moduli $\mu = (0.45, 0.91, 1.82) Nmm^{-2}$ with all other Parameters Assigned their Nominal Values. . . . .	99
3.11	A. Schematic for n-Modules with Flexible Tube over the Joint, B. $i^{th}$ Vertebra Showing Friction, Force and Moment Interactions, and C. $n^{th}$ Vertebra Showing Force and Moment Interactions. . . . .	103
3.12	Schematic of the Tendon-Channel Friction Interaction for the $i^{th}$ Vertebra . .	105
3.13	Schematic Showing Joint Friction. A. Section view of a Single Continuum Module Showing Male and Female Snap-in Interference, B. Free Body Diagram of the Resulting Force and Moment. . . . .	107
3.14	Tension-Bend Angle Analysis for Cases 1-8 . . . . .	110
4.1	A. Experimental Setup to Characterize the Module Behavior without the Light-Controlled Environment. Single Module without Joint Tube for B. $3mm$ , C. $6mm$ , D. $9mm$ , E. $12mm$ Joint Lengths (scale in $mm$ ). . . . .	116
4.2	Computer Vision Flowchart for Bending Angle Measurement. . . . .	117
4.3	Schematic for the Analysis of Robot Curvature Geometric Parameters. . . .	118
4.4	Joint Tube Interaction with Vertebrae and Tendon during Bending; red and green solid lines represent the tendon path and interior tube wall. . . . .	120

4.5	Experimental and Quasi-Static Model Evaluated Tension-Bend Angle Responses for (3, 6, 9, 12)mm Joint Lengths. . . . .	122
4.6	Prototyped Continuum Segment Modules for 2 and 3 Joints with 3 and 6mm Joint Lengths . . . . .	126
4.7	Experimental Tension-Bend Angle Behavior for 2 and 3 Joint Modules with 3 and 6mm Joint Lengths . . . . .	128



## LIST OF TABLES

Table	Page
2.1 Robot Continuum Segment Design Iterations and Improvements. . . . .	16
2.2 Nominal Robot Model Dimensions (see Figs. 2.6, 2.7 and 2.8) . . . . .	22
2.3 Mechanical Properties for Formlabs Standard Grey Resin [6] . . . . .	25
2.4 Design 2: Maximum Stresses Associated with Varied Pin and Pin Hole Diameter . . . . .	30
2.5 Design 3: Maximum Stresses Associated with Varied Pin and Pin Hole Diameter . . . . .	31
2.6 Maximum Deflection due to Loading Conditions for Different Joint Designs	31
2.7 Single Module Geometric Parameters . . . . .	47
2.8 Design Variable Values for As-Designed and Optimized . . . . .	51
2.9 Table Showing the ANOVA Regression Model Summary . . . . .	69
3.1 Robot kinematic definition using the MDH notation . . . . .	75
3.2 Continuum Segment Pose Error Due to Manufacturing Geometrical Uncertainties . . . . .	80
3.3 Continuum Segment Pose Error Due to Uncertainties in Joint $\theta$ . . . . .	81
3.4 Summary of Results for Arbitrary Robot End Effector Pose on the Ellipsoid .	87
3.5 Two-Term Exponential Function Parameters for Tension-bend Angle Relationships based on theoretical analysis. . . . .	100
3.6 Tension Bend Angle Behavior for a Single Module with Varying Joint Friction	114
4.1 Tension-bend Angle Comparison from Experimental and Quasi-Static Model Analysis . . . . .	123

4.2	Experimental Tension-Bend Angle Results for Two Joint Modules with 3mm Joint Lengths . . . . .	126
4.3	Experimental Tension-Bend Angle Results for Two Joint Modules with 6mm Joint Lengths . . . . .	127
4.4	Experimental Tension-bend Angle Results for Three Joint Modules with 3mm Joint Lengths . . . . .	127
4.5	Experimental Tension-bend Angle Comparison for Three Joint Modules with 6mm Joint Lengths . . . . .	128

## CHAPTER 1

### INTRODUCTION

The use of robotics has seen significant application in medical intervention for prognosis, diagnosis, surgery, and rehabilitation, primarily because of their characteristics of precision, reliability, and their ability to access confined spaces in the human body [7]. Specific examples of such applications include endovascular, laparoscopic vascular, and cardiac surgery, or in robot-assisted rehabilitation of neurological motor impairments, etc [8, 9]. Recent medical applications have demanded a reassessment of the design architecture, behavior, performance, and reach of traditional medical robotic technologies due to the need for more confined space accessibility, improvement to patient care (by reducing scarring, loss of blood, and post-operation recovery rate) and the demand for improved functionality, performance and efficacy [10]. Traditional medical robotic technology comprises entirely of rigid components with dexterous distal wrists with high repeatability and precision. However, their design and configuration present challenges with miniaturization for improved accessibility to the human internal anatomy without incisions through natural orifices. On the other hand, the demands for the improvement of robot-assisted medical intervention have driven a paradigm shift from traditional robot designs towards designs with more flexible or soft components to improve human internal anatomy accessibility with greater end effector manipulability while reducing or eliminating the use of skin incisions to access the internal anatomy. Even so, these systems have their own challenges as a result of limitations with the design architecture and/or the sensing, modeling, and control approaches they employ [10, 11]. Flexible or soft robots are relatively difficult to control

and maneuver because of their uncanny high Degree-Of-Freedom (DOF) and approximate modeling techniques [10]. In like fashion, available flexible medical robotic technologies have design architectures that make use of materials such as shape memory alloy (like Nitinol) for actuation and Aluminum as the critical structural member for flexibility. However, studies have shown that these design approaches suffer from friction and backlash that affect motion accuracy [10, 12, 13].

## 1.1 Motivation

Urinary Incontinence (UI) is a medical condition where individuals suffer from a loss of bladder control, thereby leading to inadvertent leaking of urine from the urethra [14]. UI may be a symptom of mild or severe medical problems such as aged or weakened bladder muscles, physical damage to pelvic floor muscles, kidney stones, infection or prostate enlargement, benign tumors, and more importantly prostate or bladder cancer among other causes [15, 16]. In addition, according to the Urological Care Foundation, people who suffer from UI also experience negative effects on their emotional, psychological, and social life [16]. The prevalence of UI demonstrates the severity of the condition since approximately 400 million people worldwide are affected by it [17]. A 2014 review of the economic cost of UI by Milsom *et al.* showed the rates of UI among men and women as 1.5% to 14.3% and 1.6% to 22.8% respectively. They estimated an annual cost-of-illness of 7 billion euros in Europe and Canada combined and 66 billion US dollars in the USA [18].

Characterizing the stiffness properties of the bladder wall tissue is an important step towards obtaining critical information for a better understanding of diseases or dysfunction-inducing UI and/or for providing better patient care [19, 20]. However, current methods for quantitatively evaluating the elasticity of the bladder tissue such as cystometry or elas-

tography are not without variability [21]. These methods assume the entire bladder tissue structure as being homogeneous or rely heavily on the pressure or volume measurement of the bladder during the procedure [20, 22, 23]. In addition, these methods are non-contact and do not provide direct contact measurements for localized tissue characterization which is important to characterize the non-homogeneous trigone, midsection and bladder dome areas that constitute the bladder structure [20, 23].

## 1.2 State of the Art of Transurethral Manipulators

Advancements in robotics and its application to medical diagnosis, treatment, care, and rehabilitation could be an enabling technology advantageously employed to provide access to the bladder interior for possible solutions. Particularly, studies in *in vivo* medical interventions using Natural Orifice Transluminal Endoscopy Surgery (NOTES) and Single Point Access (SPA) systems serve as a springboard for robotics-based solutions since the mechanical architectures of these systems could be designed with the high dexterity needed to successfully transverse confined and complex *in vivo* structures while performing useful work [24, 25]. For instance, accessing the bladder (an ellipsoid-shaped membranous sac) through the urethra meatus requires overcoming the geometric constraints of the urethra [26, 27]. Hickling *et al.* stated that the bladder reshapes from a tetrahedron to an ellipsoid when emptied and filled respectively [26]. These differences in the geometry and structure of the bladder and urethra in possible patients certainly define the bladder-urethra constraint and support efforts toward uniquely developed robotic solutions. Current NOTES and SPA robotic systems are categorized by their actuation means and/or design approach as articulated, tendon-actuated, rigid-link, soft, or continuum robots [28]. However, these systems have their own challenges due to their design, sensing, modeling, and control approaches [11, 12, 13, 28, 5].

A significant amount of research has been performed on flexible robots for medical interventions focusing primarily on robot design, actuation, modeling, and control principles. The designs of these flexible robots comprise architectures with the use of pre-curved or pre-strained superelastic tubes as in concentric tube robots, or the use of multiple disks held along the central axis with a flexible member and actuation tendons as in tendon/cable continuum robots, or the use of shape memory alloy as critical displacement components as in shape memory robots, or the use of viscoelastic materials such as silicon as the entire structure as in soft pneumatic and hydraulic robots [5, 29, 30, 31, 32]. These design architectures have associated advantages and trade-offs; Concentric tube robots usually weigh less than other designs and can be extremely slender, while tendon/cable robots are easier to control compared to concentric tube robots, shape memory robots have high dexterity with the added ease of miniaturization, and soft robot manipulators are hyper compliant and biocompatible [10, 29, 32, 33, 34]. Tradeoffs associated with concentric tube robots are their limited bend variations, tendon/cable robots are affected by cable slack, shape memory robots have slow response speed with sensitivity to environment temperature, and soft pneumatic and hydraulic robots have high motion nonlinearities [29, 35]. Flexible robots generally suffer from limited workload capability, however, improvement attempts are currently investigated with consideration to dexterity and stiffness. For flexible manipulators, higher dexterity correlates adversely to poor stiffness or workload capability [36, 37, 38, 39].

In terms of actuation principles, flexible robots for medical applications have either intrinsic (having their actuation mechanism in the flexible structure) or extrinsic (having the actuation mechanism outside the flexible structure) actuation principles. Current extrinsic actuation means are tendon/cable driven, push-pull rods, or shape memory alloys where the lengths of these materials are shortened to create motion in the structures of a manipulator

[40, 41, 42, 43]. Meanwhile, intrinsic actuation principles involve the application of hydraulics, pneumatics, and magnetic fields (using fields created by magnets embedded in the robot structure). Both extrinsic and intrinsic actuation means could be combined to establish hybrid actuation systems [35]. The choice of actuation system is usually determined by the desired actuation and operational force required or the manipulator geometry and constraints related to the intended application, workspace, actuation speed, motion parameters, or compatibility with other medical and imaging equipment.

Modeling of flexible surgical robots includes kinematic, static, and dynamic analyses. In kinematic modeling, a piecewise constant curvature assumption is common where the bending section of the flexible robot is approximated as a circular arc [31, 41, 44]. Other research investigations have explored variable-curvature modal-based approaches to represent these robot segments or the use of traditional rigid link kinematics using Denavit-Hartenberg (D-H) parameters [31, 41, 45, 46]. Static modeling of these robots explored the use of classical elasticity theories such as Euler-Bernoulli beam theory, Cosserat rod theory, or energy methods. Dynamic modeling of flexible surgical robots is challenging with relatively less exploration [31, 47, 48, 49, 50].

Despite advancements in robotic interventions for NOTES and SPA, transurethral robotic solutions have been insufficient and suffer from limited tooltip dexterity and fettered accessibility to the entirety of the bladder [51]. Other key technical issues, such as position and motion accuracy impeding the deployment of NOTES and SPA robotic systems for transurethral intervention can be attributed to the design approaches and mechanical architectures employed [28, 52, 53]. Therefore, further investigation to mitigate these limitations with novel or improved design approaches and mechanical architectures or concepts is needed [28, 52, 53].

### 1.3 Significance and Contributions of Research

The uniqueness of this research stems from addressing a critical medical need by providing a unique diagnosis tool for operation in a hyper-constrained and difficult to access environment. The significance of this research contributes to the field of medical robotics by proposing

1. A robotic device to deliver and position, orient a diagnostic force sensor in the bladder for direct localized characterization of the biomechanical properties of tissues *in vivo* that could significantly improve the quality of medical care and interventions.
2. A methodology for the analysis and design of a unique hybrid flexible-rigid hyper-redundant micro-continuum manipulator architecture while avoiding singularities in the hyper-constrained environment of the urological anatomy.
3. A methodology for the fabrication and prototyping of the continuum part of the manipulator.
4. A methodology to characterize the nonlinear behavior of the proposed continuum segment manipulator and similar types, and a procedure to quantitatively measure the joint motion of the manipulator, thus providing an approach for optimizing the performance of the proposed manipulator.

### 1.4 Dissertation Outline

Chapter 1 begins this dissertation with the design requirements of the proposed manipulator and a description of the manipulator intended operational use.

Chapter 2 presents the conceptual designs and design iterations of the robot along with the manufacturing method used for fabricating a subpart of the robot. The structural analysis



of the continuum segment components is examined to meet the design requirements for a chosen material and presented.

Chapter 3 presents modeling for motion studies using forward and inverse kinematics of the entire robot. The force and moment interactions at the continuum segment for tension-bend angle characterizations are developed and presented.

In Chapter 4, the initial tendon-bend angle characterization using additive manufacturing to prototype limited functionality components and a computer vision-enabled experimental testbed is introduced.

Chapter 5 offers conclusions about the overall work and suggests future activities.

## CHAPTER 2

### ROBOT DESIGN AND PROTOTYPING

#### 2.1 Operational Environment, Design Constraint, and Specifications of Proposed Robot

As mentioned in section 1.2, the urinary tract, bladder structure, and environmental conditions present a unique workspace for any robot operation. The workspace is hyper-constrained with unique bladder and urethra geometries and structures for males and females as shown in Fig. 2.1 [27].

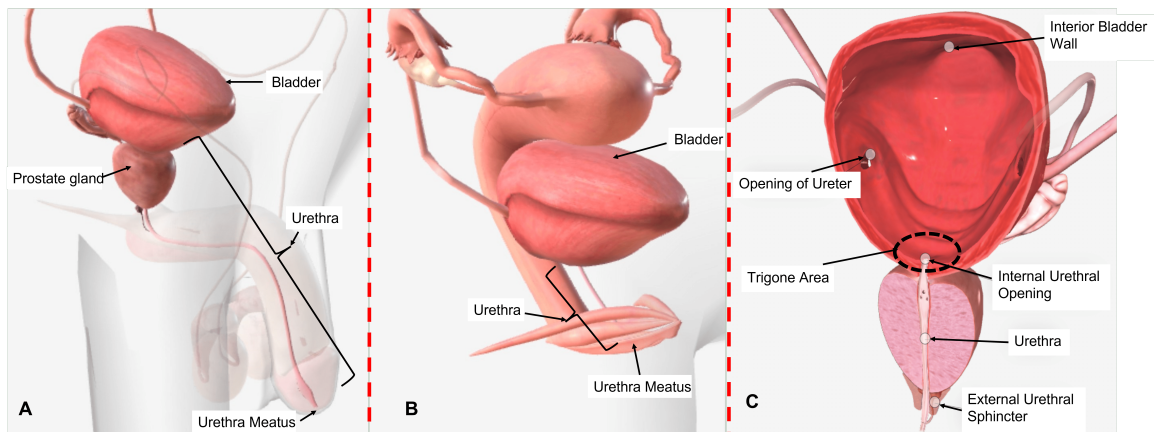


Figure 2.1: A. Male Urological Anatomy, B. Female Urological Anatomy, C. Interior Bladder Wall showing Internal Urethral Opening and Trigone Area [1]

The internal bladder environment is wet and could also pose a slippage challenge during palpation of the bladder walls. Likewise, the volume of the bladder varies across patients [26]. In this research, without loss of generality of the proposed manipulator, the geometry of the bladder considered for analysis and design is that of an ellipsoid with dimensions

of (length, width, height)= (93, 96, 82)*mm* [54]. However, if a different size or volume bladder is considered, the presented methodology and robot can be easily modified and employed to complete the same purpose.

Likewise, complications due to the size of transurethral instruments have been studied in attempts to establish a sizing standard for such instruments. In a study with 115 patients, Hudson *et. al.* investigated the relationship between ureteroscope insertion, its diameter, and the required rate of ureteric dilation [55]. The study concluded that when the ureteroscope diameter reduced from (9.0 to 7.4)*Fr*, (3.00 to 2.47)*mm*, the percentage of failure to insert the ureteroscope decreased from 37% to 0.9%. De Coninck *et. al.* surveyed 148 patients to assess urethral wall injuries associated with the size of ureteroscopy instruments [56]. They found that when (14.0 to 16.0)*Fr*, (4.67 to 5.33)*mm*, instruments were used, superficial lesions were present on the urethra wall in 39.9%, deeper urethra wall lesions in 17.6%, and circumferential perforation in 4.7% of the patients. Lildal *et. al.*, in a study with 180 patients, found that lesions and other complications associated with post-ureteroscopic surgery decreased when reduced diameter ureteroscopy instruments were used, particularly for (12 to 10)*Fr*, (4.00 to 3.33)*mm* [57]. These works clearly demonstrate that reduced diameter transurethral diagnostic instruments are associated with reduced patient trauma.

Therefore, the proposed manipulator must be designed with a constrained diameter of  $\leq 4\text{mm}$  for reduced patient trauma during transurethral palpation while still meeting operational and other design requirements. Along with the constrained diameter of the proposed manipulator, the urethrae lengths of 13 to 20*cm* in males and 3.8 to 5.1*cm* in females are important geometric factors that should be considered.

Furthermore, the proposed robot must be able to access the bladder through the urethra meatus and the urethra to meet the operational requirement of positioning and orienting the

force sensor normal to the bladder wall at the point of interest during tissue palpation and interrogation. The robot must meet these requirements considering size constraints for the motion actuation mechanism while exhibiting acceptable positioning and orientation error for the distal end attached force sensor.

## 2.2 Intended *in vivo* Operation of Proposed Robot

A transurethral intervention with the proposed robot is intended to follow similar steps to those of a cystoscopy procedure as outlined by Engelsjerd *et al.* [58] where the patient takes a lithotomy position as shown in Fig. 2.2. First, a lubricated rigid sheath tube longer than the length of the urethra and with slightly larger diameter than the continuum segment of the robot is inserted into the urethra to facilitate a pathway for the manipulator during operation of the robot prismatic joint. The rigid sheath tube also prevents the manipulator from interacting directly and being in contact with the urethra walls during operation (motion/positioning/orientation) in an effort to reduce patient trauma. Leading with the end effector, the continuum segment is inserted into the rigid sheath tube protecting the urethra meatus and extended through the patient's urethra and into the bladder. With the help of medical ultrasonography, the robot operator will locate the point of interest on the bladder wall and the control system will guide the robot such that the sensor orients itself for normal palpation at one or multiple points of interest in a single insertion operation. At the end of the operation, the manipulator will be retracted from the urethra and the urethra meatus, and then the sheath tube will be removed.

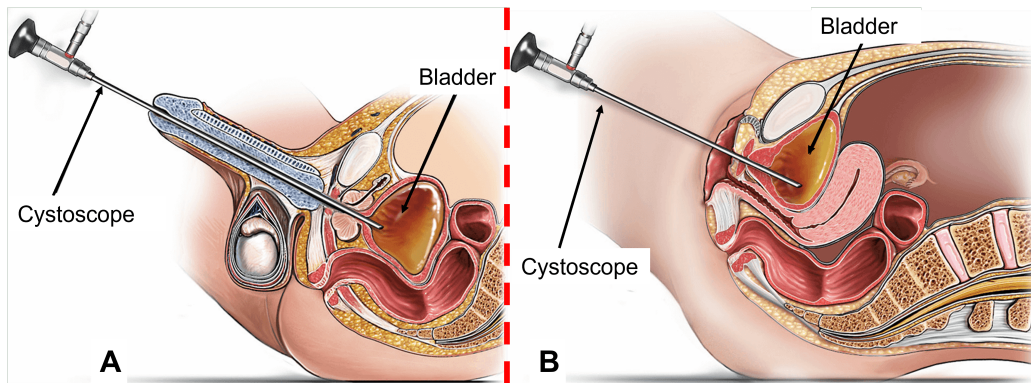


Figure 2.2: Illustrations of a Cystoscopy Performed by a Physician [2] A. Male Patient, B. Female Patient

Therefore, considering the relevant geometric design constraints enforced by the urethra-bladder anatomy and the intended *in vivo* operation, the proposed diagnostic robotic system was conceptualized to comprise of the following components (see Fig. 2.3):

1. A computer vision system with the ability to map and acquire regions of interest on the bladder interior wall.
2. A force sensor for recording the reaction forces from the bladder wall during palpation.
3. **A manipulator with a hybrid flexible-rigid design architecture that could host a force sensor at the distal end with reachability and orientation capabilities to all areas of the bladder wall while meeting the urethra-bladder geometric constraints.**
4. **An actuation mechanism concept and motion formulation that allows complete manipulability of the entire proposed robot to achieve the desired pose (position and constrained orientation) without singularity or motion discontinuity.**

The components of the robotic system highlighted in bold (3 and 4) represent the focus of my Ph.D. dissertation.

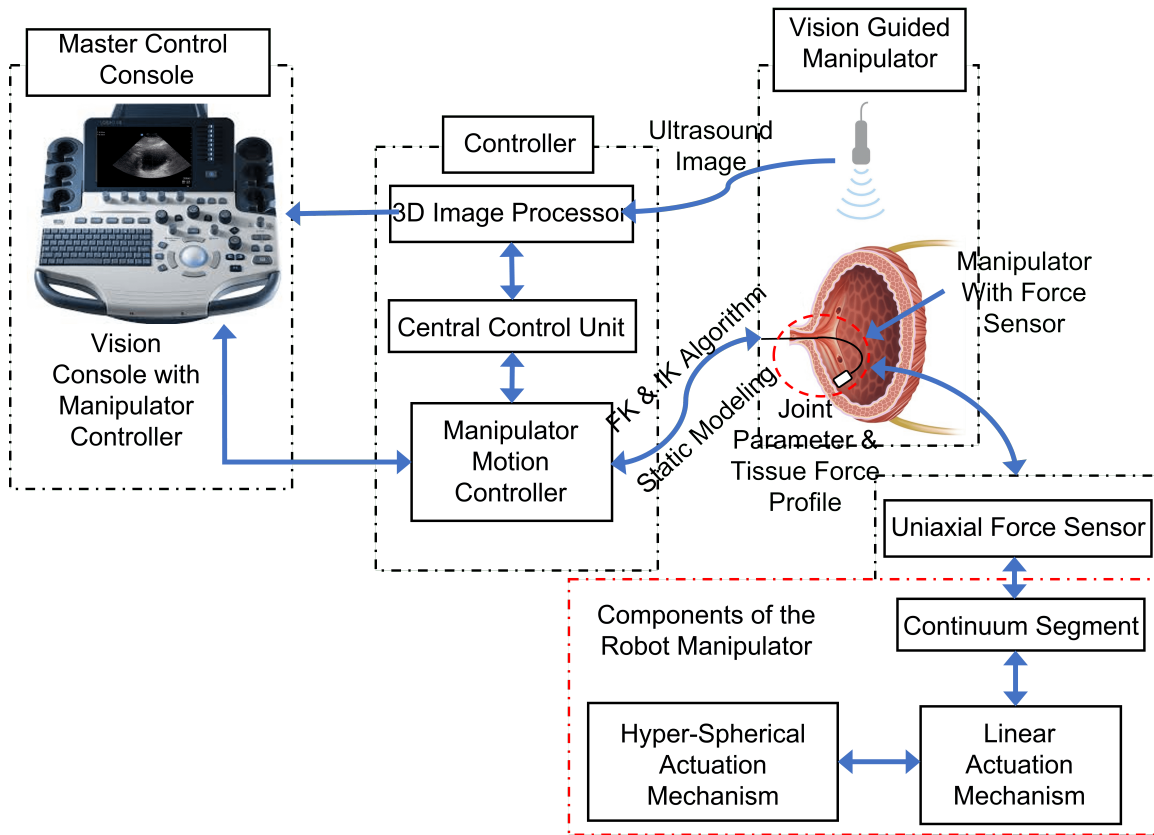


Figure 2.3: Proposed Micro Robotic System Components with the Robot Manipulator Components Highlighted in a Red Box. The Master Control Console serves as the User Interface with Visual Feedback of the Bladder [3, 4]

## 2.3 Conceptual Design of Proposed Robot

### 2.3.1 Original Conceptual Design

The original conceptual design of the proposed robot was developed during my Masters thesis research [5]. The major structural components of the proposed robot manipulator (as presented in Figs. 2.4 and 2.5) are the flexible-continuum segment that is comprised of

multiple vertebrae attached to each other with pins forming at a pin joint. The assembled vertebrae are then inserted in a silicone tube. A force sensor is attached to the vertebrae base at the distal end of the other assembled vertebrae. While the base vertebra joint is attached to an extended rigid tube. Two tendons extend from the base of the force sensor, on either side of the central axis of the continuum module, and are guided via through-channels in the vertebrae to the base of the rigid tube to a tendon actuation mechanism. The tendon actuation mechanism is composed of two V-groove guide pulleys that allow the routing of the tendon to two actuators for uniform flexion and extension of the flexible-continuum module. The flexible-continuum module with the tendon actuation mechanism is envisioned to be mounted on a linear actuation mechanism and altogether mounted on a hyper-spherical joint base composed of four actuators with a mounting base. The flexible-continuum module is envisioned to have a bending angle between  $-90^\circ$  and  $+90^\circ$  due to the actuation of the flexion and extension tendons. While the linear and hyper-spherical actuation allows the flexible-continuum module along with the tendon actuation mechanism to translate  $60mm$  and the robot to acquire a desired pose. The hyper-spherical mechanism is mounted to a fixed base.

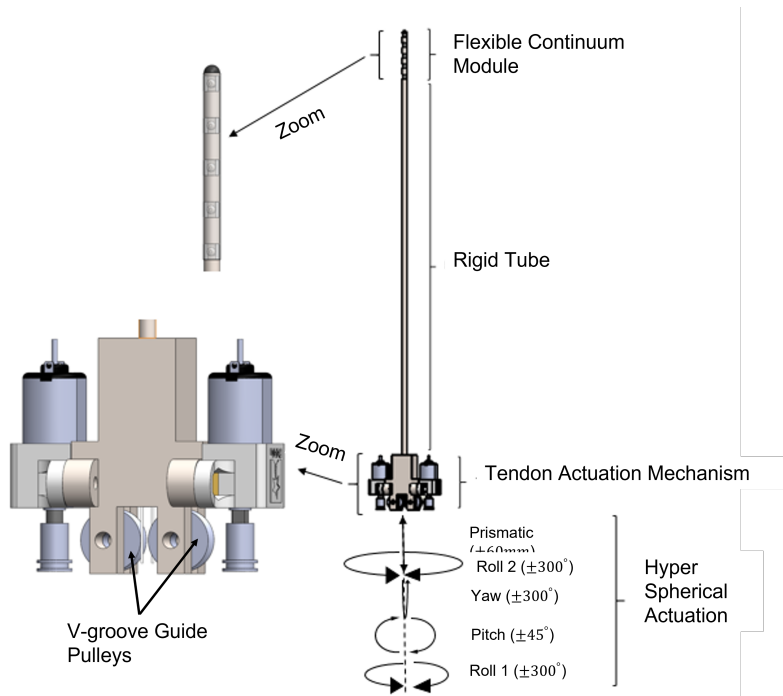


Figure 2.4: Original Proposed Robot CAD Assembly (Masters Thesis) [5]

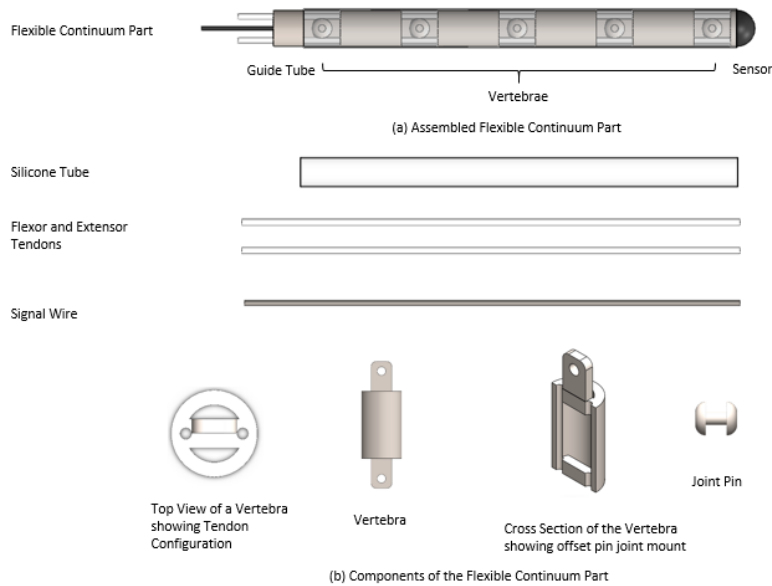


Figure 2.5: Original Proposed Robot Flexible Continuum Segment Design (Masters Thesis) [5]

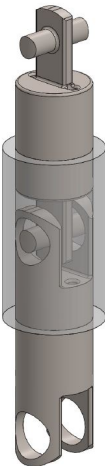
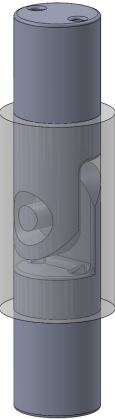


The original proposed robot design may have met the design requirements. However, the original proposed robot is largely conceptual (particularly for the linear and the hyper-spherical actuation mechanism). Additive manufacturing (also known as 3D-printing) was used to fabricate the continuum segment to scale and at  $3\times$  scale. The  $3\times$  scale was assembled while the at-scale continuum segment components proved challenging to prototype. As such, improved design and manufacturing methods were investigated.

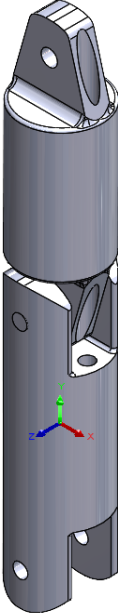
### 2.3.2 Design Iterations and Improvement of Robot Continuum Segment

Design improvements to the proposed manipulator first focused on the robot continuum segment due to the high probability of failure and difficulty to fabricate the micro vertebra-joint pin components. The design iterations shown in Table 2.1 were informed by the ease of fabrication (especially with rapid prototyping methods such as additive manufacturing) and structural analysis. Also, the use of an elastic tube encompassing the entire length of the continuum segment is redundant as its usefulness is to enable a compliant joint behavior and as such is only required to encompass each joint. Therefore, multiple independent elastic tubes are only used to encompass each joint. An advantage of this modification makes it possible to define the compliance of each joint by pre-selecting elastic tubes with different required material and geometric properties for unique joint configurations of the continuum segment of the manipulator. The design iterations enumerated in Table 2.1 and associated studies suggest that Design 7 allows significantly higher load-bearing capacity, ease of assembly, and limits lateral motion.

Table 2.1: Robot Continuum Segment Design Iterations and Improvements.

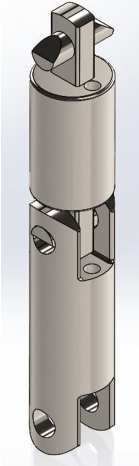

CAD Designs	Revisions	Advantages & Disadvantages
	<ul style="list-style-type: none"> <li>- Monolithic design and fabricated as a whole</li> <li>- Monolithic fabrication without tube</li> </ul>	<ul style="list-style-type: none"> <li>- Ease of fabrication using additive manufacturing</li> <li>- Pin and pin hole clearance limited to the 3D printing technology used</li> <li>- Joint load bearing capacity insufficient and prone to lateral motion using polymeric materials</li> </ul>
Design 2		<ul style="list-style-type: none"> <li>- Ease of fabrication using additive manufacturing similar to Design 2</li> </ul>
	<ul style="list-style-type: none"> <li>- Monolithic design and fabricated as a whole</li> <li>- Monolithic fabrication without tube</li> </ul>	<ul style="list-style-type: none"> <li>- Pin and pin hole clearance limited to the 3D printing technology used</li> <li>- Better load bearing capacity than Design 2 but still insufficient and prone to lateral motion</li> </ul>
Design 3		Continued on next page

**Table 2.1 – continued from previous page**

CAD Designs	Revisions	Advantages & Disadvantages
	<ul style="list-style-type: none"> <li>– Non-monolithic design with the use of joint pin</li> </ul>	<ul style="list-style-type: none"> <li>– Better load-bearing capacity than Designs 2 and 3 but still insufficient and prone to lateral motion</li> <li>– The use of a joint pin may increase the complexity of fabrication and the risk of structural failure</li> </ul>
<p>Design 4 (without joint tube)</p>	<ul style="list-style-type: none"> <li>– Non-monolithic joint design to eliminate lateral motion with the use of a captive joint pin</li> </ul>	<ul style="list-style-type: none"> <li>– No lateral motion</li> <li>– Insufficient load-bearing capacity, lower than designs 2, 3 and 4</li> <li>– Existing complexity and risk due to joint captive pin</li> </ul>
<p>Design 5 (without joint tube)</p>		

Continued on next page

**Table 2.1 – continued from previous page**

CAD Designs	Revisions	Advantages & Disadvantages
	<ul style="list-style-type: none"> <li>– Snap-in joint to eliminate the use of joint pin</li> </ul>	<ul style="list-style-type: none"> <li>– Easy of assembly</li> <li>– Significantly lower load bearing capacity</li> </ul>
<p>Design 6 (without joint tube)</p>		
	<ul style="list-style-type: none"> <li>– Improved Snap-in joint design</li> <li>– Side stops designed into vertebra prongs</li> </ul>	<ul style="list-style-type: none"> <li>– Significantly higher load-bearing capacity</li> <li>– Ease of assembly</li> <li>– No lateral motion</li> </ul>
<p>Design 7 (without joint tube)</p>		

### 2.3.3 Current Robot Conceptual Design

The proposed robot model is presented in Fig. 2.6 with the continuum segment having an overall diameter of  $4mm$ . The *ex-situ* actuated robot consists of 10 joints. The robot consists of 4 direct driven revolute joints for the hyper-spherical motion ( $\theta_{R1}, \theta_P, \theta_Y, \theta_{R2}$ ), 1 direct driven prismatic joint ( $D_P$ ), and 1 equivalent revolute joint for the distal 5-articulated joints with total motion ( $\theta$ ) for the continuum body controlled by flexion/extension tendons. The architecture of the hyper-spherical configuration reduces the probability of singularities by providing alternative solutions for a desired pose [59, 60]. Avoiding singularity is important in this research since it enables achieving normal orientation anywhere on the bladder wall for palpation purposes without encountering singularities or motion discontinuities while attaining the desired pose. The prismatic joint enables linear translation of the robot continuum segment to extend or retract the end effector to reach all areas in the bladder through the urethra considering the different urethra lengths for males and females.

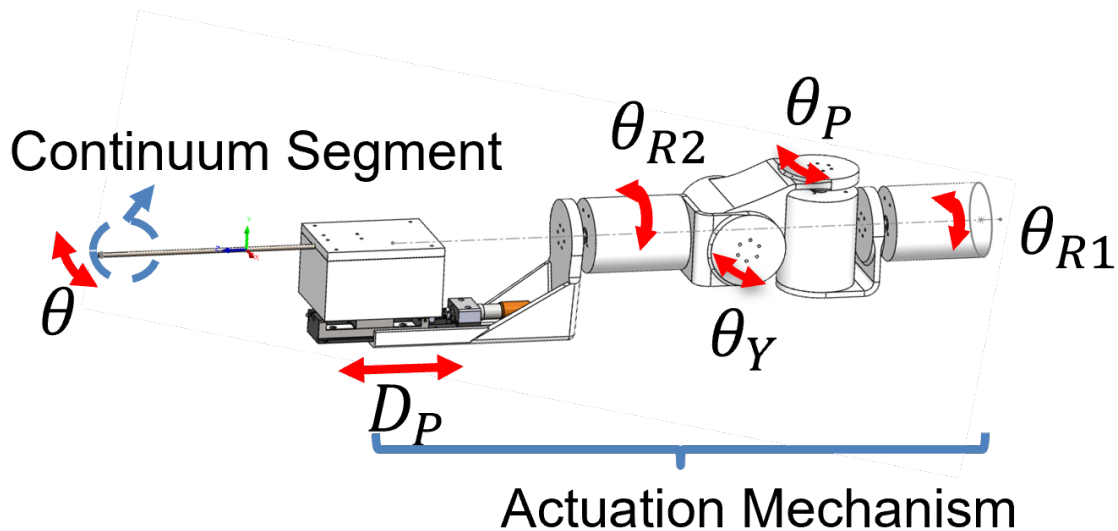


Figure 2.6: Proposed Robot Model;  $\theta_{R1}, \theta_P, \theta_Y, \theta_{R2}$  are revolute joint,  $D_P$  is the prismatic joint, and  $\theta$  is the whole continuum bend.

### Continuum Segment Description

The distal 5 articulated joints are referred to as the “continuum segment” due to compliance and the multiple elastic components that allow for a continuous curvature motion [61, 62]. The continuum segment architecture is that of a planar multi-elbow joint-like structure with sequentially connected vertebrae presented in Fig. 2.7.

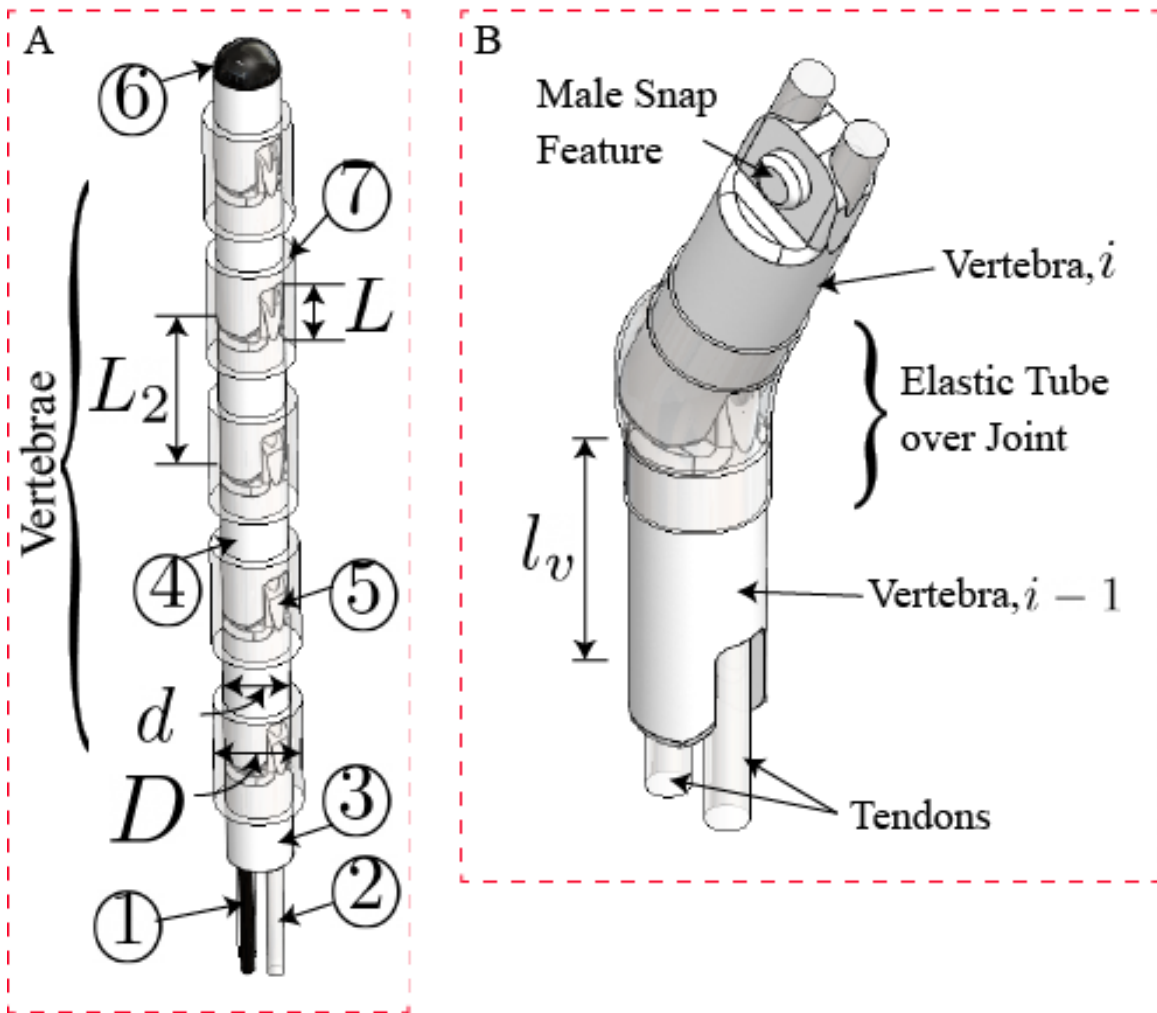


Figure 2.7: A. 3D Model of the Continuum Segment, ① Force Sensor Power and Signal Wires, ② Flexion and Extension Tendons, ③ Rigid Guide Tube, ④ Vertebra, ⑤ Snap-Fit Joint, ⑥ Force Sensor, ⑦ Joint Tubes, B. 3D Model of an Actuated Single Module with the Joint Tube

Each vertebra (shown in Fig. 2.8) is designed as a cylindrical structure with a male and a female snap feature at each end. Two vertebrae form a rotational joint when the male snap of one vertebra is fitted into the female snap of the next vertebra. The two vertebrae are then inserted in an elastic tube and each end of the elastic tube is securely fastened to each vertebra. Using biocompatible adhesive such as Masterbond® EP3HTMed or Loctite®, the two vertebrae and an elastic tube is assembled and will be referred to as a single continuum segment module or simply a module.

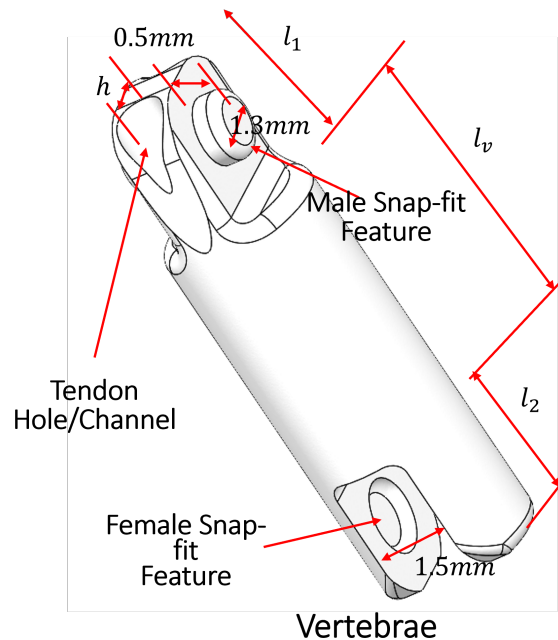


Figure 2.8: 3D Model of the Continuum Segment Vertebra

The flexion and extension of the continuum segment are achieved by tendons that run through all the modules of the continuum segment to the distal vertebra and controlled by two *ex-situ* actuators fixed to the base of the rigid tube and ride on the prismatic joint (see Fig. 2.6). One of the functions of the elastic tube is to keep the snap-in connection and the two vertebrae together. Since the elastic tube covers the snap-in rotational joint, the

rotation of each single module joint depends on the reaction stresses generated by the tube when the tendons are actuated. These reaction stresses control the bending behavior of the joint and are a function of the material and geometric properties of the elastic tube and the geometric parameters of the module joint. These reaction stresses could be advantageously employed to control individual joint rotation since the applied tension or actuating force must overcome these stresses.

### Robot Components and Dimensions

Computer-aided design (CAD) models of the  $4mm$  continuum segment and actuation system are shown in Figs. 2.6, 2.7 and 2.8. The continuum segment configuration consists of five modules of four vertebrae numbered from the base to the distal end, the rigid tube, and a force sensor as the end effector.

Table 2.2: Nominal Robot Model Dimensions (see Figs. 2.6, 2.7 and 2.8)

$L = 3.00mm$	Joint length
$L_2 = 8.00mm$	Joint to joint length
$l_v = 5.00mm$	Vertebrae length
$d = 3.00mm$	Vertebrae diameter
$D = 4.00mm$	Elastic tube outside diameter

The nomenclature and nominal dimensions of the different components of the robot CAD model in Figs. 2.7 and 2.8 are presented in Table 2.2. Figure 2.7① are power and signal wires for the force sensor and Fig. 2.7② are the flexion and extension tendons controlled by actuators at the external actuation unit. The tendons are routed via through-channels in each vertebra to the base of the sensor. Figure 2.7③ is the rigid tube that provides a structural interface from the continuum segment to the actuation unit for ease of inserting and removing the robot through the urethra to reach the bladder. Figure 2.7④ is the vertebra and two consecutive vertebrae are connected (see Fig. 2.7⑤) to form a rotational joint.



Figure 2.7⑥ is a force sensor attached at the distal end of the robot continuum segment to interrogate and interact with the interior bladder wall tissue while adhering to the same geometric constraints as the continuum segment [63]. An elastic tube (see Fig. 2.7⑦) encompasses each vertebra joint and is assumed to maintain a constant curvature during bending.

## 2.4 Structural Analysis of the Continuum Segment

Static failure analysis of the vertebrae for each design is evaluated under static reaction loading of  $1N$  to determine if the continuum module will sustain the applied load during palpation of the bladder tissue and to inform improvements to the design. This analysis is important to ensure the continuum module will not fail or become permanently distorted at the joints, thus ruining its joint geometry and reduce the reliability and performance while in *in vivo* use.

### 2.4.1 Static Failure Analysis for Improved Mechanical Strength of the Robot Continuum Segment Joints

Failure analysis was performed focusing on the joints of the robot continuum segment as it is hypothesized that the joints would experience high stresses as a result of the reaction forces due to tissue palpation. Investigating the high stresses on the micro-joints was also important to reduce the diameter of the size of the different components of the continuum segment, and improve the fabrication procedures, performance, operation, and design of the robot while ensuring patient safety during operation. The failure analysis was performed on the vertebrae assuming they were in a single continuum module (two vertebrae connected to form a rotary joint) configuration using a force propagation method. Assuming a contact force at the distal vertebra, the region of the joint highlighted in red in Fig. 2.9 will experience a significant magnitude of the reaction force. The static analysis in ANSYS® is

set up with a boundary condition, an applied force, and a fixed support to simulate the joint interactions in the schematic shown in Fig. 2.9.

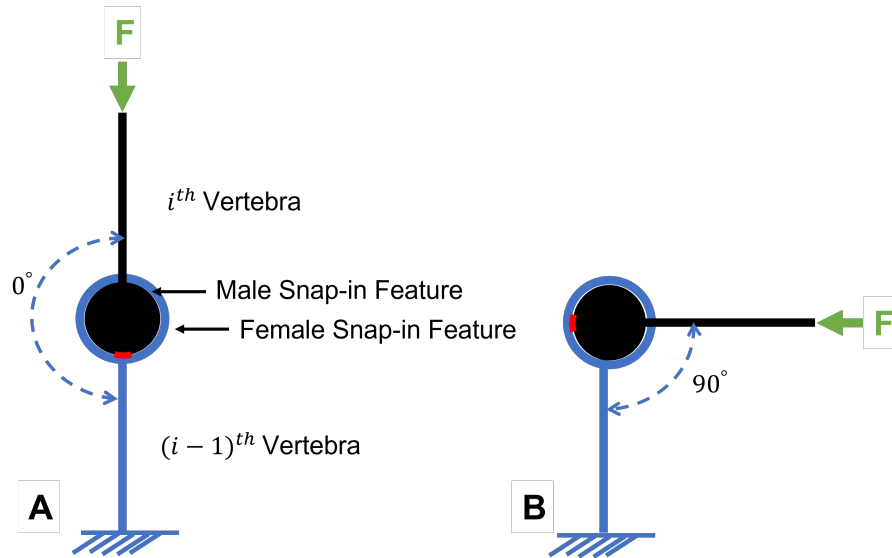


Figure 2.9: Orientation Based Contact Force Schematic for a Single Module. A. Vertebrae at  $0^\circ$ , B. Vertebrae at  $90^\circ$ .

## Design 2

First, the initial joint geometry is improved (by varying the pin and pin hole diameter) in a way that maximizes the structural integrity of the design while meeting the design criteria of  $1N$  maximum tissue contact force,  $3mm$  overall vertebrae diameter and the design requirements of resin-based 3D printing fabrication technology (tolerance, clearance, resolution, etc.). Figures 2.10 and 2.11 show the boundary conditions and stress analysis for Vertebrae 1 and 2 respectively. The deflection experienced by the individual vertebrae for the single robot module is shown in Fig. 2.12. Vertebra 1 was set up in such a way that the bottom pin hole has a fixed support and the side of the top pin hole has an applied force of  $1N$ . Vertebra 2 has the bottom pin (surface area in contact with the top pin hole) with a fixed support and an applied force of  $1N$  on the top face of the vertebra. A Formlabs

3D printer was considered to fabricate the vertebrae using the standard grey resin with its material properties given in Table 2.3 and used for the finite element analysis [6].

Table 2.3: Mechanical Properties for Formlabs Standard Grey Resin [6]

Mechanical Properties	Green	Post-Cured
Tensile Strength at Yield ( $MPa$ )	38	65
Young's Modulus ( $GPa$ )	1.6	28
Elongation at Failure	12 %	6.2
Flexural Modulus ( $GPa$ )	1.25	2.2

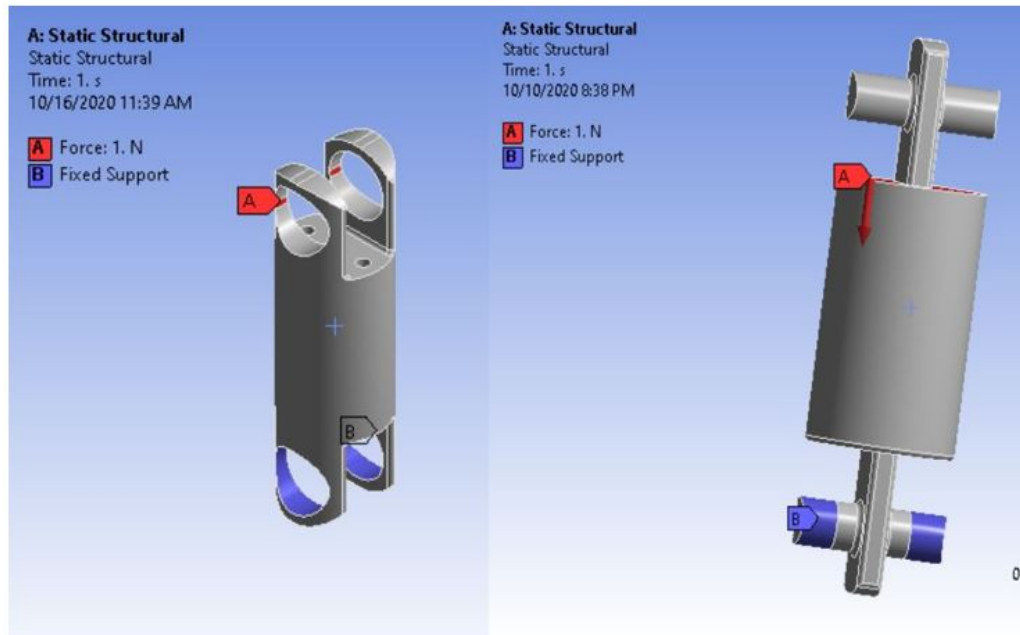


Figure 2.10: Design 2: Boundary Conditions for Vertebrae 1 and 2.

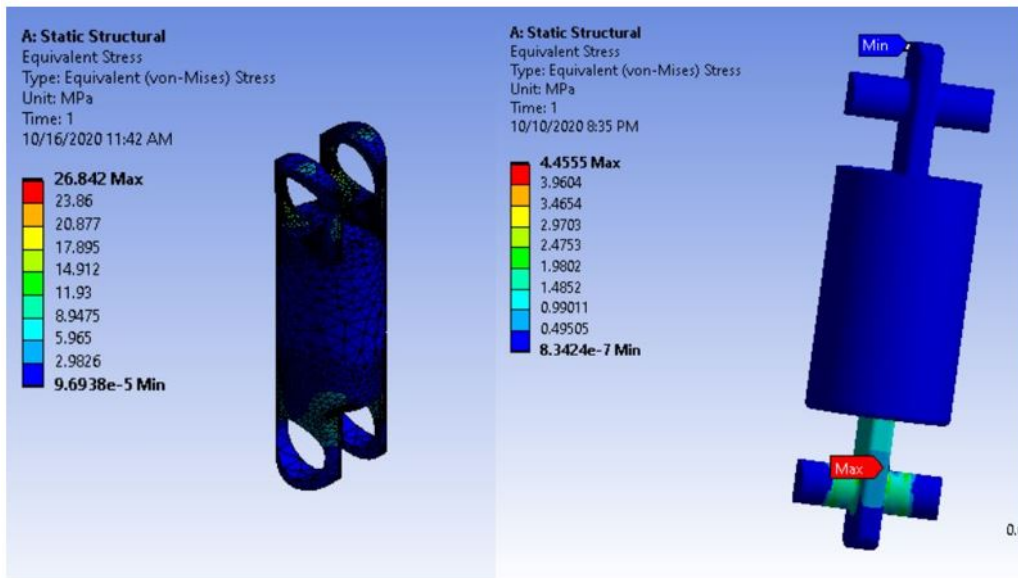


Figure 2.11: Design 2: Stress Analysis Results for Vertebrae 1 and 2.

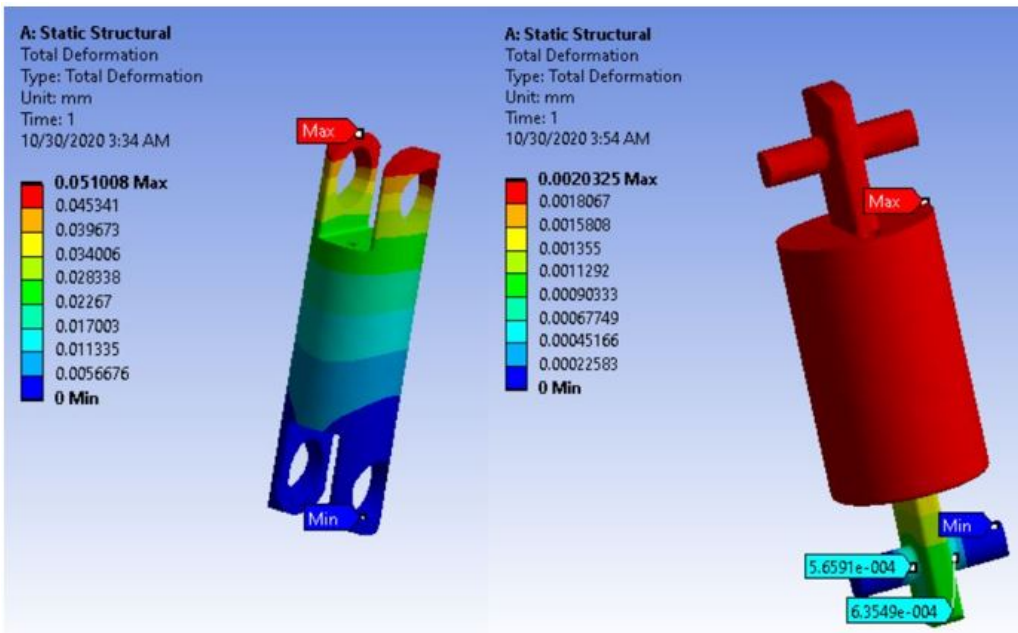


Figure 2.12: Design 2: Deflection for Vertebrae 1 and 2 due to Vertical Loading.

In anticipation of some lateral loading as a result of workspace disturbance (and in a situation where the prongs of Vertebra 1 act as stops to prevent lateral motion of Vertebra 2), the stress analysis due to lateral loading on the free-moving vertebra at the joint was also performed and evaluated for a  $0.35N$  loading. A lateral loading of  $0.35N$  is chosen as a fraction of the palpating force; while minimal or no side disturbance from the urethra wall is expected. Figure 2.13 shows the boundary conditions and stress results for Vertebra 1. The boundary conditions are applied such that the force acts in 1-D on the red region while fixed support is applied on the blue region.

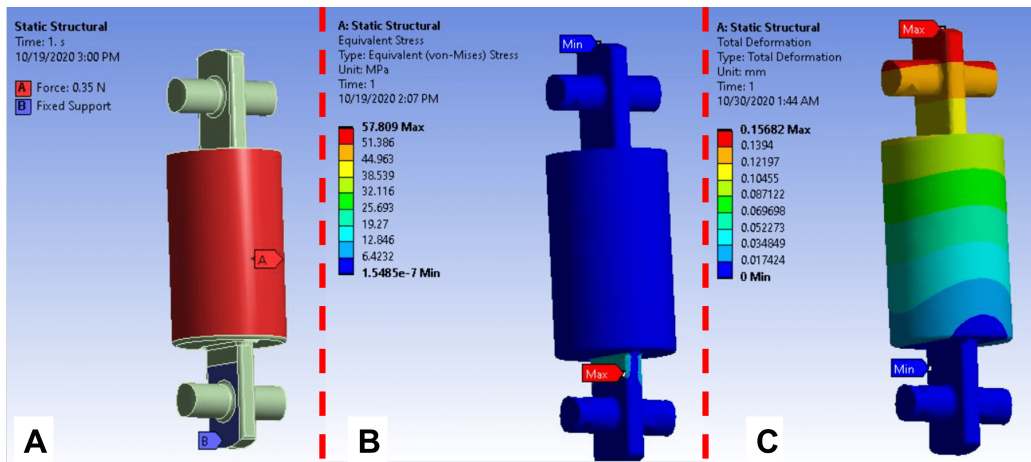


Figure 2.13: Design 2: Stress Analysis for Vertebrae due to Lateral Loading.

The results from the failure analysis setup (Figs. 2.11 and 2.13) show that the maximum stresses estimated are below the ultimate tensile strength of  $65MPa$  yielding a Factor of Safety,  $FoS \geq 2.42$ .

### Design 3

The failure analysis for Design 3 used boundary conditions and applied force setup similar to Design 2. The initial joint geometry was refined (by varying the pin, pin hole diameter,

and the length and width of the structural frame of the pin and pin hole) to maximize the structural integrity of the design while meeting the design criteria and requirements as in Design 1. Figures 2.14 and 2.15 show the boundary conditions and stress analysis for both Vertebrae 1 and 2. The deflection experienced by the individual vertebrae of the single robot module is shown in Fig. 2.16. Vertebra 1 was set up in such a way that the base was fixed at B with an applied force of 1N on the pin region shaded red, while Vertebra 2 has the flat face fixed while a force of 1N is applied on the region of the vertebra shaded red. The material properties defined were the same as that for Design 2.

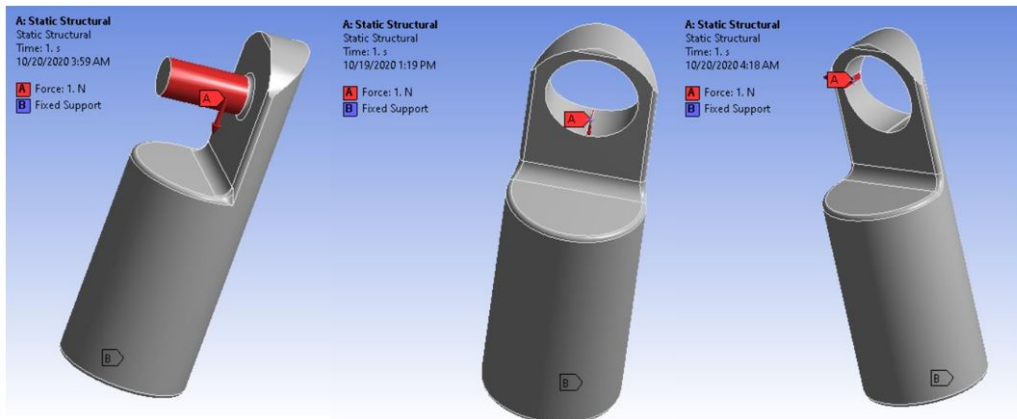


Figure 2.14: Design 3: Boundary Conditions for Vertebrae 1 and 2 (Vertical and Side Loading).

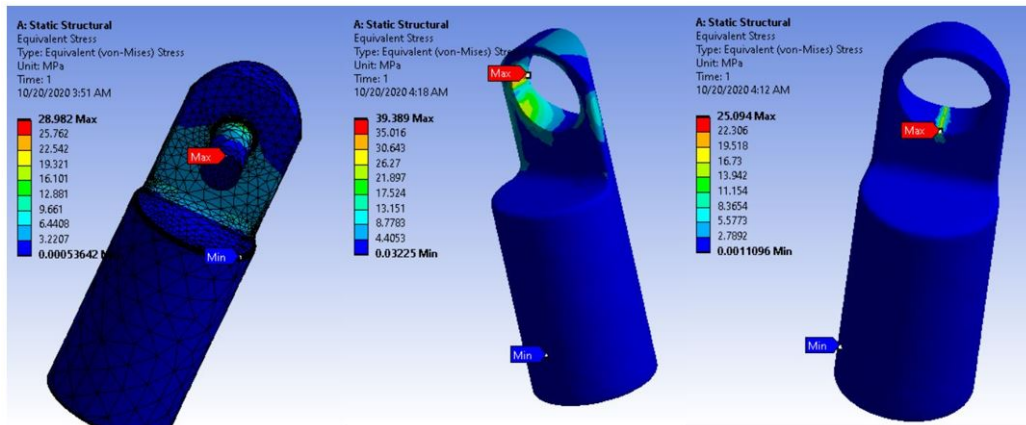


Figure 2.15: Design 3: Stress Analysis for Vertebrae 1 and 2 (Vertical and Side Loading).

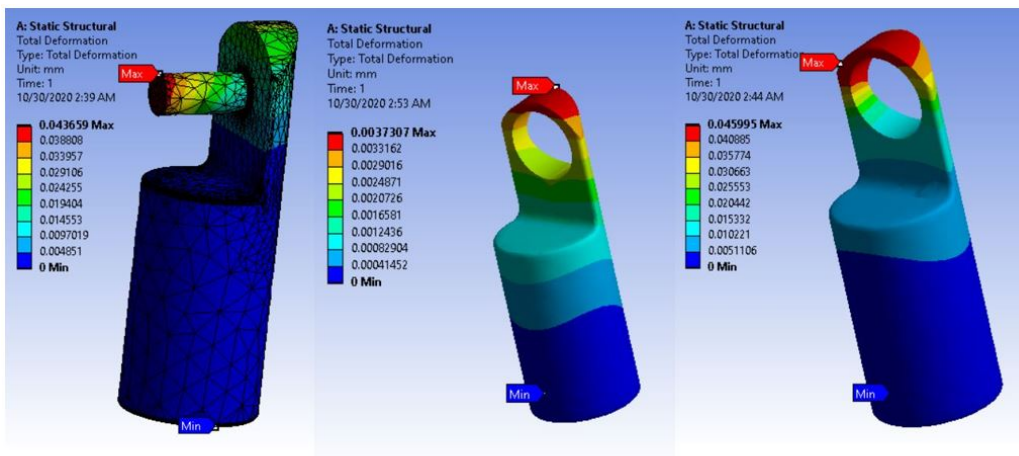


Figure 2.16: Design 3: Deflection for Vertebrae 1 and 2 (Vertical and Side Loading).

### Discussion of Static Failure Analysis Results for Designs 2 and 3

The stress analysis results for Designs 2 and 3 are presented in Tables 2.4 and 2.5. Design 2 results show that for Vertebra 1, the maximum stress of  $\sim 27MPa$  is located on the edge of the top pin hole when the pin diameter and pin hole diameter are 0.9 and 1.9mm. While that of Vertebra 2 is  $\sim 257MPa$  and located at the bottom pin region between the

fixed support and the link when the pin diameter and pin hole diameter are 0.3 and 1.3mm. These results show that decreasing the pin diameter (effectively increasing the pin hole diameter), decreases the stress on the surrounding structure of the pin hole of Vertebra 1 but increases the Vertebra 2 pin stress. The same behavior is expected for Design 3. Therefore, the dimensions for pin diameter and pin hole diameter are recommended in the range of 0.7 – 0.9mm and 1.7 – 1.9mm respectively.

These pin diameter and pin hole diameter ranges result in stresses in Vertebrae 1 and 2 that are below the ultimate tensile strength of 65MPa by a factor of 5.4 and 13 respectively. Therefore the structures are considered rigid and meet the specification of the desired contact load of 1 N. These results also show that Design 2 experienced significantly less structural stress than those evaluated for Design 3 with a factor of 1.65.

Side loading stress analysis evaluated on Vertebra 2 of Design 2 with a load capacity of 0.35N resulting in maximum stress of approximately 58MPa. In Tables 2.4 and 2.5, further stress analysis of the second vertebra of the module was not performed if the stress estimated on one vertebra of the single module is close to or higher than the material ultimate tensile strength.

Table 2.4: Design 2: Maximum Stresses Associated with Varied Pin and Pin Hole Diameter

Joint Geometry (mm)		Max. Stress (MPa) at 90°	
Pin Diameter	Pin Hole Diameter	Vertebra 1	Vertebra 2
0.9	1.9	26.842	4.455
0.7	1.7	19.059	6.090
0.5	1.5	12.096	12.166
0.3	1.3	5.416	257.620



Table 2.5: Design 3: Maximum Stresses Associated with Varied Pin and Pin Hole Diameter

Joint Geometry (mm)		Max. Stress (MPa)		
Pin Diameter	Pin Hole Diameter	Vertebra 1	Vertebra 2 (at 0 <sup>0</sup> )	Vertebra 2 (at 90 <sup>0</sup> )
0.9	1.9	28.982	25.094	39.389
0.7	1.7	50.927	Not Performed	Not Performed
0.5	1.5	119.960	Not Performed	Not Performed
0.3	1.3	478.760	Not Performed	Not Performed

The deflection results for the different joint geometry configurations are presented in Table 2.6. The results show that Design 3 experienced a greater deflection ( $\sim 21$  times) at the pin than that for Design 2. When a contact force of  $1N$  is applied on a vertically oriented Vertebra 2, the component with the pin hole shows that Design 2 has a slightly larger deflection than Design 3. Also, a side-loading deflection analysis is performed on Vertebra 2 of Design 2. These results suggest that Design 2 provides slightly better structural performance than Design 3, however further improvements might be required to the pin.

Table 2.6: Maximum Deflection due to Loading Conditions for Different Joint Designs

Joint Geometry		Max. Deflection ( $\mu\text{m}$ )		
Design	Component with Pin	Component with Pin Hole at 0 <sup>0</sup>	Component with Pin Hole at 90 <sup>0</sup>	Side Loading
Design 2	2.033	Not Performed	51.008	156.82
Design 3	43.659	3.7307	45.995	Not Performed

#### Design 4

The static failure analysis results of Designs 2 and 3, and SLA inverted vat polymerization fabrication requirements informed the next design improvement of the vertebrae components. Design 4 is an iteration of Design 2 since lower stress values were recorded in De-

sign 2 than in Design 3. However, the monolithically printed body-attached 3D printed pin is substituted for a stainless steel pin while the pin hole is reduced to reduce the expected stresses.

A pin hole diameters of  $0.54\text{mm}$  and  $0.60\text{mm}$  are designed into Vertebra 1 and Vertebra 2 respectively. It was intended that a stainless steel pin with a diameter of  $0.54\text{mm}$  is press fitted into Vertebra 1 while allowing clearance for Vertebra 2 to rotate. The hole sizes of  $0.54\text{mm}$  and  $0.60\text{mm}$  were chosen since they are in the range of hole dimensions that produced acceptable stress results as shown in Table 2.4. Design 4 is then set up with boundary conditions and structurally analyzed for failures in the same way as Design 2. Figure 2.17 shows the boundary conditions for Vertebra 1 and 2 and the joint pin for a  $1N$  reaction load when the single module bend angle is  $0^\circ$ . Figure 2.18 shows the resulting stresses for Vertebra 1 and 2, and the joint pin. Figure 2.19 shows the deformation due to the loading conditions.

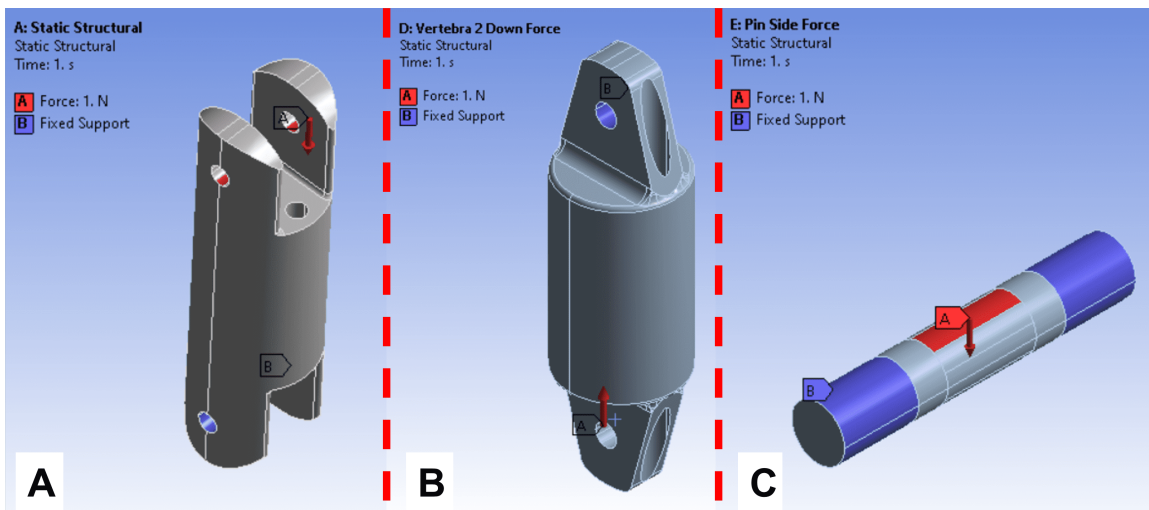


Figure 2.17: Design 4: Boundary Conditions. A. Vertebra 1, B. Vertebra 2, C. Joint Pin for a  $1N$  Reaction Load at  $0^\circ$  Bend Angle.

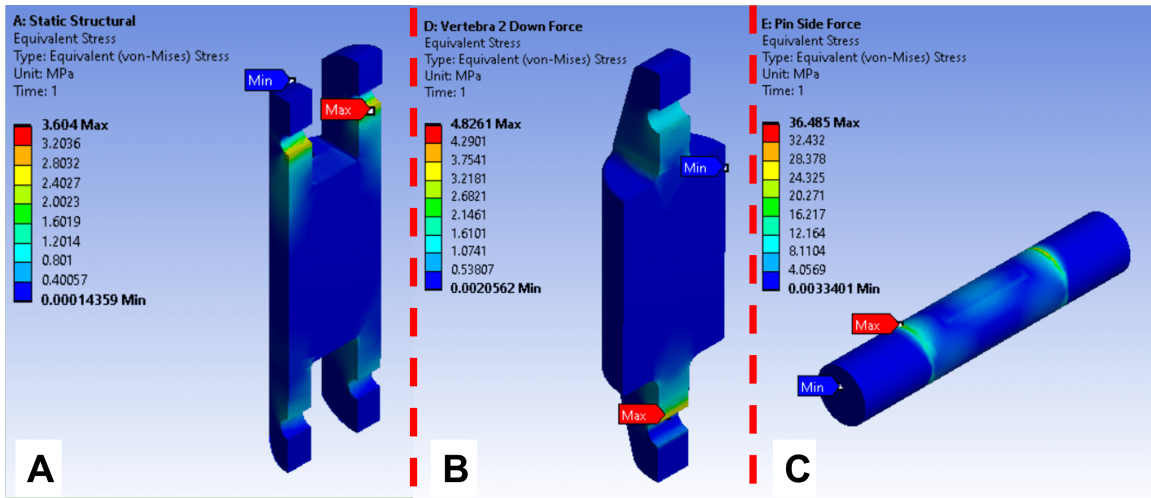


Figure 2.18: Design 4: Stresses. A. Vertebra 1, B. Vertebra 2, C. Joint Pin for a 1N Reaction Load at 0° Bend Angle.

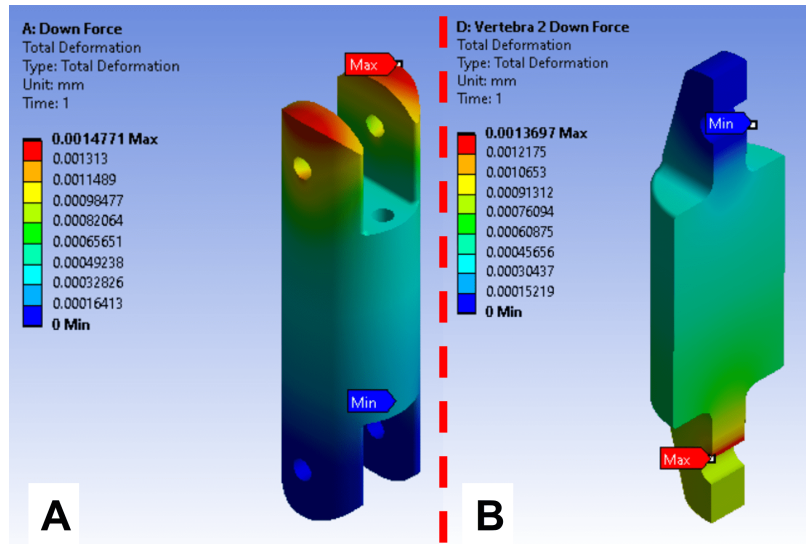


Figure 2.19: Design 4: Deformation. A. Vertebra 1, B. Vertebra 2 for a 1N Reaction Load at 0° Bend Angle.

The stress and deformation results in Figs. 2.18 and 2.19 show that this joint design and geometry significantly reduced the evaluated stresses from ranges of 12.10 – 19.10MPa to 3.60MPa in Vertebra 1 and 6.09 – 12.17MPa to 4.83MPa in Vertebra 2.

The boundary conditions for Design 4 are set up to simulate a reaction load on the joint when the continuum segment palpates tissue at 90° with structural analysis for failures evaluated as described before. Figure 2.20 shows the boundary conditions for Vertebra 1 and 2 for this case. Figure 2.21 shows the resulting stresses for Vertebra 1 and 2. Figure 2.22 shows the deformation due to the loading conditions. The stresses and deformations estimated at 90° bend angle were elevated. The maximum stresses are 24.87MPa on Vertebra 1 and 33.29MPa on Vertebra 2 which are approximately half of the ultimate tensile strength of the grey resin fabrication material. These results show slight structural improvement of the vertebrae designs as a result of more structural volume designed around the pin and pin hole as well as the use of the higher yield strength steel pin. However, Design 4 could be further improved to reduce possible lateral movements of Vertebra 2 due to the clearance between the joint pin and the joint hole of Vertebra 2.

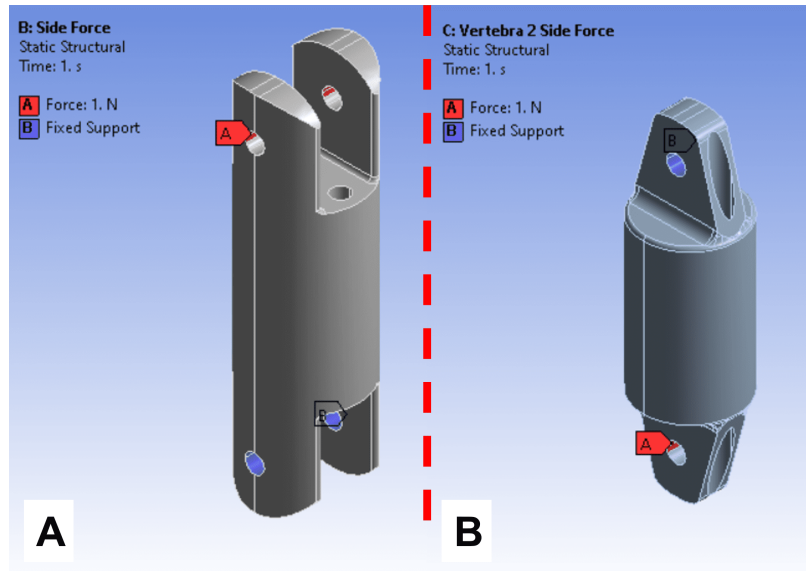


Figure 2.20: Design 4: Boundary Conditions. A. Vertebra 1, B. Vertebra 2 for a 1N Reaction Load at 90° Bend Angle.

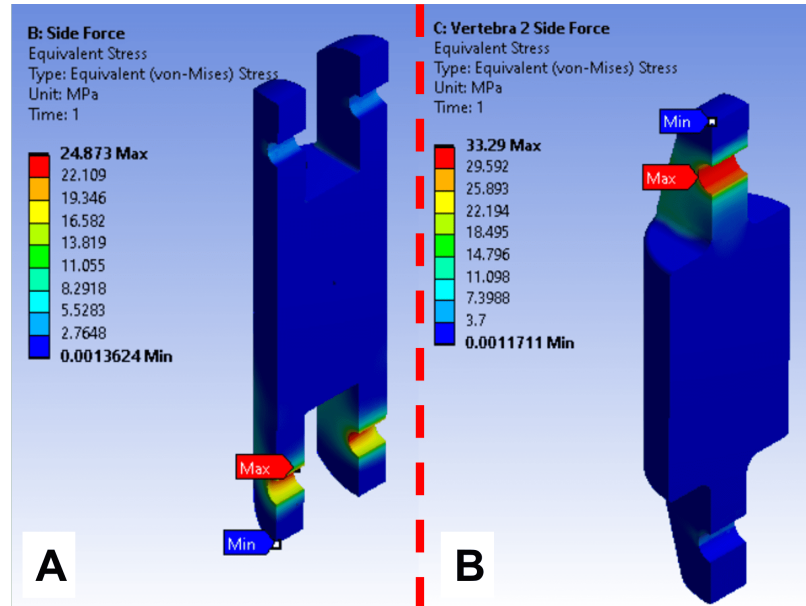


Figure 2.21: Design 4: Stresses. A. Vertebra 1, B. Vertebra 2 for a 1N Reaction Load at 90° Bend Angle.

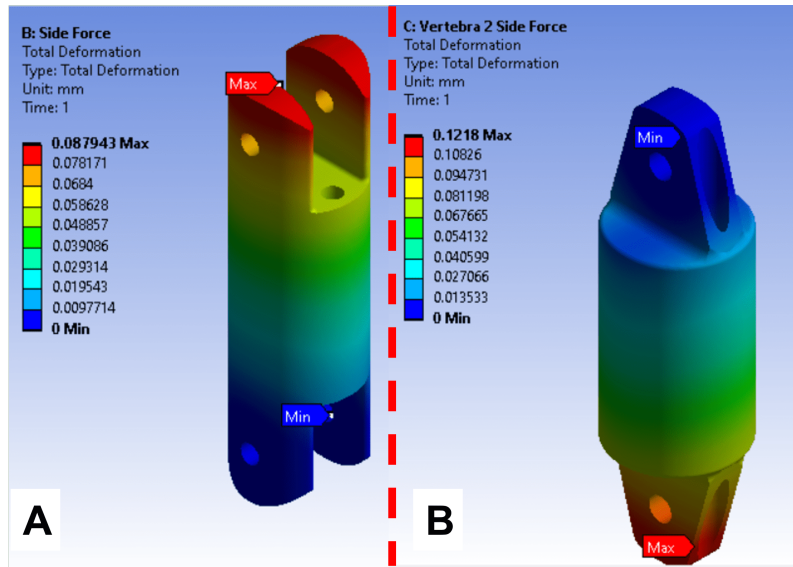


Figure 2.22: Design 4: Deformation. A. Vertebra 1, B. Vertebra 2 for a 1N Reaction Load at 90° Bend Angle.

## Design 5

Design 5 is a drastically different design from Design 4 and similar to Design 3. Design 5 was proposed to take advantage of the joint hole sizing range estimated to have the least stress in response to a reaction load while eliminating relative lateral motion between identical vertebrae. The joint hole for the vertebrae is  $0.54\text{mm}$  with countersinks to allow for a captive screw to be fitted and recess in the body of the vertebrae. Design 5 is set up and analyzed following the procedure described for previous designs. Figure 2.23 shows the boundary conditions, stresses, and deformation for the vertebra with 1N reaction load when the single module bend angle is  $0^\circ$ . Figure 2.24 shows the boundary conditions, stresses, and deformation for the vertebra with 1N reaction load when the single module bend angle is  $90^\circ$ . The resulting stresses from the  $90^\circ$  bend angle is  $71.31\text{MPa}$  and greater than the material ultimate yield strength. Hence, this design is not feasible even though it significantly reduces lateral motion.

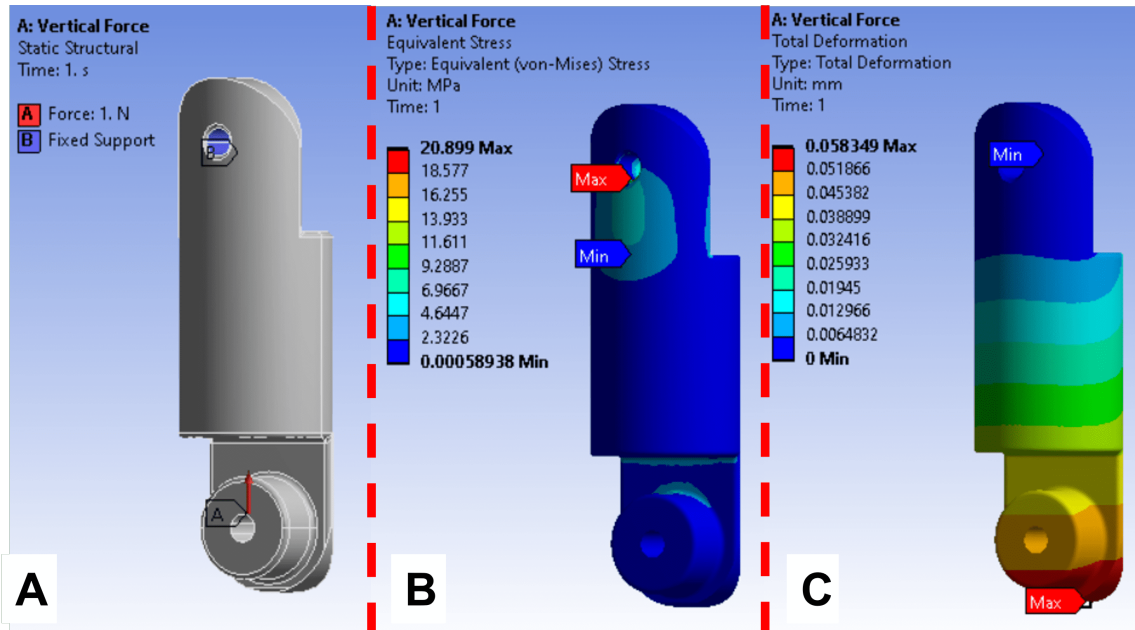


Figure 2.23: Design 5 at 0° Bend Angle. A. Vertebra Boundary Conditions, B. Vertebra Stresses for a 1N Reaction Load at 0° Bend Angle, C. Vertebra Deformation.

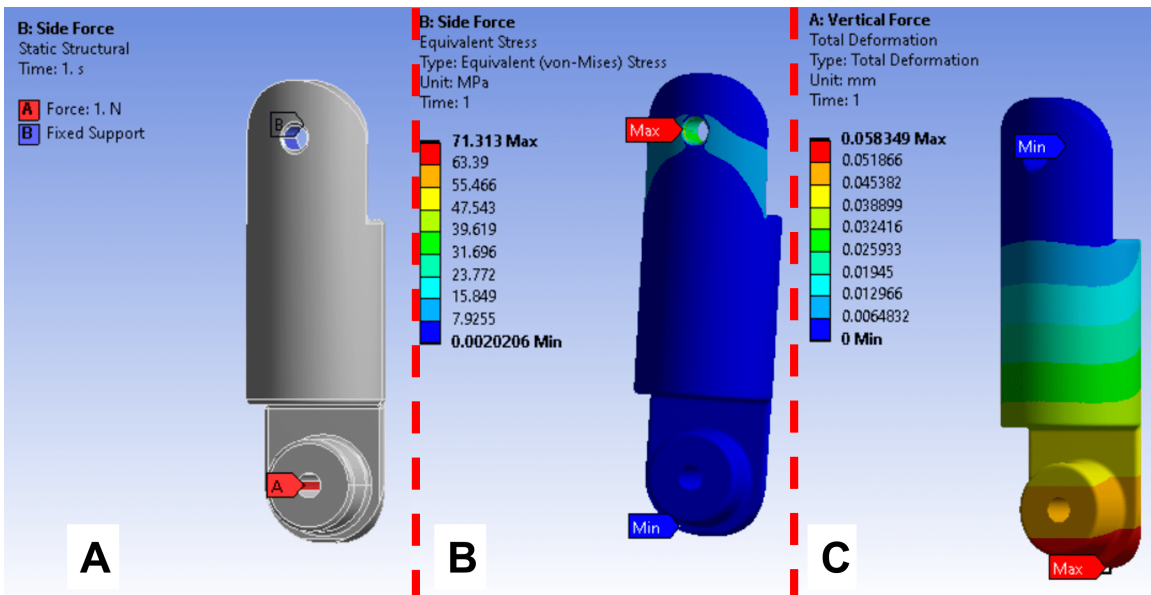


Figure 2.24: Design 5 at 90° Bend Angle. A. Vertebra Boundary Conditions, B. Vertebra Stresses for a 1N Reaction Load at 90° Bend Angle, C. Vertebra Deformation.

## Design 6

Doing away with the use of a joint captive pin altogether and to provide for ease of fabrication, Design 6 employs a snap-fit design configuration. The joint hole diameter in Vertebra 1 is  $1.11\text{mm}$  while the snap-in pin diameter is  $1.07\text{mm}$  with a chamfer to allow coupling the joint by snapping Vertebra 2 into Vertebra 1. The static failure analysis was performed and the results analyzed as with previous iterations. Figure 2.25 shows the boundary conditions for Vertebra 1 and 2 for a  $1\text{N}$  reaction load when the single module bend angle is  $0^\circ$ , and Fig. 2.26 shows the resulting stresses for Vertebra 1 and 2. Figure 2.27 shows the deformation due to the loading conditions.

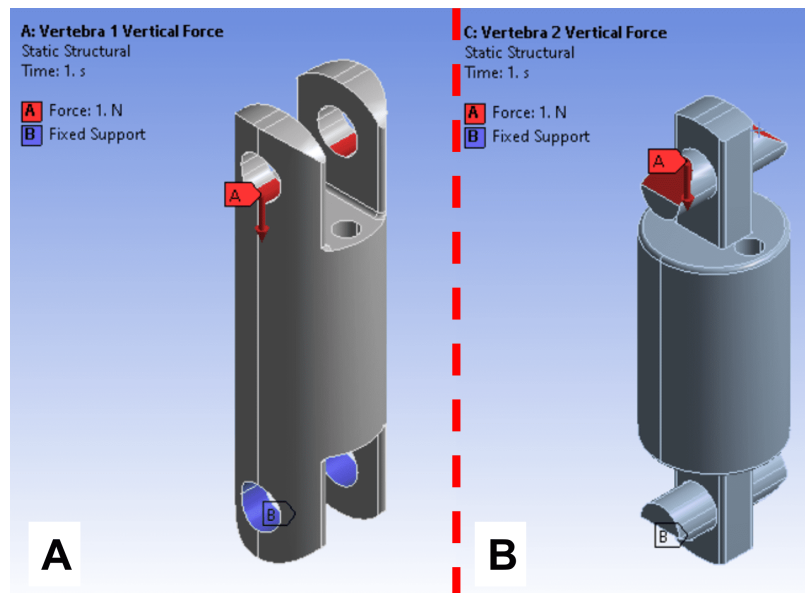


Figure 2.25: Design 6: Boundary Conditions. A. Vertebra 1, B. Vertebra 2 for a  $1\text{N}$  Reaction Load at  $0^\circ$  Bend Angle.



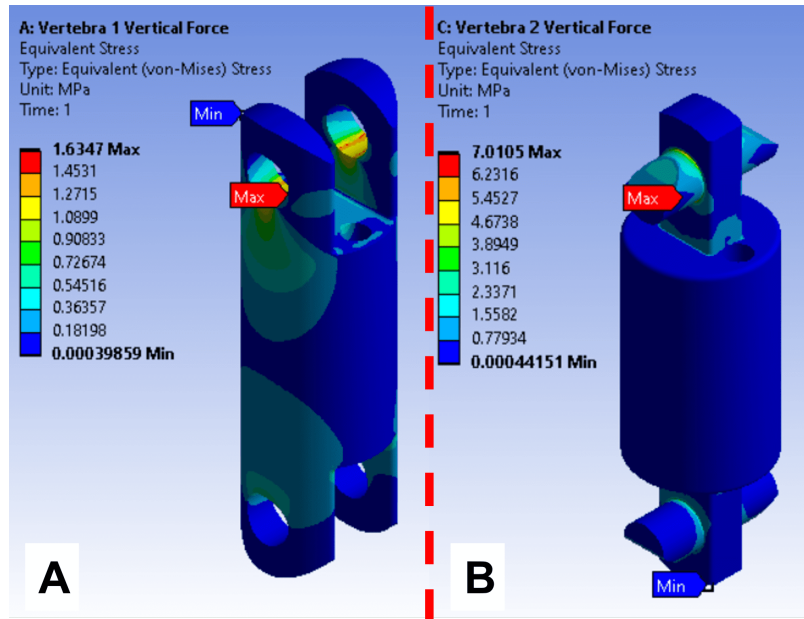


Figure 2.26: Design 6: Stresses. A. Vertebra 1, B. Vertebra 2 for a 1N Reaction Load at 0° Bend Angle.

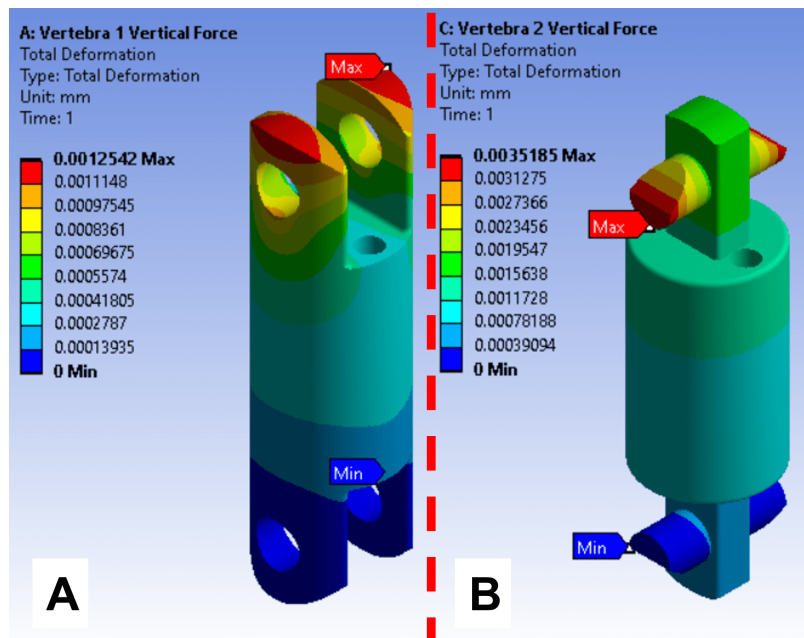


Figure 2.27: Design 6: Deformation. A. Vertebra 1, B. Vertebra 2 for a 1N Reaction Load at 0° Bend Angle.

The stress and deformation results in Figs. 2.26 and 2.27 show that the stresses of 1.64MPa in Vertebra 1 and 7.01MPa in Vertebra 2 are lower than that for Design 4 even though the snap-in joint hole was increased and the pin, which is non-metal, is a body attached monolithically printed snap-in pin.

The boundary conditions for Design 6 are set up to simulate a reaction load on the joint at 90° tissue palpation. The structural analysis is performed in the same way as described before. Figure 2.28 shows the boundary conditions for Vertebra 1 and 2 for this case. Figure 2.29 shows the resulting stresses for Vertebra 1 and 2, and Fig. 2.30 shows the deformation due to the loading conditions. The stresses and deformations estimated at 90° bend angle were shown to be elevated. The maximum stress of 102.58MPa is significantly more than the material ultimate tensile strength as the reaction force acts on the non-chamfered surface. Relative lateral motion between Vertebrae 1 and 2 may also exist in Design 6. These results suggest that designing a chamfer in the pin may reduce the stress concentration on the pin by redirecting the direction of the reaction load due to the applied load. Likewise, a kinematic constraint that eliminates lateral motion at the joint between Vertebrae 1 and 2 will improve the single module motion performance.

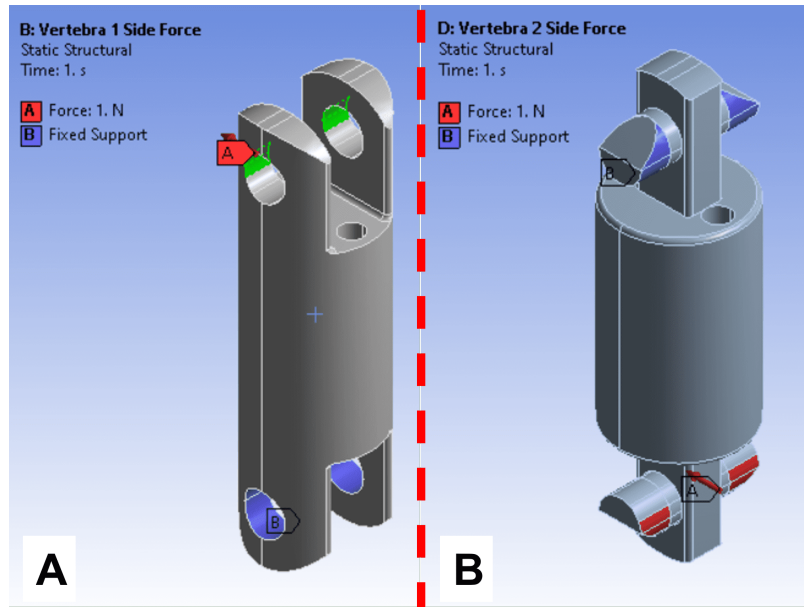


Figure 2.28: Design 6: Boundary Conditions. A. Vertebra 1, B. Vertebra 2 for a 1N Reaction Load at 90° Bend Angle.

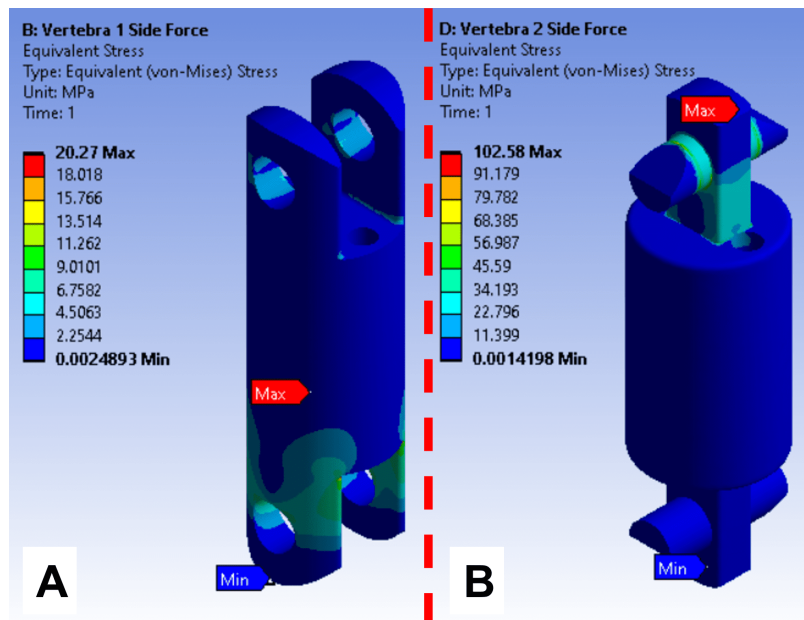


Figure 2.29: Design 6: Stresses. A. Vertebra 1, B. Vertebra 2 for a 1N Reaction Load at 90° Bend Angle.

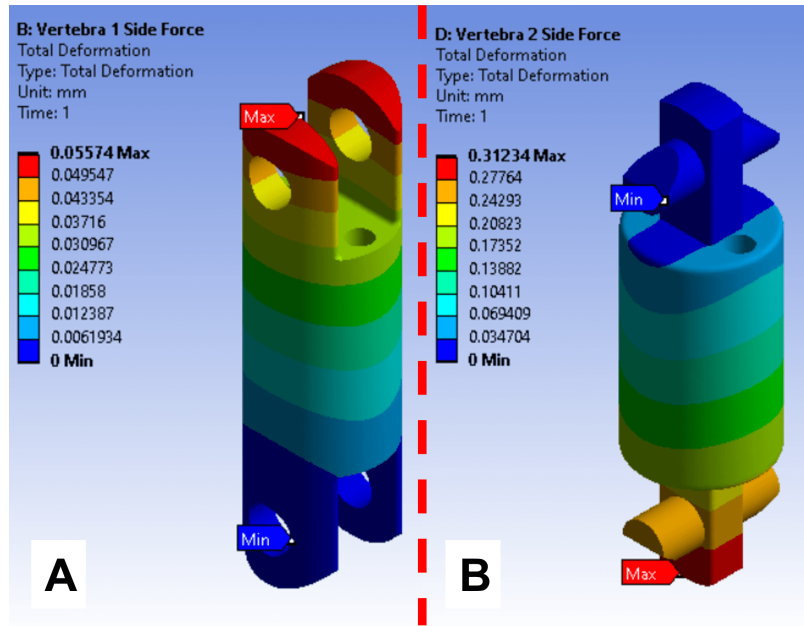


Figure 2.30: Design 6: Deformation. A. Vertebra 1, B. Vertebra 2 for a 1N Reaction Load at 90° Bend Angle.

## Design 7

Design 7 was developed to take advantage of the interior redistribution of reaction forces and address the relative lateral motion between Vertebrae 1 and 2. The interior redistribution of the reaction forces is accomplished by redesigning the joint snap-in features. The through hole that served as the pin hole in Design 6 is substituted for a recessed snap-in female feature that interfaces with the snap-in male feature that serves as the pin. This joint design also improves the fabrication and assembly of the module. Figure 2.31 shows the boundary conditions for the vertebra for a 1N reaction load when the single module bend angle is 0°, the resulting stresses and the deformation due to the loading conditions. Figure 2.32 presents the boundary conditions, stress, and deformation for single module bend angle 90°.

The maximum stress estimated is  $17.68\text{MPa}$  which gives this design a FoS of 3.68. Likewise, the maximum deformation of  $0.0018\text{mm}$  is considered negligible relative to the size of the vertebrae and does not pose any deflection challenge to the vertebrae that may lead to motion or displacement errors.

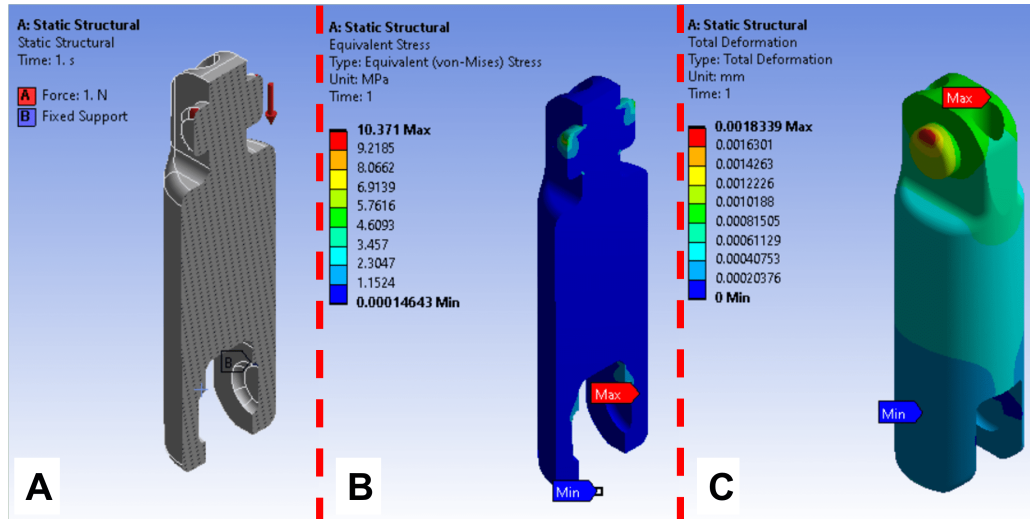


Figure 2.31: Design 7. A. Boundary Conditions, B. Stresses, C. Deformation for 1N Reaction Load at  $0^\circ$  Bend Angle.

## 2.5 Geometric Optimization of Robot Continuum Segment Module for Maximum Tension-Bend Angle Sensitivity

In section 2.4, a static failure analysis was performed to evaluate the acceptable joint design for the structural integrity of the continuum module given the fabrication material of choice. The static failure analysis assisted in deciding the acceptable joint pin and hole geometric values. However, the experimental analysis (to be discussed in Chapter 4) revealed that the joint active length is an important component of the robot continuum module performance. Therefore, a design optimization approach using the continuum segment quasi-static formulation (discussed in section 3.3) could be developed to estimate the optimal

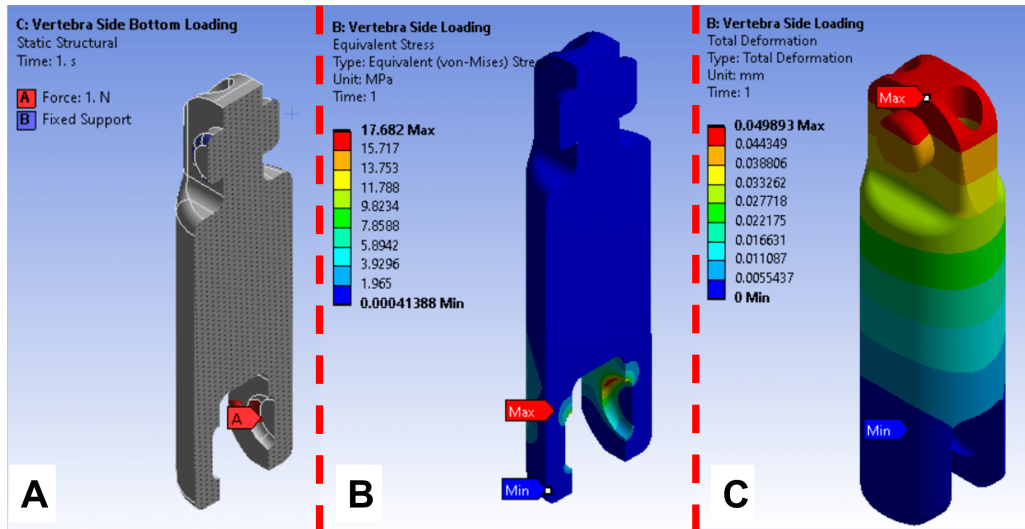


Figure 2.32: Design 7. A. Boundary Conditions, B. Stresses, C. Deformation for 1N Reaction Load at 90° Bend Angle.

design geometric parameters with acceptable FoS. Once formulated, the design optimization approach could be used to find multiple combinations of design parameters such as the joint length, distance of the tendon from the continuum central axis, and the length of the vertebra cylindrical component that meet the constraints with the objective of maximizing the continuum segment bend angle for a given applied tension or minimizing the applied tension for a given bend angle.

### 2.5.1 Geometric Design Optimization Formulation

Important to the formulation of the objective function are Eqs. 3.21-3.23, which present the quasi-static model of a single module and relate the applied tension to the module bend angle, material, and geometric properties of the tube and other joint and vertebrae geometry. These equations can be parametrically solved to find the tendon tension values,  $T_1$  or  $T_2$  or  $T_1 + T_2$ , as a nonlinear multivariable function,  $f(\bar{x})$ . Where  $\bar{x}$  is a vector of any combination of the single module design parameters such as bend angle  $\theta$ , active joint lengths  $l_1$  and  $l_2$ , vertebrae length  $l_v$ , tube material property, outer diameter, and thickness

$\mu$ ,  $D$ , and  $t$  respectively, and the distance from the tendon to the central axis  $r_T$ . An optimization problem can be defined where the objective is to estimate the values of  $\bar{x}$  such that  $f(\bar{x})$  is minimum subject to constraints as presented in Eq. 2.1. There are a plethora of nonlinear constrained optimization algorithms, however, the algorithm used in this research is the “Interior Point Algorithm”.

$$\begin{aligned} \min_{\bar{x}} f(\bar{x}) &= T_1(\theta, T_2, F_C, l_1, l_2, l_v, r_T, D, \mu), \\ \text{subject to } &\left\{ \begin{array}{l} \text{Joint collision constraint} \\ D \geq d + t_{min} \\ l_1 \geq L_{min} \\ l_2 \geq L_{min} \\ 0 < r_T \leq \frac{d}{2} - w_{min} \end{array} \right. \end{aligned} \quad (2.1)$$

where  $\bar{x} = (D, l_1, l_2, r_T)$  is the design variable vector;  $D$  is the outer tube diameter,  $d$  is the vertebra diameter,  $t_{min}$  is minimum tube thickness,  $L_{min}$  is minimum feasible link length, and  $w_{min}$  is minimum feasible vertebra wall thickness.

The interior point algorithm (presented by Byrd *et al.* [64, 65] and Waltz *et al.* [66]) minimizes a constrained problem (Eq. 2.2) by solving a sequence of approximate minimization problems given as Eq. 2.3 for the barrier parameter  $\mu_f > 0$ . To solve the approximate problem, the algorithm uses either a direct step in  $(x, s)$  or the conjugate gradient step, where  $s$  are additional variables introduced into the linear constraints to transform them from inequality constraints to equality constraints

$$\begin{aligned} \min_x f(x), \\ \text{subject to } h(x) = 0 \text{ and } g(x) \leq 0 \end{aligned} \quad (2.2)$$

where  $h(x)$  and  $g(x)$  are equality and inequality constraints respectively.

$$\min_{x,s} f_{\mu_f}(x, s) = \min_{x,s} f_{\mu_f}(x) - \mu_f \sum_i \ln s_i, \quad (2.3)$$

subject to  $s \geq 0$ ,  $h(x) = 0$  and  $g(x) + s = 0$ .

The geometric design optimization interior point algorithm is implemented using the MATLAB<sup>®</sup> function *fmincon*. Evaluating the design architecture for improved performance of the hybrid flexible-rigid manipulator with multi-dependent parameters and geometric descriptions is the significance of the design optimization analysis in this research. For example, given a set of joint tubes with different shear modulus ( $\mu$ ) or thickness, the design optimization analysis can estimate the values for the single module geometric parameters for improved performance and desired tension-bend angle response or joint configuration due to a tendon-applied load.

### 2.5.2 Establishing Constraints

The robot self-collision analysis was performed to study the range of possible robot motions for varied geometrical parameters. This analysis is important to understand what joint constraints can be defined as an input to the design optimization formulation. Primarily, a joint constraint could be implemented to avoid robot self-collision in such a way that limits rotation about the X, Y, and Z axis independently. Therefore, the kinematic formulations (developed in section 3.1) were used for a single module (Fig. 2.7b) with the varied geometric values presented in Fig. 2.33 and Table 2.7.



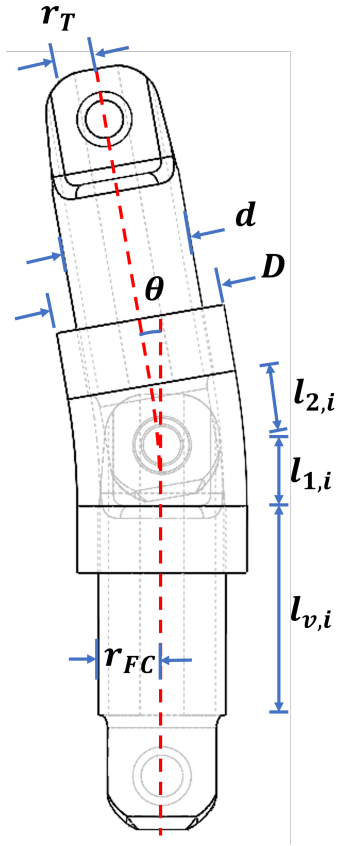


Figure 2.33: Schematic of Single Module Showing Geometric Design Variables.

Table 2.7: Single Module Geometric Parameters

Geometric Parameters	Values
Outer diameter of the elastic joint tube, $D(mm)$	4.00
Outer diameter of vertebra, $d(mm)$	3.00
Length of vertebrae cylindrical section, $l_{v,i}(mm)$	4.00
Length of vertebrae lower pivot link, $l_{1,i}(mm)$	1.50
Length of vertebrae upper pivot link, $l_{2,i}(mm)$	1.50
Joint Length, $L = (l_{1,i} + l_{2,i})$	
Vertebrae radius, $r_{FC} = d/2$	
Robot bend angle, $\theta(^{\circ})$	90
Tube Shear Modulus, $\mu(Nmm^{-2})$	0.22
Vertebrae Weight, $W_i = \rho Vg$	

where  $\rho$  and  $V$  are the  $i^{th}$  vertebra density, volume and  $g$  is gravity.

The single module geometry consisting of 2 vertebrae labeled  $A$  and  $B$ , and body-attached points of interest,  $A_1$ ,  $A_2$ ,  $B_1$ , and  $B_2$  is shown in Fig. 2.34. The kinematics of the single module was evaluated for multiple arbitrary geometric parameters that were manually assigned and studied for self-collision for a bend angle range. The results for the motion of  $B_1(x, y)$  relative to  $A_2(x, y)$  for one of the multiple studies are plotted in Fig. 2.35.

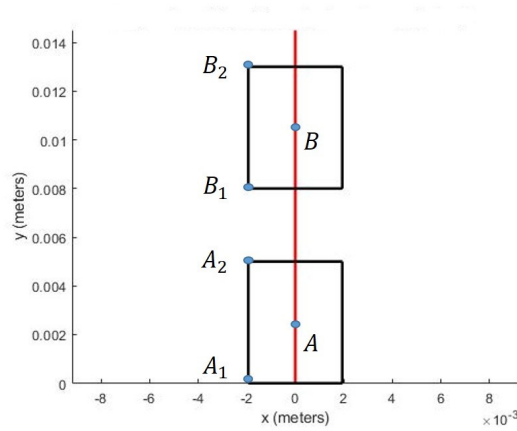
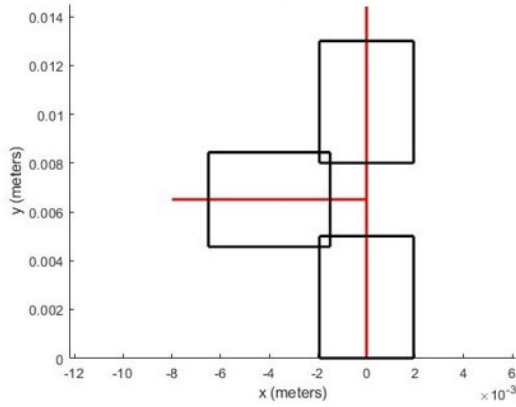


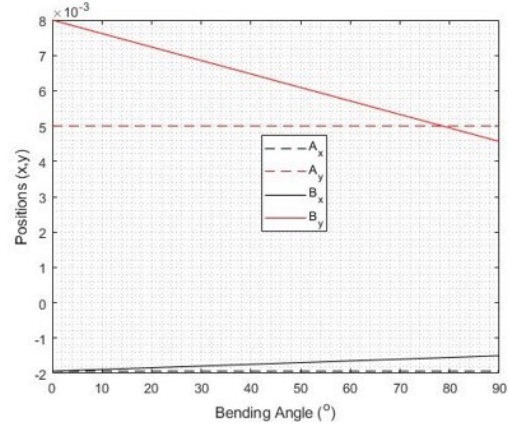
Figure 2.34: Kinematics of 2-vertebrae for bending angle  $\theta = 0^\circ$ .

The results presented in Fig 2.35, for example, show that edge collisions may occur. Increasing  $l_2$  will increase the bend angle attainable than for when  $l_1 = l_2$ , however, a self-collision is inevitable at some bend angle. If  $l_1 > l_2$ , an edge collision may be avoided but not a side collision of the  $i^{th}$  vertebra with the edge of  $(i - 1)^{th}$  vertebra. Likewise, increasing the diameter of the vertebrae may reduce the bend angle attainable before collision even if the lengths of the links  $l_1$  and  $l_2$  are held constant. These results show, as expected, that the geometry of the robot design strongly affects the joint motion limits and the maximum bending angle obtainable by the continuum segment before self-collision occurs. This analysis suggests that a constraint to account for both edge and side collisions

between the  $i$ th and the  $(i - 1)$ th vertebrae must be considered in a design optimization that aims to find the optimal geometric solutions.



(a) Schematic Showing Pose of Robot.



(b) Position of  $B_1$  w.r.t  $A_2$

Figure 2.35: Kinematics of 2-Vertebrae for Bending Angle,  $\theta = 0^0 : 90^0$  using  $d = 2.07l_1$ ,  $l_1 = l_2$ , and  $r_{FC} = 990\mu m$ .

The edge and side collision constraint is formulated from the slope equality condition presented in Eq. 2.4, where the leading edge on the  $(n - 1)^{th}$  vertebra exists in the set of coordinates on the slope of the  $n^{th}$  vertebra edge.

$$\frac{A_{2y}}{A_{2x}} = \frac{B_{2y} - B_{1y}}{B_{2x} - B_{1x}} \quad (2.4)$$

The constraint that accounts for edge and side collision,  $g(1)$ , is presented in Eq. 2.5.

$$g(1) = A_{2y}(B_{2x} - B_{1x}) - A_{2x}(B_{2y} - B_{1y}) < 0 \quad (2.5)$$

Other constraints applied relate to the manufacturing feasibility of the design geometric variables and are presented in Eq. 2.6

$$\begin{aligned}
g(2) &= D - d - t_{min} > 0 \\
g(3) &= l_1 - L_{min} > 0 \\
g(4) &= l_2 - L_{min} > 0 \\
g(5) &= 0.5d - r_T - w_{min} > 0
\end{aligned} \tag{2.6}$$

where  $t_{min} = 0.2mm$ ,  $L_{min} = 1.5mm$ , and  $w_{min} = 0.2mm$ .

Initial studies were performed to estimate the optimal combination of the link lengths,  $l_1$  and  $l_2$ , tube diameter,  $D$ , and distance of the tendon to the central axis,  $r_T$ , for a minimum actuating tension using the geometric design optimization problem defined in Eqs. 2.2-2.6. The lower,  $X_L$ , and upper,  $X_U$ , boundary conditions for the design variables are defined as  $X_L = \{r_T = 1, D = 2.5, l_1 = 2.5, l_2 = 2.5\} mm$  and  $X_U = \{r_T = 10, D = 10, l_1 = 10, l_2 = 10\} mm$  respectively, with initial values  $X_0 = \{r_T = 2.5, D = 2.5, l_1 = 2.5, l_2 = 2.5\} mm$ . The tension results, based on the optimal design variables values are compared to the tension results from the as-designed state and are presented in Table 2.8. Using the constants for the design variables in Table 2.7, the optimal values are estimated as  $(r_T, D, l_1, \text{ and } l_2) = (1.30, 3.20, 1.55, \text{ and } 7.11)mm$  respectively for an optimal applied tension of  $2.49N$  with the design variable history plotted in Fig. 2.36. If the elastic tube shear modulus,  $\mu$ , is changed from  $0.22Nmm^{-2}$  to  $2Nmm^{-2}$ , the optimal values are estimated to be  $(r_T, D, l_1, \text{ and } l_2) = (1.30, 3.20, 1.55 \text{ and } 7.11)mm$  respectively with an optimal applied tension of  $22.61N$  and with the design variable history plotted in Fig. 2.37. The optimal design variable solutions were manually verified that they do not violate the constraints.

The tensions obtained with the optimal design variables are compared to the tensions obtained using the as-designed module parameter values (without optimization) (presented in section 3.3) for  $\mu = 0.22Nmm^{-2}$  and  $\mu = 2Nmm^{-2}$  for a bend angle of  $90^\circ$ . The

Table 2.8: Design Variable Values for As-Designed and Optimized

Design Variable	Design Variable Values As-Designed, Not Optimized		Design Variable Values Optimized	
	$\mu = 0.22Nmm^{-2}$	$\mu = 2Nmm^{-2}$	$\mu = 0.22Nmm^{-2}$	$\mu = 2Nmm^{-2}$
$r_T(mm)$	1.00	1.00	1.30	1.30
$D(mm)$	4.00	4.00	3.20	3.20
$l_1(mm)$	1.50	1.50	1.55	1.55
$l_2(mm)$	1.50	1.50	7.11	7.11
$T(N)$	11.38	103.5	2.49	22.61

optimized tensions are  $2.49N$  and  $22.61N$  compared to the non-optimized ones of  $11.38N$  and  $103.5N$  yielding a reduction of  $\sim 4.58$  times. The design optimization algorithm was able to achieve a reduction of tensions by  $\sim 0.22$  times by increasing the joint moment arm variables  $r_T = 1.30mm$  and  $l_2 = 7.11mm$  compared to the as-designed  $r_T = 1.00mm$  and  $l_2 = 1.5mm$ , and reduced the elastic tube thickness to  $(D - d)/2 = (3.20 - 3)/2 = 0.1mm$  compared to the as-designed  $(D - d)/2 = (4 - 3)/2 = 0.5mm$ . Reduction in the required tension as a result of the design optimization analysis aids in the reduction of stresses on the vertebrae components and therefore, improves the structural integrity of the vertebra and continuum segment. Given the material used to fabricate the continuum module, an applied tension of  $103.5N$  on the body of the vertebrae may easily cause a structural failure of the robot before an actuation is achieved.

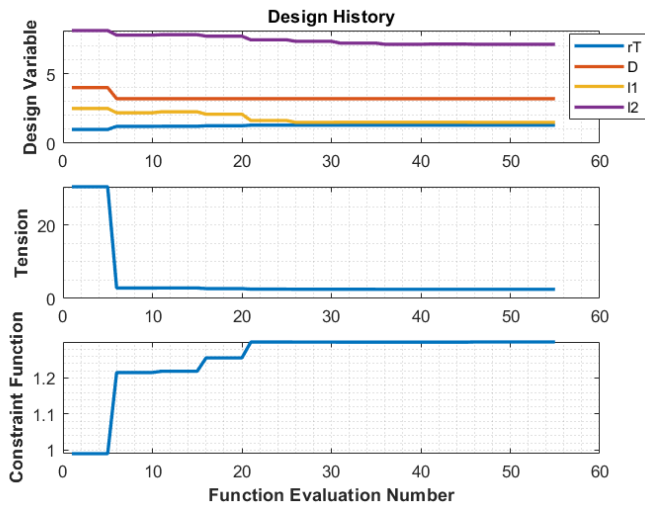


Figure 2.36: Design Variable Iteration History for  $\mu = 0.22Nmm^{-2}$ .

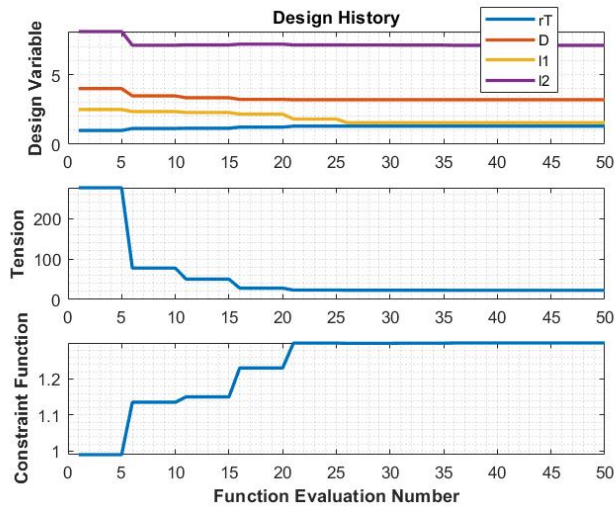


Figure 2.37: Design Variable Iteration History for  $\mu = 2Nmm^{-2}$ .

## 2.6 Initial Prototyping of Robot Continuum Segment

The vertebrae components for the continuum robot segment are designed in Solidworks® (SolidWorks Corp., Waltham, MA) (see Fig. 2.38a) and fabricated for (3, 6, 9, 12)mm joint

lengths for a  $0.8\text{mm}$  tendon diameter using resin based additive manufacturing. Fabrication experiments were performed with Photon-S™ (Anycubic Technology Co. Ltd., Kowloon, Hong Kong, China) SLA 3D printer with clear resin and Form3™ (Formlabs® Inc., San Francisco, California) SLA 3D printer with grey resin. The manufacturer-recommended procedures and default print settings were followed while printing, washing, and curing the vertebrae. Figure 2.38 shows the entire fabrication flowchart. During preliminary experiments, it was found that the Photon-S™ SLA 3D printer provided relatively better results with additional post-processing measures.

After the default print settings (see Fig. 2.38b) were defined, the vertebrae were oriented upright with the vertebrae link that has the male snap-in features closest to the print bed and raised  $4\text{mm}$  from the print bed to facilitate resin drainage from the vertebrae interior channels as shown in Fig. 2.38c. These channels function as a guide for the actuation tendons and sensor cables from the base to the end of the micro-robot. Once printing is completed (see Fig. 2.38d), an additional post-processing step of pre-washing the vertebrae with a  $50\text{ml}$  Isopropyl Alcohol (IPA) filled syringe and needle to remove leftover resin from the vertebrae channels and features is completed. This step has been found to greatly improve the quality of the printed vertebrae. The printed vertebrae components were then washed in an IPA bath for 5 minutes and then cured for 30 minutes using a Wash and Cure machine 2.0™ (Anycubic Technology® Co. Ltd.) using default settings and shown in Fig. 2.38e. Distinct features of a printed vertebra such as tendon guide channels and male and female snap-in connections along with key dimensional measurements are shown in Figs. 2.39a and 2.39b respectively. The fabricated vertebra demonstrated good dimensional accuracy with a maximum deviation of  $\sim 0.4\text{mm}$  (shown in Fig. 2.39c) compared to as designed dimensions. This deviation is a result of volume loss and thermal contraction during and after the curing process [67].

The cured vertebrae are assembled by engaging the snap-in joint locking mechanism, then tendons are routed through the internal channels, and the assembly is inserted into elastic tubes to form the continuum segment of the robot. A 3-module representative section of the continuum robot with 3-joints (4-vertebrae) along with the micro-force sensor assembly is shown in Fig. 2.38f.

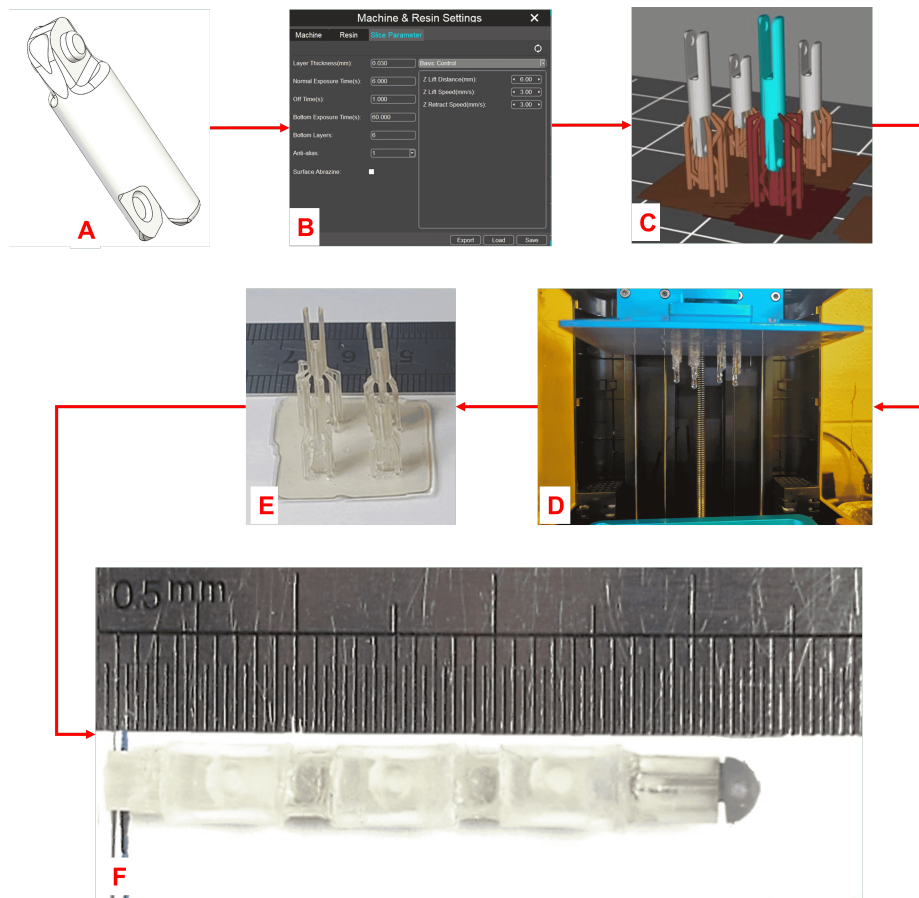


Figure 2.38: Vertebrae Fabrication Steps. A. CAD Vertebra Model, B. Print Settings in Photon™ Workshop, C. Vertebrae Oriented with Support and Sliced, D. Vertebrae on the Build Platform after Printing, E. Vertebrae Washed and Cured using the Washing and Cure Machine, F. Vertebrae Assembly for a 3 Joint Continuum Module.



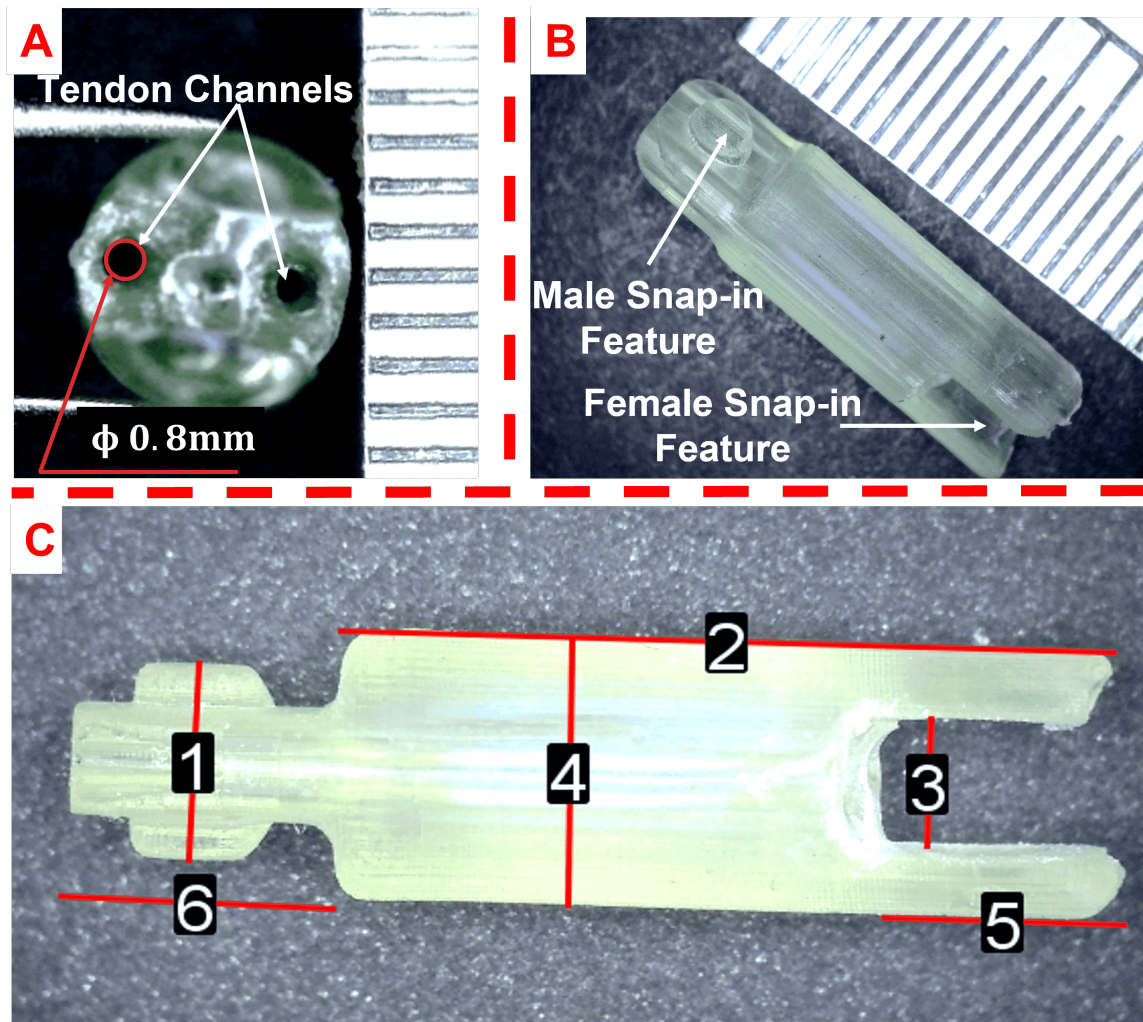


Figure 2.39: Vertebra with 3mm Joint Length features. A. Tendon Channels, B. Male and Female Snap-in Features, C. Key Dimensions Indicated as (1, 2, 3, 4, 5, 6) are (2.1, 7.4, 1.4, 2.9, 2.3, 2.6) $mm$  as Measured Respectively. Compared to (2.2, 7.7, 1.5, 3.0, 2.7, 2.7) $mm$  as designed.

## 2.7 Continuum Segment Manufacturing: Investigation into Rapid Prototyping

*Disclaimer: This research started and is based on the preliminary experiments I (Samson Adejokun) performed towards prototyping of the proposed continuum microrobot. Based on the observations of these preliminary experiments and further discussions with Dr. Shiakolas and committee member Dr. Ravi*

*(University of Cincinnati), Dr. Shiakolas, Mr. Adejokun, and Dr. Ravi conceived the proposed methodology to investigate the effects of printing process parameters on the print quality of the vertebrae on three different inverted vat polymerization printers. Mr. Adejokun conducted experiments on the Anycubic 3D printing platform and evaluated all measured data, Mr. Tushar Saini, Ph.D. student at MARS lab advised by Dr. Shiakolas, developed the imaging fixture, automatic imaging algorithm and imaged the manufactured parts, and Mr. Shivum Chokshi (University of Cincinnati under Dr. Ravi) conducted experiments on the Formlabs Form 3 and Peopoly Phenom 3D printing platforms and measured the geometry of interest from the images of the manufactured parts.*

In section 2.6, multiple quality and dimensional variations were identified in initial fabrication experiments of the vertebra of the continuum segment depending on the additive manufacturing method used. These manufacturing uncertainties have adverse effects on the overall performance of the continuum segment of the micro-robotic manipulator [68]. Therefore, an investigation was undertaken to identify fabrication and process parameters to minimize manufacturing defects and dimensional variations. This investigation is also critical to the predictive manipulation of the continuum segment of the robotic manipulator. Figure 2.40 shows possible manufacturing defects; the degree of occlusion of the tendon channels, shown in Fig. 2.40a, will result in assembly difficulty or in greater friction due to the relative motion between the tendon and a narrower, non-uniform tendon channel, or the degree of dimensional instability between the as-designed and fabricated component, shown in Fig. 2.40b, could contribute to the bend angle-tension behavior uncertainty and increase the divergence between the theoretical model and the actual behavior of the continuum segment extending to the overall micro-robotic manipulator.

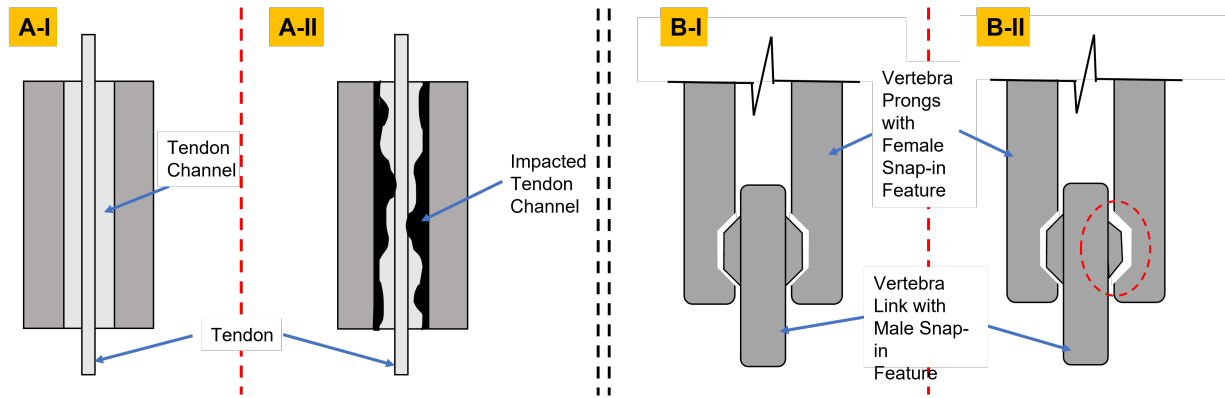


Figure 2.40: Schematic Showing Possible Manufacturing Defects and Dimensional Variations. A-I. As-Designed Tendon Channel, A-II. Impacted Tendon Channel, B-I. As-Designed Continuum Module Joint with vertebra prong, Male and Female Snap-in Features, B-II. Continuum Module Joint with Dimensional Variation in Male Snap-in Feature.

The application of additive manufacturing in the prototyping and manufacturing of medical devices has received significant attention due to its versatility in manufacturing parts with complex geometries compared to traditional manufacturing methods and customized properties by combining different materials [69, 70]. The U.S Food and Drug Administration (FDA), the regulating body responsible for public health, has recognized and approved the use of additive manufacturing for implants, surgical devices and prosthetics [71]. Additive manufacturing technologies can be categorized by their fabrication process which includes Selective Laser Sintering (SLS), Stereolithography (SLA) or Fused Deposition Modeling (FDM). In the research and development of the micro-robotic manipulator for transurethral bladder tissue diagnosis, SLA-based additive manufacturing platforms have been employed due to their ability to produce small detailed components in the scale of interest, cost to quality ratio and availability [70]. Examples of medical devices manufactured using SLA-based additive manufacturing platforms and the respective biocompatible materials used for manufacturing are discussed by Guttridge *et al.* [72].

The use of SLA for manufacturing requires the user to define certain process parameters. These process parameters are inputs that affect the quality of parts and determine the success or failure of the process and the quality of the manufactured component. The process parameters for SLA may include [73];

- Layer thickness or height (mm): The height of an individual layer of a multi-layer part. It affects the printing time and the amount of details of the part.
- Bottom layer exposure time (s): The time required to cure resin onto the print bed (or plate) to form each layer of the first few support layers before starting printing the actual part. It affects the quality and print success of the part.
- Normal layer exposure time (s): The time required to cure resin to form each subsequent layer of the part. It also affects the quality and print success of the part.
- Off time (s): The time between the *On/Off* states of the UV-light source when the layers of the part are being cured. It affects the print success of the part due to the partial or complete build of each layer of the part.
- Lift speed (mm/s): The speed at which the print bed is moved away from the resin bath after each layer exposure. It affects how the model is peeled from the thermo-plastic film between the print bed and the UV-curing source.
- Retract speed (mm/s): Similar to the lift speed, the retract speed is the speed at which the print bed is moved towards the resin bath.
- Lift height (mm): The distance at which the print bed is moved up away from the resin bath after each layer exposure. It affects the print success similar to the lift speed.

- Anti-aliasing: This is the edge smoothing or resolution parameter that affects how detailed the manufactured parts are.
- Supports: These are structures inserted by the pre-processing software and built by the 3D printer to support the actual part during the fabrication.
- Model orientation (degrees): It defines how the part is oriented with respect to the print bed and affects the print success of the part considering part geometry and features.
- Wash time: The time the part is washed in a washing machine to completely remove uncured and residue resin on the part after printing.
- Cure time: The time the part is in direct exposure in the curing machine after printing and washing to completely cure the part.

The manufacturer of the SLA technology usually suggests baseline values for these process parameters but defects and failures in manufactured parts are not uncommon using default values particularly due to the uniqueness of part designs which demands the definition of different combinations of the process parameters. Experimentally identifying combinations of process parameters could lead to minimizing dimensional variations and improve the quality and success of produced parts [70]. An investigation into a cross-platform performance evaluation as a result of these process parameters and other pre- and post-print factors is the focus of this section.

Using the preliminary manufacturing experiments discussed in section 2.6, the process parameters of interest for the manufacturing of the vertebra components of the continuum segment were identified to be the layer height, model orientation, and resin color while other parameters enumerated above were left at their manufacturer recommended values. For a cross-platform evaluation, the resin-based inverted VAT photopolymerization SLA plat-

forms chosen were the Photon-S<sup>TM</sup> (Anycubic Technology Co. Ltd., Kowloon, Hong Kong, China), Form3B<sup>TM</sup> (Formlabs<sup>®</sup> Inc., San Francisco, California), and Phenom<sup>TM</sup> (Peopoly<sup>®</sup>, San Francisco, California). The choice of these platforms allows for the evaluation of multiple printing technologies. The Photon-S<sup>TM</sup> uses LEDs beneath a  $2k$  resolution LCD and the resin bath as its source for UV curing [74]. The Form3B<sup>TM</sup> uses a laser at  $405nm$  wavelength and  $250mW$  power [75]. The Peopoly<sup>TM</sup> uses an “MSLA” (LCD and LED) with a  $72\mu m$  resolution as their printing technology [76].

### 2.7.1 Experimental Methods and Methodology

The purpose of this research is to investigate the performance of multiple 3D printing platforms with different printing technologies for the manufacturing of the unique micro-vertebra geometry or other similar geometries given specified process parameters and standardized pre- and post-print processes. These process parameters and manufacturing processes are enumerated below. In this investigation, the  $6mm$  joint length vertebra with channel diameters of  $0.6$ ,  $0.7$  and  $0.8mm$  was selected as the print test piece as shown in Fig. 2.41.

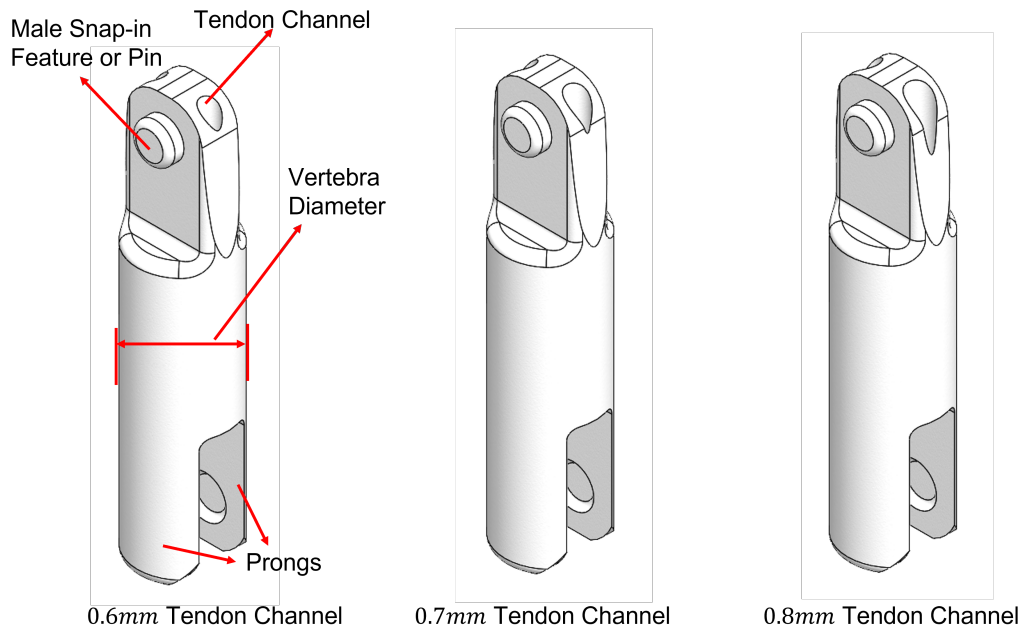


Figure 2.41: Solid Models of the  $6mm$  Joint Length Vertebrae with Different Tendon Channel Diameters

The cross-platform evaluation of some of the process parameters was standardized using a step-by-step repeatable manufacturing process to minimize experimental procedural errors or bias in the results. This process was performed for multiple layer heights, orientations, channel diameters, and resin colors. Chitobox™ (Shenzhen CBD Technology Co., Ltd), a professional 3D printing preprocessing software, is used for preprocessing the models; setting up and labeling each part for identification purposes for a multi-model print of the vertebrae with the defined print orientations and tendon channel diameters in duplicates as shown in Fig. 2.42. In this research, two batches of the vertebrae components are printed with clear and grey resins and evaluated per 3D printing platform. Each print batch contains 36 ( $= 3$  channel diameters  $\times 2$  orientations  $\times 2$  layer heights  $\times 3$  duplicates) vertebrae components.

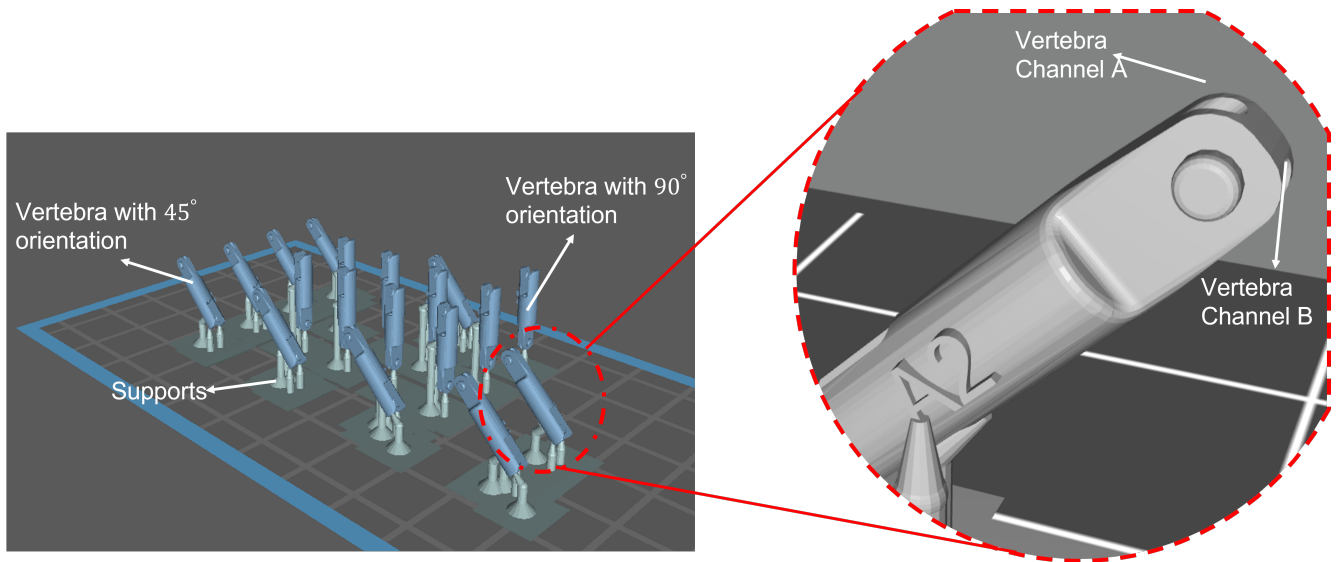


Figure 2.42: Multi-Model Vertebrae Setup in Chitubox™

- Preprocessing and Print Settings

- Orientation: The orientation of parts on the print bed placed at  $45^\circ$  and  $90^\circ$  as shown in Fig. 2.42.
- Support Structures: Support structures were placed in a minimalist approach to avoid interference with key features (such as channels or prongs). Minimal or no support structures were placed on the female snap-in features since these features were found to break easily while removing their support structures during post-processing. Examples of support structures applied are shown in Fig. 2.42.
- Layer Height: Layer height settings were defined at  $0.025mm$  and  $0.050mm$ .
- Printers: The printers were Formlabs Form3B, Anycubic Photon-S, and Peopoly Phenom.



- Print Material: The resin materials used for printing were transparent clear and grey procured from the respective printer manufacturer.
- Other Print Settings: Other print process parameters were left at their manufacturer-recommended default values.
- Resin Material Swap: After a batch of experiments has been completed with the first resin type on one printer, the print bath is cleaned using the manufacturer recommendations before the resin is changed for further experiments.

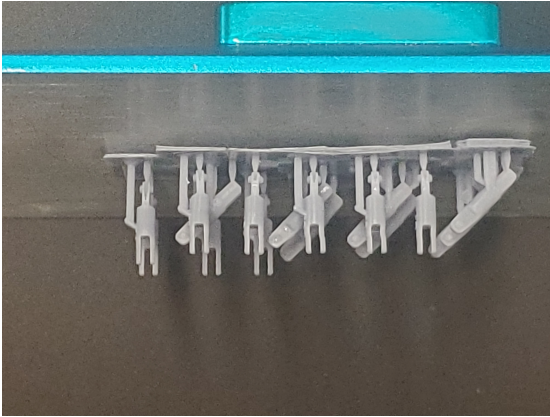
The Formlabs printer allows swapping of the entire printer resin bath (allowing the use of one resin bath per material). For the Peopoly and Anycubic printers, the thermoplastic film sheet of the resin bath was thoroughly cleaned after pouring out the first resin before refilling with the next resin.

- Printing

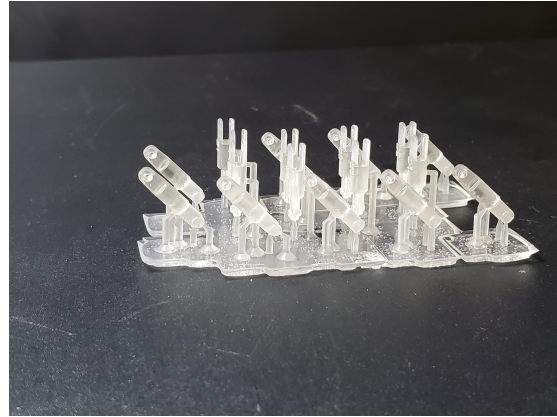
Apart from the aforementioned process parameters defined, the parts were printed using the manufacturer-recommended settings for each printer and resin.

- Part Wash or Cleaning

- Bath Wash: The parts were cleaned immediately after printing in washing machines with Isopropyl Alcohol (IPA) to remove uncured resin using the manufacturer recommended settings for the resin type used. Sample grey and clear resin parts after wash in the Anycubic wash station are shown in Fig. 2.43. The figures show that the print appears to be successful with the raft attached to the print bed and the support holding up the parts.



(a) Sample Manufactured Parts with Grey Resin After Wash Still Attached to Print Bed



(b) Sample Manufactured Parts with Clear Resin After Wash not Attached to Print Bed

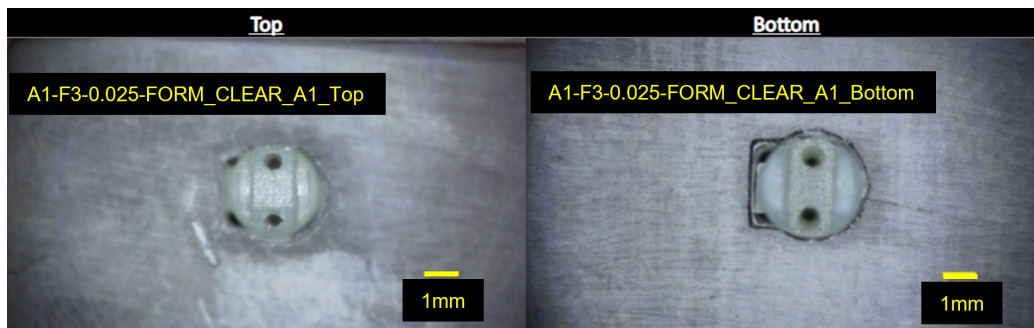
Figure 2.43: Sample Manufactured Parts After Processing in Anycubic Wash Station

- Air Clean: Following the bath wash, each part is air cleaned using 15 psi of air pressure to force clean and remove any remaining residue resin and IPA.
- Manual Wash: An 18-gauge (0.050in or 1.27mm) needle and a 50mL syringe filled with IPA are used to manually wash each part immediately after air cleaning. The needle (attached to the syringe) was placed at 1 – 3cm away from the part and the jet of IPA is directed to each channel and other features to further force clean residue from difficult-to-reach geometries of the vertebra
- Curing
 

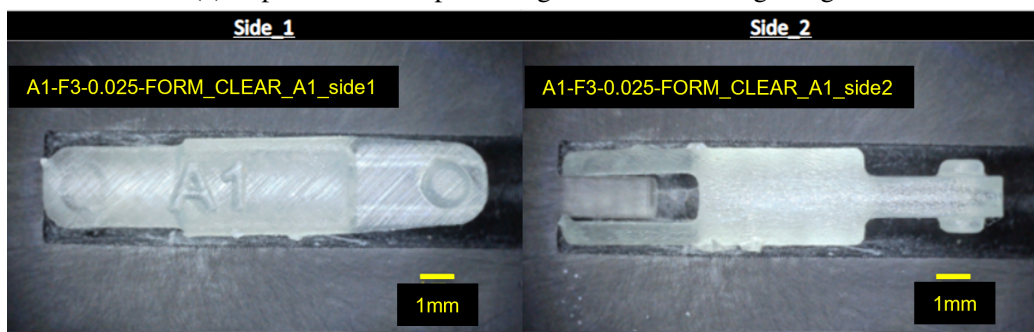
The cleaned parts were then cured using the curing station that accompanies the additive manufacturing platform at their respective default temperature and time settings for the resin material used.
- Imaging and Measurements
 

After curing, the parts were removed from their print support and imaged using a custom-developed holding jig, a Bysameyee<sup>®</sup> microscope (Shenzhen Shengyi Elec-

tronic Commerce Co., Ltd) attached on a stand, and ImageJ imaging software (NIH Bethesda, Maryland, U.S.). Images of individual parts from multiple views were taken in ImageJ. The images were calibrated, processed, and annotated before geometries of interest were measured as shown in Fig. 2.44. The in-built calibration tool in ImageJ uses the relation between a known distance and the pixel count for that distance to set the scale of the image in real-world units. For the purpose of this research, the chosen geometries of interest are the vertebra diameter, and the quality of the prongs, pins, and channels. Except for the vertebra diameter, the other features are evaluated for quality and given a qualitative score of 1 to 3 attributed to poor, good, and excellent quality respectively.



(a) Top View of Sampled Imaged Vertebrae using ImageJ



(b) Side View of Sampled Imaged Vertebrae using ImageJ

Figure 2.44: Sampled Imaged Vertebrae using ImageJ

### 2.7.2 Evaluation of Geometric Responses due to Process Parameters

The printing process parameters, which include the print orientations, the resin color, and the layer height along with the printing platforms were considered as factors contributing to the dimensional or geometric responses of features of the manufactured vertebra. Using the Analysis of Variance (ANOVA) tool in the statistical analysis software, Minitab® (Minitab, LLC, State College, Pennsylvania, U.S.), a manufacturing process model is established for the individual vertebra features of interest as a function of the factors for the purpose of determining the relationship between the manufacturing factors and the vertebra geometric response. The magnitude of the effect of each factor on the geometry stability/instability of the vertebra features without taking the other factors into account is subsequently evaluated. Finally, an evaluation of the effect of the factors and how these factors influence the geometry stability/instability of the vertebra features is performed. Collectively, these analyses can be used to improve the process parameters for geometrically stable, defect-free manufacturing of the vertebra and even predict the quality of the manufactured parts due to modifications before implementation.

### 2.7.3 Results and Discussion

#### **Establishing the Manufacturing Process Model**

A general linear model is used to fit the imaging measurements using regression analysis. The resulting regression equations for estimating the vertebrae geometry responses are shown in Eqs. 2.7-2.11. These relationships can be used to estimate and improve the quality of the interested vertebrae geometry within the experimental range by selecting available factors. Also, the vertebrae are uniquely oriented to allow channels A and B to be printed in a stacked manner or side-by-side to evaluate how these orientations improve the clarity of the channels.

$$\begin{aligned}
\text{Avg. Vertebrae Diameter} = & 2.9586 + 0.1030 \text{Printer}_{(\text{Anycubic})} - 0.0656 \text{Printer}_{(\text{Formlabs})} \\
& - 0.0374 \text{Printer}_{(\text{Peopoly})} - 0.0041 \text{Resin Color}_{(\text{Clear})} \\
& + 0.0041 \text{Resin Color}_{(\text{Gray})} - 0.0171 \text{Orientation}_{(45^\circ)} \\
& + 0.0171 \text{Orientation}_{(90^\circ)} + 0.0113 \text{Layer Height}_{(0.025\text{mm})} \\
& - 0.0113 \text{Layer Height}_{(0.050\text{mm})} - 0.0338 \text{Channel Dia}_{(0.6\text{mm})} \\
& + 0.0054 \text{Channel Dia}_{(0.7\text{mm})} + 0.0285 \text{Channel Dia}_{(0.8\text{mm})}
\end{aligned} \tag{2.7}$$

$$\begin{aligned}
\text{ChA} = & 1.8750 - 0.6250 \text{Printer}_{(\text{Anycubic})} + 0.1528 \text{Printer}_{(\text{Formlabs})} \\
& + 0.4722 \text{Printer}_{(\text{Peopoly})} + 0.2917 \text{Resin Color}_{(\text{Clear})} \\
& - 0.2917 \text{Resin Color}_{(\text{Gray})} + 0.1435 \text{Orientation}_{(45^\circ)} \\
& - 0.1435 \text{Orientation}_{(90^\circ)} - 0.0324 \text{Layer Height}_{(0.025\text{mm})} \\
& + 0.0324 \text{Layer Height}_{(0.050\text{mm})} - 0.1250 \text{Channel Dia}_{(0.6\text{mm})} \\
& - 0.1528 \text{Channel Dia}_{(0.7\text{mm})} + 0.2778 \text{Channel Dia}_{(0.8\text{mm})}
\end{aligned} \tag{2.8}$$

$$\begin{aligned}
\text{ChB} = & 1.7315 - 0.4120 \text{Printer}_{(\text{Anycubic})} + 0.2269 \text{Printer}_{(\text{Formlabs})} \\
& + 0.1852 \text{Printer}_{(\text{Peopoly})} + 0.2593 \text{Resin Color}_{(\text{Clear})} \\
& - 0.2593 \text{Resin Color}_{(\text{Gray})} - 0.1667 \text{Orientation}_{(45^\circ)} \\
& - 0.1667 \text{Orientation}_{(90^\circ)} + 0.0370 \text{Layer Height}_{(0.025\text{mm})} \\
& - 0.0370 \text{Layer Height}_{(0.050\text{mm})} - 0.2037 \text{Channel Dia}_{(0.6\text{mm})} \\
& - 0.1343 \text{Channel Dia}_{(0.7\text{mm})} + 0.3380 \text{Channel Dia}_{(0.8\text{mm})}
\end{aligned} \tag{2.9}$$

$$\begin{aligned}
Prongs = & 2.8843 + 0.0324 Printer_{(Anycubic)} + 0.1157 Printer_{(Formlabs)} \\
& - 0.1481 Printer_{(Peopoly)} - 0.0602 Resin Color_{(Clear)} \\
& + 0.0602 Resin Color_{(Gray)} - 0.0324 Orientation_{(45^\circ)} \\
& - 0.0324 Orientation_{(90^\circ)} - 0.0231 Layer Height_{(0.025mm)} \\
& + 0.0231 Layer Height_{(0.050mm)} - 0.1204 Channel Dia_{(0.6mm)} \\
& + 0.0741 Channel Dia_{(0.7mm)} + 0.0463 Channel Dia_{(0.8mm)} \quad (2.10)
\end{aligned}$$

$$\begin{aligned}
Pins = & 2.4815 + 0.1991 Printer_{(Anycubic)} + 0.0741 Printer_{(Formlabs)} \\
& - 0.2731 Printer_{(Peopoly)} - 0.1111 Resin Color_{(Clear)} \\
& + 0.1111 Resin Color_{(Gray)} + 0.1852 Orientation_{(45^\circ)} \\
& - 0.1852 Orientation_{(90^\circ)} - 0.0463 Layer Height_{(0.025mm)} \\
& + 0.0463 Layer Height_{(0.050mm)} - 0.0787 Channel Dia_{(0.6mm)} \\
& + 0.1296 Channel Dia_{(0.7mm)} - 0.0509 Channel Dia_{(0.8mm)} \quad (2.11)
\end{aligned}$$

The ANOVA tool in Minitab<sup>®</sup> is used to estimate the relationship between the manufacturing factors adopted and the responses of the vertebra features of interest. The “*p*-value“, a statistical test value used to evaluate whether there is a relationship between each factor and the response of the vertebra features of interest, is estimated for each factor. A *p*-value  $\leq \alpha_{Sign}$  suggests that the factor is not statistically significant to the response of the associated vertebra feature, while a *p*-value  $> \alpha_{Sing}$  suggests otherwise [77]. Where  $\alpha_{Sing}$  is the significance level which represents the probability of randomly observing an outlier value and has traditionally been selected as 0.1 or 0.05 or 0.01 [78, 79]. A value  $\alpha_{Sing} = 0.05$

Table 2.9: Table Showing the ANOVA Regression Model Summary

Factors	Analysis of Variance $p$ -value				
	Vertebra Diameter	Vertebra Channel A	Vertebra Channel B	Pin	Prongs
Printer	0.000	0.000	0.000	0.000	0.000
Resin Color	0.788	0.000	0.000	0.000	0.027
Orientation (Deg)	0.261	0.002	0.000	0.000	0.232
Layer Height (mm)	0.456	0.471	0.411	0.136	0.392
Channel Dia (mm)	0.238	0.000	0.000	0.013	0.007
R-Squared	12.07%	46.10%	36.32%	32.85%	14.01%

means that only observations that fall within 95% ( $= 1 - \alpha_{Sign}$ ) of all measurements are accepted.

In this research, lower  $p$ -values are interpreted as evidence for a stronger association between the factor and selected responses. Also, the R-Squared, which estimates the variations of the measurements from the regression is evaluated for the process models. The results of these analyses are presented in Table 2.9 for the vertebra diameter, vertebra male snap-in feature (or pin), tendon channels A and B, and prongs.

The ANOVA shows that the 3D printer used is of greater significance to the vertebra features than the other factors. In terms of the vertebra diameter, a lesser relationship to the factors is observed with the type of resin color used. For the vertebra channels, the pin, and the prongs, a lesser dependence on the factors is observed compared to the layer height settings. At first glance, the R-Squared values for the regression model of all the vertebra features appear low (at  $\leq 50\%$ ) and suggest variability between the factors and responses, however, key conclusions can be drawn for improving the manufacturing experiments since the  $p$ -values suggest there exist statistically significant relationships.

### Effect of the Factors on Vertebra Features

The ANOVA tool in Minitab<sup>®</sup> was used to estimate the effect of each factor on the verte-

bra features. The geometric response means are evaluated for each factor in terms of their dimensional error (as in the case of the vertebra diameter) and manufacturing quality (as in the case of the prongs, pins, and channels) using the measurement data obtained during imaging. The evaluation followed the procedure described in [80] and the results are presented in Figs. 2.45 and 2.46.

In Fig. 2.45a, it is observed that the Anycubic printer offers the lowest dimensional variation of  $\sim 0.06mm$  in the diameter (at manufactured diameter  $\sim 3.06mm$  with as-designed diameter  $3mm$ ) while the largest dimensional variation is associated with the Form3 printer at  $\sim 2.89mm$  with significant negative impact as a result of the clear resin as shown in Fig. 2.46a. This may be attributed to the shrinkage of the resins during polymerization (curing) as a result of the exposure of the resin to a greater power source as is the case with the laser of the Form3 3D printer compared to the lower output power of the LEDs used with the Anycubic or Peopoly [81]. This shrinkage may also be affected by the material composition of the resins used [82, 81]. The effect of the grey color of the resin on the vertebra diameter is less significant but provides better results than the clear resin. When the channel diameter is designed to be larger (from  $0.6mm$  to  $0.8mm$ ), the dimensional variation of the vertebra diameter is observed to be smaller and reduces from  $0.08mm$  to  $0.01mm$ .

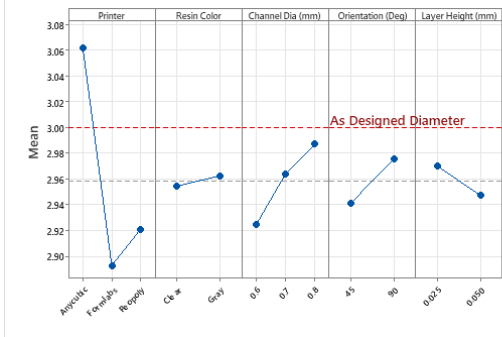
Figs. 2.45b and 2.45c show that the least quality in the manufacturing of the channels is associated with the Anycubic printer while the Formlabs Form3 and Peopoly provide significantly higher quality. The results of the initial manufacturing experiments conducted with the Anycubic 3D printer suggest other factors such as the layer exposure may be a significant factor affecting the quality of the channels even though it was fixed consistently across the 3D printing platforms for uniformity. The clear resin and a larger channel diameter are observed to contribute to a higher quality manufacturing of the tendon channels. In



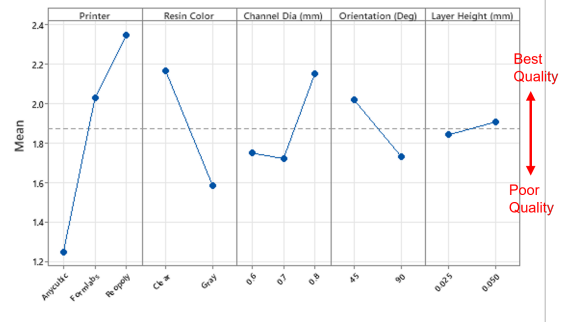
terms of print orientations, channel A is observed to print better at 45° (see Fig. 2.46b) than channel B, while channel B prints better at 90° even though they have the same geometry. This can be explained by the results presented in Fig. 2.46c that show that the quality of channel B is significantly higher at 90° for the Formlabs Form3. Nonetheless, the results suggest that the orientation is significant to the quality of the channels.

Figure. 2.45d shows that the vertebra pins were manufactured at higher quality with the Anycubic and the grey resin color. The pins or male snap-in features are overhanging and show warping from the base of the feature to the end. The observation of warping is less prominent in the Anycubic and the Formlabs for both clear and gray resin as shown in Fig. 2.46d. However, the pins of the gray resin prints on the Anycubic result in much less warping than that of the Formlabs which gave an edge to the overall pin quality from the Anycubic printer. These results suggest a better performance of the 3D printing technology in the Anycubic and the Formlabs to print overhanging features, particularly at the 45° orientation as shown in Fig. 2.46d. Also, the opacity of the resin is known to affect the diffusion of the UV resin during curing and may have played a role in the quality of the pins across the resin colors used [83].

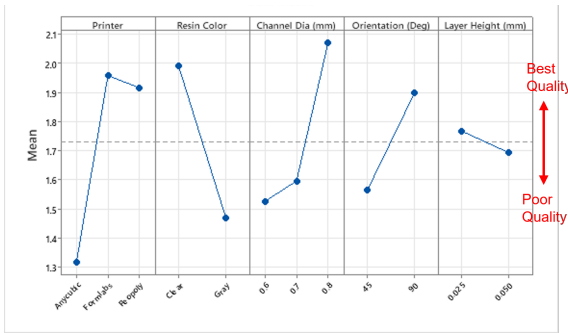
The quality of the prongs shown in Fig. 2.45e is higher in prints from the Formlabs followed by that of the Anycubic particularly when printed in the gray resin. The prongs printed with the Peopoly had significantly lower quality across all parameters as shown in Fig. 2.46e.



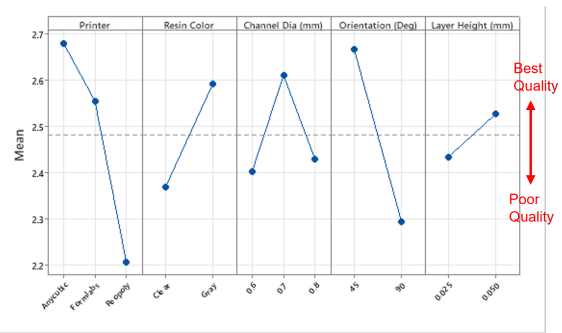
(a) Effect of the Factors on the Vertebra Diameter



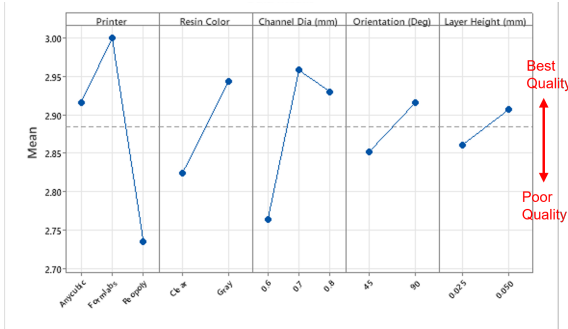
(b) Effect of the Factors on the Tendon Channel A



(c) Effect of the Factors on the Tendon Channel B

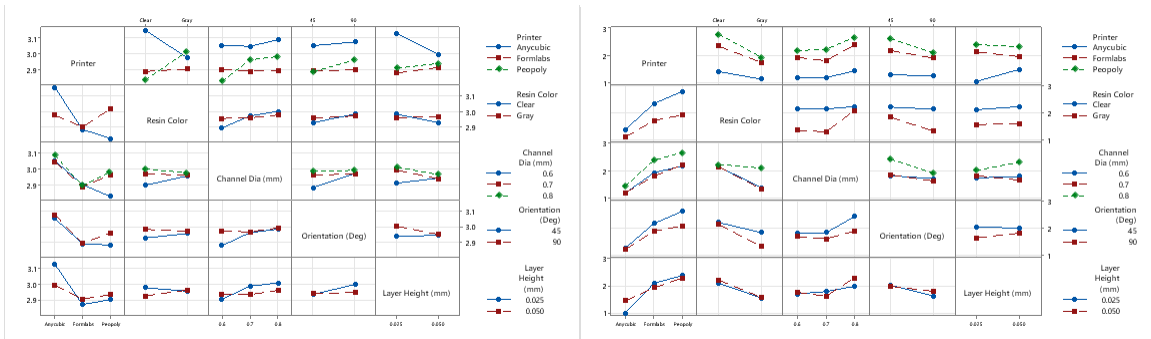


(d) Effect of the Factors on the Male Snap-in Feature or Pin



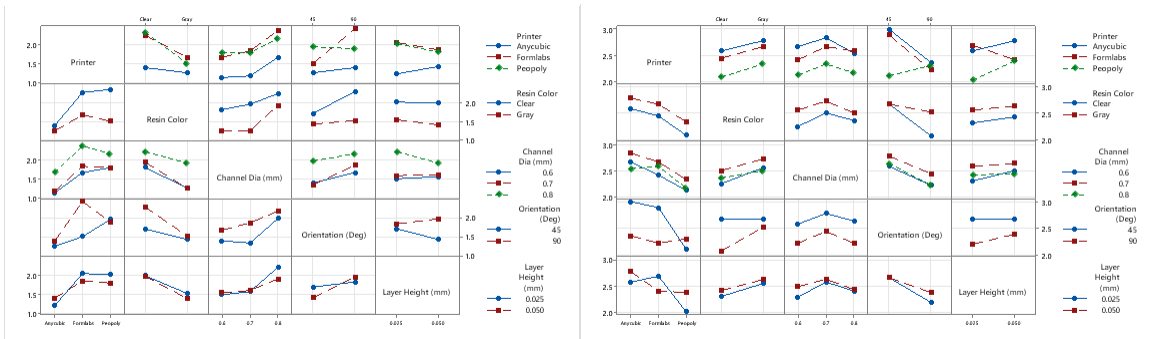
(e) Effect of the Factors on the Prongs

Figure 2.45: Effect of Factors on the Features of Interest



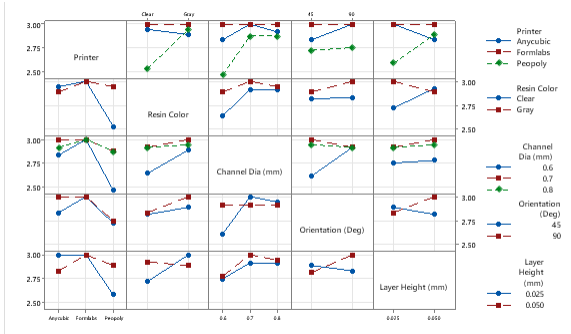
(a) Effect of Multiple Factors on the Vertebra Diameter

(b) Effect of Multiple Factors on the Tendon Channel A



(c) Effect of Multiple Factors on the Tendon Channel B

(d) Effect of Multiple Factors on the Male Snap-in Feature



(e) Effect of Multiple Factors on the Prongs

Figure 2.46: Effect of Multiple Factors on the Various Geometries of Interest

## CHAPTER 3

### MATHEMATICAL MODELING

#### 3.1 Forward Kinematics

The robot kinematic parameters and coordinate frames are defined using the modified Denavit-Hartenberg (MDH) convention according to Craig [84]. A stationary base coordinate frame,  $\{B\}$ , is established at the center of the ellipsoid representing the bladder. Coordinate frames are assigned such that the  $Z$ -axis for each frame aligns with the joint motion axis as shown in Fig. 3.1. The hyper-spherical joint consisting of two roll ( $\theta_{R1}$  and  $\theta_{R2}$ ), a pitch ( $\theta_P$ ), and a yaw ( $\theta_Y$ ), is arranged as shown in Fig. 3.1. The continuum segment is modeled, without loss of generality, as a planar 5-rotational joint elbow manipulator with a uniformly distributed total bend angle,  $\theta$ .

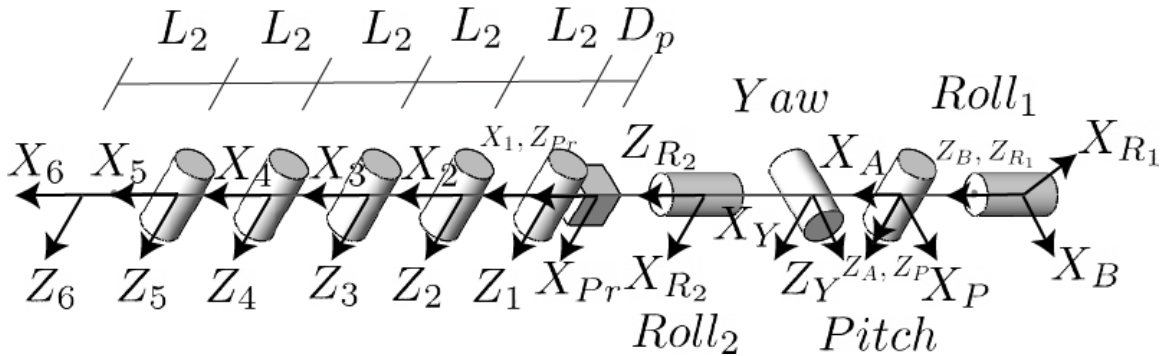


Figure 3.1: Robot Joint Representation and Frames According to the MDH Convention

The application of the forward kinematics equations computes the pose (position and orientation) of the end effector or sensor as a function of the kinematic parameters. The pose of the last coordinate frame 6 (associated with joint 12) with respect to frame 1,  ${}^1_{12}T$ , is

evaluated according to Eq. 3.1, where  ${}^j_{j+1}T$  is the homogeneous transformation matrix of joint frame  $(j + 1)$  reference to joint frame  $(j)$  as described by Craig [84].

$${}^1_{12}T = \prod_{j=1}^{12} {}^j_{j+1}T = \begin{bmatrix} {}^1_{12}R_{3 \times 3} & {}^1_{12}P_{3 \times 1} \\ 0_{1 \times 3} & 1 \end{bmatrix} \quad (3.1)$$

where  ${}^1_{12}R_{3 \times 3} = f(\alpha_j, \theta_j)$  and  ${}^1_{12}P_{3 \times 1} = f(a_j, \alpha_j, d_j, \theta_j)$  are the orientation and position evaluated as functions of the kinematic parameters in Table 3.1.

Table 3.1: Robot kinematic definition using the MDH notation

Frame		Joint		MDH Parameters				Joint Limits*	
C	N	#	Type	$a$	$\alpha(^{\circ})$	$d(mm)$	$\theta(^{\circ})$	Min	Max
$B$	$R_1$	1	$R$	0	0	-41	$\theta_{R_1}$	$-\pi$	$\pi$
$R_1$	$P$	2	$R$	0	90	0	$\theta_P$	$-\pi/2$	$\pi/2$
$P$	$A$	3	-	0	0	0	90	-	-
$A$	$Y$	4	$R$	0	90	0	$\theta_Y + 90$	$-\pi/2$	$\pi/2$
$Y$	$R_2$	5	$R$	0	90	0	$\theta_{R_2}$	$-\pi$	$\pi$
$R_2$	$Pr$	6	$P$	0	0	$D_p$	0	0	130
$Pr$	1	7	$R$	0	-90	0	$\theta_k - 90$	$-\pi/2$	$\pi/2$
1	2	8	$R$	$L_2$	0	0	$\theta_k$	$-\pi/2$	$\pi/2$
2	3	9	$R$	$L_2$	0	0	$\theta_k$	$-\pi/2$	$\pi/2$
3	4	10	$R$	$L_2$	0	0	$\theta_k$	$-\pi/2$	$\pi/2$
4	5	11	$R$	$L_2$	0	0	$\theta_k$	$-\pi/2$	$\pi/2$
5	6	12	-	$L_2$	0	0	0	-	-

where  $\theta_k = \theta/n$  is the angle attained by each module of the  $n$ -modules of the continuum segment of the robot with  $\theta$  being the total angle for all modules of the continuum segment of the robot.

\*Min and Max values are in radians for angles and  $mm$  for distance.

### 3.1.1 Robot Pose and Workspace Visualization

The forward kinematics formulation is used to compute sample robot poses using specified values for the joint parameters. The bladder is modeled as an ellipsoid with nominal dimensions (length, width, height) = (93, 96, 82) $mm$  [26, 54]. The robot bladder workspace

and select robot poses are plotted to aid in visualizing the robot in the bladder as shown in Fig. 3.2. Motion *A* represents the configuration of the robot when all joint parameters are initialized to zero. Motion *B* shows the reach of the robot in the trigone area close to the entrance to the bladder. Motion *C* shows the bending of the continuum segment, pitch rotation, and translation of the prismatic joint which extends the reach of the robot to areas further away from the entrance to the bladder.

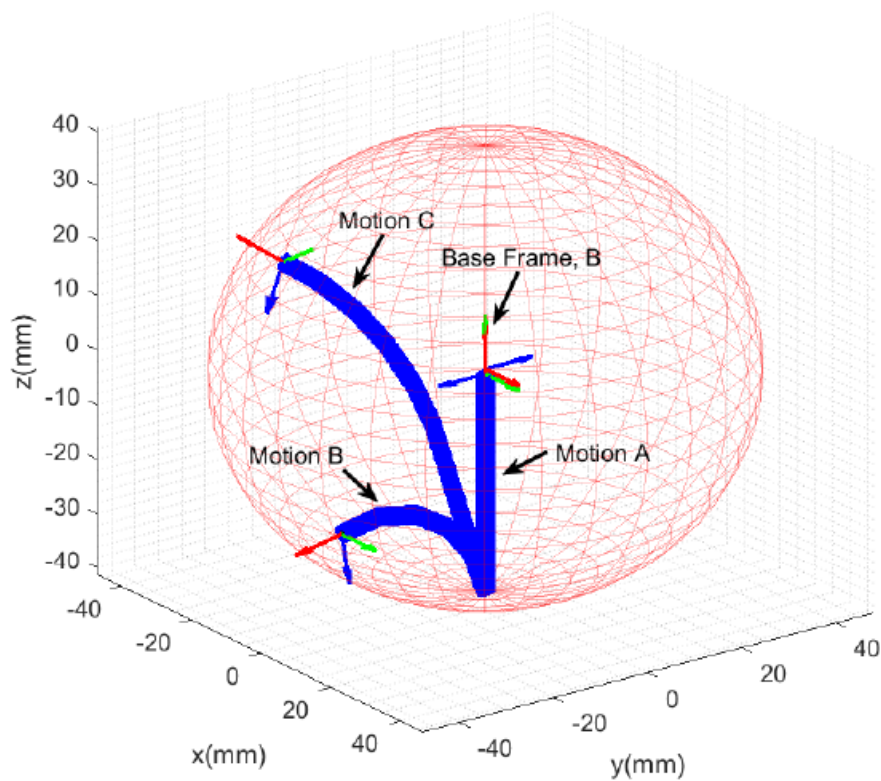


Figure 3.2: Sample Robot Poses in the “Bladder Workspace”; Motion A: All Joint Parameters Initialized to Zero. Motion B: Continuum Segment Bending Angle of  $\theta = 150^\circ$ . Motion C: Continuum Segment bend Angle,  $\theta = 50^\circ$ , Pitch Angle,  $\theta_P = 30^\circ$ , and Prismatic Joint  $D_p = 30\text{mm}$ .

### 3.1.2 Kinematic Pose Error due to Manufacturing Uncertainties

The effectiveness and performance of robotic manipulators are highly dependent on their ability to complete a desired task. This ability can be adversely affected by certain inaccuracy factors that characterize the manipulators as a result of geometrical errors during manufacturing or fabrication and non-geometrical errors that alter the actual positioning and orientation of the manipulator end effector [85, 68]. More specifically, the geometrical errors are a result of inaccurate geometric features of the components of the manipulator, or joint or other assembling errors [85]. While non-geometrical errors are a result of modeling, controls, and compliance errors, or environmental factors (such as temperature or humidity), friction, backlash, or wear of the mechanical elements of the manipulator [85].

The most significant source of robot pose inaccuracy is the geometrical errors in the robot links as a result of manufacturing or machining defects and assembly which introduce variations in the robot dimensions and joint orientations [68]. Considering the dimensional variations of the continuum segment vertebrae due to the additive manufacturing method used and the effect of the manufacturing parameters on the manufactured vertebrae, it is important to study how these dimensional variations contribute to the robot end effector pose error. The study of the relationship between manufacturing variations and the accuracy of the proposed micro-robotic manipulator with an attached force sensor is critical in improving the effectiveness of the robot to palpate the bladder tissue normal to the bladder at the desired location for error-free biomechanical characterization of the bladder tissue.

The kinematic model developed in section 3 is employed to evaluate the proposed robot end effector pose error as the difference between the robot theoretical pose and the differential pose change as a function of the as-designed geometry of interest and their corresponding dimensional variations for the continuum segment [68]. Assuming, there are no error con-

tributing variations outside the continuum segment (the prismatic or hyper-spherical joints), the geometries of interest (shown in Fig. 3.3) are the vertebrae cylindrical length,  $L_v$ , top link joint length,  $l_{J1}$ , and the base link joint length,  $l_{J2}$ . Additional geometrical features such as the tendon channel diameters, the distance between the extension and compression channels, the channel lengths, and the male and female snap-in feature diameters and depths may be considered in a pose error study as geometries of interest. However, a static or dynamic formulation is required as they capture interactions such as backlash, friction, damping, and sliding or mating variations between other bodies in the continuum segment and these additional geometrical features. The geometric uncertainties are used for pose error calculations.

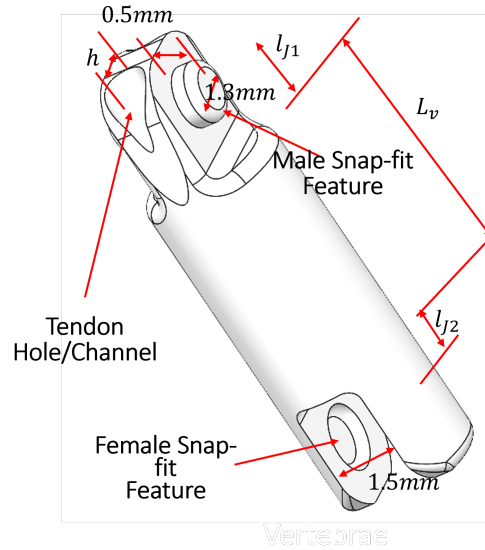


Figure 3.3: Vertebra Showing Geometry of Interest

The real world or actual end effector pose,  ${}^1_{12}T_{actual}$ , of the micro-robotic manipulator is presented in Eq. 3.2 as a function of the robot theoretical pose,  ${}^1_{12}T_{theor}$ , and the differential pose change,  $\Delta^1_{12}T_{theor}$  [68].



$${}^1_{12}T_{actual} = {}^1_{12}T_{theor} \pm \Delta^1_{12}T_{theor} \quad (3.2)$$

The differential pose change,  $\Delta^1_{12}T_{theor}$ , given an arbitrary set of manipulator joint configurations is a function of the geometrical variations,  $\nu = \{L_v, l_{J1}, l_{J2}\}$ , and defined as,

$$\Delta^1_{12}T_{theor} = \sum_i \frac{\delta T_{theor}}{\delta \nu_i} \Delta \nu_i \quad (3.3)$$

An influence matrix,  ${}^1_{12}T_{\nu}^*$  which is a transformation matrix of the manufactured geometry variation of each geometry of interest can be represented as a function of the theoretical robot transformation matrix and is given as  ${}^1_{12}T_{\nu_i}^* = {}^1_{12}T_{theor}^{-1} \frac{\delta T_{theor}}{\delta \nu_i}$  [68]. Therefore, the actual micro-robot end effector pose as a function of the influence matrix is given as,

$${}^1_{12}T_{actual} = {}^1_{12}T_{theor} \left\{ I_4 \pm \sum_i {}^1_{12}T_{\nu_i}^* \Delta \nu_i \right\} \quad (3.4)$$

where  $I_4$  is a  $4 \times 4$  identity matrix.

### Pose Error

The pose error,  $e_{pose}$ , of the manipulator end effector can be obtained as the difference between the actual end effector 3D position and orientation vector as a function of geometric variations or manufacturing uncertainties of interest, and the theoretical end effector position and orientation vectors. The actual end effector position,  ${}^1_{12}\vec{P}_{actual(3 \times 1)}$ , and orientation,  ${}^1_{12}\vec{\zeta}_{actual(3 \times 1)}$  (see section 3.2), vectors are derived from the  ${}^1_{12}T_{actual}$  transformation matrix (Eq. 3.4) by taking the  $3 \times 1$  position vector part as  ${}^1_{12}\vec{P}_{actual(3 \times 1)}$ , and  $3 \times 3$  orientation part and expressing it in  $Z - Y - Z$  Euler convention as  ${}^1_{12}\vec{\zeta}_{actual(3 \times 1)}$ . Similarly, the theoretical position and orientation of the end effector can be expressed as  ${}^1_{12}\vec{P}_{theor(3 \times 1)}$  and  ${}^1_{12}\vec{\zeta}_{theor(3 \times 1)}$  respectively from the theoretical transformation matrix derived in Eq. 3.1. Therefore, the pose error,  $e_{pose}$ , is given as,

$$e_{pose} = \left\| \left\{ \begin{array}{l} {}^1_{12} \vec{P}_{actual(3 \times 1)} \pm {}^1_{12} \vec{P}_{theor(3 \times 1)} \\ {}^1_{12} \vec{\zeta}_{actual(3 \times 1)} \pm {}^1_{12} \vec{\zeta}_{theor(3 \times 1)} \end{array} \right\} \right\| \quad (3.5)$$

### Numerical Evaluation of the Kinematic Pose Error

The kinematic pose error,  $e_{pose}$ , is evaluated using the geometric variations of  $L_v, l_{J1}$  and  $l_{J2}$  due to manufacturing uncertainties for the  $3mm$  joint length vertebrae as discussed in section 2.7 and using Eqs. 3.2-3.5. The  $e_{pose}$  for the proposed manipulator is evaluated using zero joint values for combinations of the variation of the geometry of interest to examine the magnitude of their error contributions to the robot position and orientation. The variations of  $L_v, l_{J1}$  and  $l_{J2}$  are obtained from the procedures described in section 2.7 across the different additive manufacturing technologies used as  $\Delta L_v = |-0.277|mm$ ,  $\Delta l_{J1} = |-0.074|mm$  and  $\Delta l_{J2} = |-0.123|mm$ . The numerical results of this analysis are presented in Table 3.2.

Table 3.2: Continuum Segment Pose Error Due to Manufacturing Geometrical Uncertainties

Geometrical Parameter Uncertainty	Pose Error for Joint Values = 0	
	Position Error (mm)	Orientation Error (°)
$\Delta L_v$	1.385	0.000
$\Delta l_{J1}$	0.370	0.000
$\Delta l_{J2}$	0.615	0.000
$\Delta L_v, \Delta l_{J1}$	1.755	0.000
$\Delta L_v, \Delta l_{J2}$	2.000	0.000
$\Delta l_{J1}, \Delta l_{J2}$	0.985	0.000
$\Delta L_v, \Delta l_{J1}, \Delta l_{J2}$	2.370	0.000

Note: The pose errors estimated above are only due to the five-joint continuum segment without considering the other joints or components of the whole microrobot.

It is observed from Table 3.2 that any variation in a geometric parameter of the continuum segment contributes to the overall error in positioning the end effector but has no effect on orienting the end effector. Likewise, a higher variation in any of the geometric parameters of interest has a greater effect on the positioning. Also, a greater adverse effect on the positioning is observed when multiple geometric parameters of interest have variations.

In a situation where there is uncertainty in the bending of the continuum segment of the proposed robotic manipulator due to geometric variation of the continuum segment vertebrae, the pose error formulation in Eq. 3.5 may also be applied to estimate the pose error. For example, if the overall bend angle,  $\theta$  of the continuum segment has an uncertainty,  $\Delta\theta$ , the differential pose change,  $\Delta_{12}^1 T_{theor}$ , and the actual robot end effector pose,  ${}_{12}^1 T_{actual}$  in Eqs. 3.3 and 3.4 respectively can be reformulated to estimate the contributions from  $\Delta\theta$ . The result of this analysis is shown in Table 3.3 for an assumed high precision bend accuracy of  $\Delta\theta = 0.0014^\circ$  and increased to  $\Delta\theta = 0.002^\circ$  and the geometrical parameter uncertainty,  $[\Delta L_v, \Delta l_{J1}, \Delta l_{J2}] = 0$  [86]. The results in Table 3.3 indicate that uncertainty in the continuum segment bending contributes to errors in both the positioning and orientation of the end effector which is not the case with uncertainty due to geometric uncertainty. Furthermore, when the uncertainty in the continuum segment bend is increased, the effect on the pose of the end effector becomes larger as shown by the greater magnitude of position and orientation error for an increase in  $\Delta\theta$ .

Table 3.3: Continuum Segment Pose Error Due to Uncertainties in Joint  $\theta$

Joint Parameter Uncertainty	Pose Error for Joint Values = 0	
	Position Error (mm)	Orientation Error ( $^\circ$ )
$\Delta\theta = 0.0014^\circ$	$58.64 \times 10^{-6}$	0.0014
$\Delta\theta = 0.0020^\circ$	$83.78 \times 10^{-6}$	0.0020

If all uncertainties in the geometries and joint parameters of the entire robot manipulator are considered, the contributions to the pose error can be evaluated using the same aforementioned approach for the tolerances (which includes the geometrical variations),  $\nu = [L_v, l_{J1}, l_{J2}, \theta_{R1}, \theta_P, \theta_Y, \theta_{R1}, D_p, \theta] = [0.277mm, 0.074mm, 0.123mm, 0.002^\circ, 0.002^\circ, 0.002^\circ, 0.002^\circ, 0.0762mm, 0.002^\circ]$ , assuming high precision joint displacements and reasonable values for tolerances [86, 87]. The pose error is estimated as  $e_{pose} = [2.446mm, 0.008^\circ]^T$ . It is recommended that the pose error should be included in the analysis of the bladder tissue palpation data obtained by the sensor.

## 3.2 Inverse Kinematics

### 3.2.1 Mathematical Modeling Approach

The inverse kinematics (IK) formulation uses a differential kinematics approach that couples the joint velocities to the end effector linear,  $\vec{0}_n V$ , and angular,  $\vec{0}_n \omega$ , velocities through the translational,  $J_V$ , and angular,  $J_\omega$ , components of the Jacobian [88]. The differential kinematics approach is preferred for this work, since it helps to avoid singularities especially with the robot hyper-redundancy and to provide appropriate continuous joint solutions without the need to select from multiple possible solutions usually obtained with other approaches [89].

The desired end effector Cartesian position is the point of interest on the interior bladder wall. The desired robot end effector or attached uniaxial sensor tip orientation is defined by a frame  $NYZ$  and is desired to be at normal contact with the bladder wall during palpation for localized force measurements. Since the bladder is modeled as an ellipsoid, this orientation is not fixed but is established from the orthogonal basis of a normal vector,  $\vec{N} = N_1 \hat{i} + N_2 \hat{j} + N_3 \hat{k}$ , on the bladder surface at the point of interest. The  $Y$ -axis of frame  $NYZ$  is evaluated using null space analysis such that  $\vec{N} \cdot \vec{Y} = 0$  and the  $Z$ -axis

of  $NYZ$  is evaluated by  $\vec{Z} = \vec{N} \times \vec{Y}$ . Therefore, during palpation, the robot end effector frame with axes  $(X_6, Y_6, Z_6)$  must align with the computed desired orientation frame  $NYZ$ .

The  $Z(\alpha) - Y(\beta) - Z(\gamma)$  Euler angle convention is used to obtain an equivalent orientation vector,  ${}^0_n \vec{\zeta}(q)$ , describing the orientation  ${}^1_{12}R_{3 \times 3}$  in Eq. 3.1 as presented in Eq. 3.6.

[84]

$${}^0_n \vec{\zeta} = \begin{bmatrix} \alpha \\ \beta \\ \gamma \end{bmatrix} = \begin{bmatrix} \text{atan2}(R_{23}/\sin\beta, R_{13}/\sin\beta) \\ \text{atan2}\left(\sqrt{R_{31}^2 + R_{32}^2}, R_{33}\right) \\ \text{atan2}(R_{32}/\sin\beta, -R_{31}/\sin\beta) \end{bmatrix} \quad (3.6)$$

In order to avoid singularities in the equivalent orientation vector, the inverse kinematics formulation considers distinct cases of Eq. 3.6 depending on the value of  $\beta$  [84]. For example, if  $\sin\beta \neq 0^\circ$ , then Eq. 3.6 is used. Otherwise, if  $\sin\beta = 0$  (i.e.  $\beta = 0^\circ$  or  $\beta = 180^\circ$ ) in Eq. 3.6, the following cases are considered.

If  $\beta = 0^\circ (\sin\beta = 0) \Rightarrow$

$${}^0_n \vec{\zeta} = \begin{bmatrix} \alpha \\ \beta \\ \gamma \end{bmatrix} = \begin{bmatrix} 0^\circ \\ 0^\circ \\ \arctan2(-R_{12}, R_{11}) \end{bmatrix} \quad (3.7)$$

If  $\beta = 180^\circ (\sin\beta = 0) \Rightarrow$

$${}^0_n \vec{\zeta} = \begin{bmatrix} \alpha \\ \beta \\ \gamma \end{bmatrix} = \begin{bmatrix} 0^\circ \\ 180^\circ \\ \arctan2(R_{12}, -R_{11}) \end{bmatrix} \quad (3.8)$$

The elements of the skew-symmetric matrix of  ${}^0_n \vec{\omega}$ , derived from

$S({}^0_n \vec{\omega}) = {}^0_n \dot{R}(\alpha, \beta, \gamma) {}^0_n R(\alpha, \beta, \gamma)^T$ , are presented in Eq. 3.9a. This is further ex-

panded to develop the relationship between  ${}^0_n\vec{\omega}$  and  ${}^0_n\vec{\zeta}$  as a function of the Euler angles  $(\alpha, \beta, \gamma)$ .

$${}^0_n\vec{\omega} = \begin{bmatrix} \dot{\gamma}\cos\alpha\sin\beta - \dot{\beta}\sin\alpha \\ \dot{\gamma}\sin\alpha\sin\beta + \dot{\beta}\cos\alpha \\ \dot{\gamma}\cos\beta + \dot{\alpha} \end{bmatrix} \quad (3.9a)$$

$$= \begin{bmatrix} 0 & -\sin\alpha & \cos\alpha\sin\beta \\ 0 & \cos\alpha & \sin\alpha\sin\beta \\ 1 & 0 & \cos\beta \end{bmatrix} \begin{bmatrix} \dot{\alpha} \\ \dot{\beta} \\ \dot{\gamma} \end{bmatrix} = A \left( {}^0_n\vec{\zeta} \right) {}^0_n\dot{\zeta} \quad (3.9b)$$

where  $A \left( {}^0_n\vec{\zeta} \right)$  is a nonlinear matrix.

The inverse orientation differential kinematics is then evaluated according to Eq. 3.10.

$${}^0_n\dot{\zeta} = A \left( {}^0_n\vec{\zeta} \right)^{-1} {}^0_n\vec{\omega} = A \left( {}^0_n\vec{\zeta} \right)^{-1} J_\omega \dot{q} \quad (3.10)$$

The inverse kinematics formulation to evaluate the joint values for a specified or desired end effector pose (position  $P$  and orientation  $\zeta$ ) is derived using the translational (or commonly referred to as linear) and orientation velocities and their corresponding Jacobians according to Eq. 3.11.

$$\dot{\vec{x}}_A = \begin{bmatrix} {}^0_n\dot{P} \\ {}^0_n\dot{\zeta} \end{bmatrix} = \begin{bmatrix} J_V \\ A \left( {}^0_n\vec{\zeta} \right)^{-1} \cdot J_\omega \end{bmatrix} \dot{q} = J_A(q) \dot{q} \quad (3.11)$$

where  $\dot{\vec{x}}_A$  and  $J_A(q)$  are the analytically evaluated solutions for the robot pose and the Jacobian respectively. The discrete form of Eq. 3.11 along with a reduced form is shown in Eq. 3.12.

$$\frac{\overrightarrow{\Delta x_A}}{\Delta t} = J_A(q) \frac{\overrightarrow{\Delta q}}{\Delta t} \Rightarrow \overrightarrow{\Delta x_A} = J_A(q) \overrightarrow{\Delta q} \quad (3.12)$$

The change in the robot joint parameters,  $\overrightarrow{\Delta q}$ , as a function of changes in the robot pose,  $\overrightarrow{\Delta x_A}$ , from the current to the desired pose is evaluated according to Eq. 3.13. The joint parameters are updated through an iterative process according to Eq. 3.14 while considering the defined joint limits.

$$\begin{aligned} \overrightarrow{\Delta q} &= J_A^{-1}(q) \overrightarrow{\Delta x_A} = J^{\dagger ED} \overrightarrow{\Delta x_A} \\ &= J_A(q)^T (J_A(q) J_A^T(q) + \eta I_{n \times n})^{-1} \overrightarrow{\Delta x_A} \end{aligned} \quad (3.13)$$

$$\overrightarrow{q}_{Next} = \overrightarrow{q}_{Current} + \overrightarrow{\Delta q} \quad (3.14)$$

where  $J^{\dagger ED}$  is a damped pseudo-inverse Jacobian employed to avoid possible solution discontinuities or singularities and  $\eta$  is a damping factor evaluated according to Eq. 3.15 [90].

$$\eta = \frac{1}{2} \begin{bmatrix} \overrightarrow{\Delta \vec{P}} \\ \overrightarrow{\Delta \vec{\zeta}} \end{bmatrix}^T \cdot \begin{bmatrix} \overrightarrow{\Delta \vec{P}} \\ \overrightarrow{\Delta \vec{\zeta}} \end{bmatrix} \quad (3.15)$$

where  $\overrightarrow{\Delta \vec{P}}$  and  $\overrightarrow{\Delta \vec{\zeta}}$  are the end effector position and orientation iterative updates as a solution is computed.

The inverse kinematics (IK) formulation is implemented in MATLAB<sup>®</sup> using the definitions of the robot kinematic structure and joint limits in Table 3.1. The algorithm inputs are the robot kinematic configuration, bladder ellipsoidal geometry definition, the initial robot pose, and the desired contact location on the bladder wall which is used to compute the desired end effector orientation constraint within a user defined tolerance. Subsequently,

the joint parameters are evaluated using Eqs. (3.13-3.15) while satisfying a user defined tolerance vector,  $\varepsilon_d (= [|\varepsilon_P|, |\varepsilon_\zeta|])$ , for position and orientation respectively. The model solution error,  $E_m$ , is computed at each iteration according to Eq. 3.16. The IK algorithm evaluates the joint parameters until the evaluated robot pose is within the user-defined tolerance, such that  $E_m \leq \varepsilon_d$ .

$$E_m = [ |E_p|, |E_\zeta| ]^T = [ \| \vec{P}_d - \vec{P}_a \|, \| \vec{\zeta}_d - \vec{\zeta}_a \| ]^T \quad (3.16)$$

where subscripts  $d$  and  $a$  are the desired and actual (calculated) values for the spatial position,  $\vec{P}$ , and orientation,  $\vec{\zeta}$ .

### 3.2.2 Performance of IK Formulation

The performance of the IK formulation is evaluated by computing the joint parameters for a number of arbitrarily selected or desired contact locations on the ellipsoid surface while enforcing the normal palpation orientation constraint. For each test case, the evaluated robot configuration in the bladder workspace is plotted for visualization purposes as shown in Fig. 3.4. The iterative joint solutions for motions A, B, C, and D are shown in Fig. 3.5. The initial, desired and evaluated poses, evaluated joint parameters, model solution error, and number of iterations to reach the defined tolerance level are presented in Table 3.4. The model solution errors for all test cases were within the user-defined tolerance of  $\varepsilon_d = [1mm, 4^\circ]$ .

The performance of the inverse kinematic formulation used and that of the hyper-redundant joint to reach all areas of the bladder wall with the desired pose (within user defined error) without discontinuities or singularities even when joint limits are reached is presented in Fig. 3.5. As observed in Fig. 3.5, motion discontinuities are avoided as there are no sudden changes in any of the joint parameter iterative solution sets.



Table 3.4: Summary of Results for Arbitrary Robot End Effector Pose on the Ellipsoid

Motion	Initial Pose, $x_I$		Desired Pose, $x_D$		Evaluated Pose, $x_E$		Computed Joint Parameters $\vec{q} = [D_P, \theta_{R1}, \theta_P, \theta_Y, \theta_{R2}, \theta]^T$	Model Solution Error, $E_m$		Number of Iterations
	$\vec{P}^*$	$\vec{\zeta}^{**}$	$\vec{P}^*$	$\vec{\zeta}^{**}$	$\vec{P}^*$	$\vec{\zeta}^{**}$		$E_P(mm)$	$E_\zeta(deg)$	
A	0.00	0.00	9.49	-0.20	9.41	0.04	[40.69, 45.74, -3.68, 1.16, -142.12, -11.22] <sup>T</sup>	0.99	3.14	11129
	0.00	-1.57	2.08	1.39	2.04	-1.32				
	9.10	-3.14	40.01	-0.17	39.02	1.42				
B	0.00	0.00	-8.47	1.89	-8.36	2.07	[38.30, 51.15, -13.47, -16.38, 61.03, -5.61] <sup>T</sup>	0.94	3.85	927
	0.00	-1.57	26.92	-1.02	26.52	-1.21				
	9.10	-3.14	33.09	-0.76	32.24	3.08				
C	0.00	0.00	39.52	0.20	39.53	-0.18	[32.71, 2.19, -33.00, 8.21, 5.62, -1.29] <sup>T</sup>	0.96	3.34	1534
	0.00	-1.57	-8.67	0.58	-8.34	-0.99				
	9.10	-3.14	20.45	0.06	19.55	-2.86				
D	0.00	0.00	-13.71	2.11	-13.83	1.44	[-0.54, 25.83, 35.58, 17.63, -6.44, -153.08] <sup>T</sup>	0.35	0.83	8
	0.00	-1.57	24.51	1.01	24.80	0.58				
	9.10	-3.14	-33.09	0.61	-32.93	0.85				
E	0.00	0.00	14.34	1.25	14.11	-1.19	[19.36, 155.06, 40.15, -38.05, 160.33, -5.96] <sup>T</sup>	0.88	3.79	751
	0.00	-1.57	-45.54	-0.12	-44.78	-0.67				
	9.10	-3.14	-4.28	-0.09	-4.65	-2.93				

\*  $\vec{P}(P_x, P_y, P_z)$  is in  $mm$ , \*\*  $\vec{\zeta}(\alpha, \beta, \gamma)$  is in  $deg$ , and \*\*\*  $\vec{q}$  is in  $[mm, deg, deg, deg, deg, deg]^T$ .

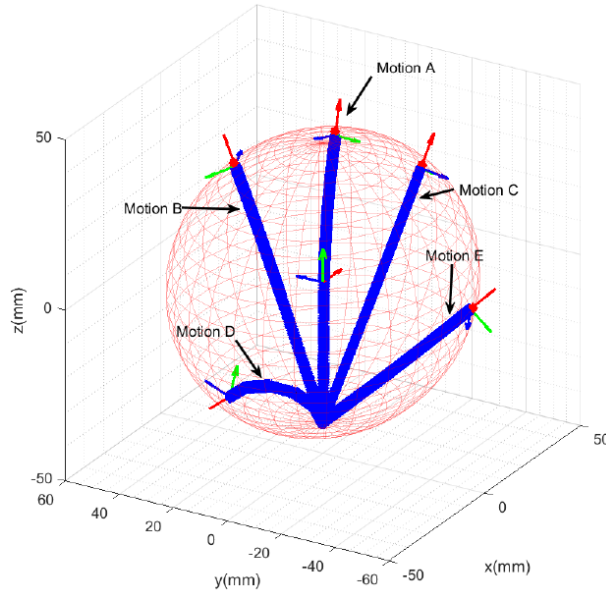
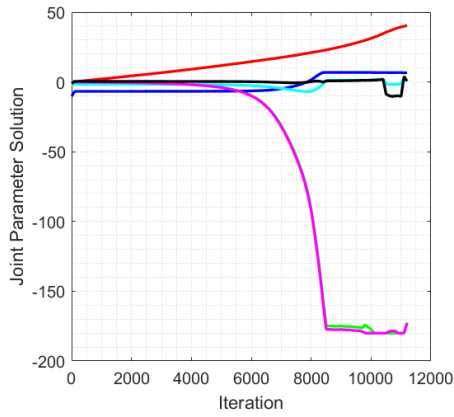
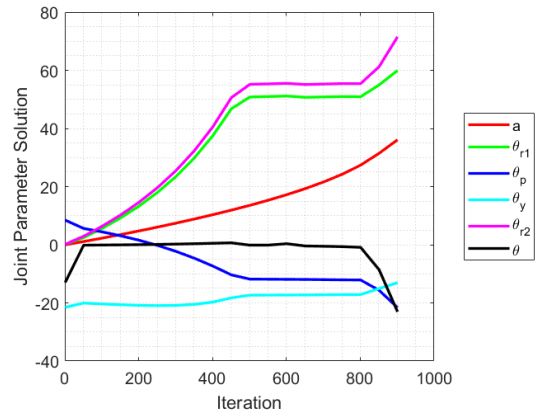


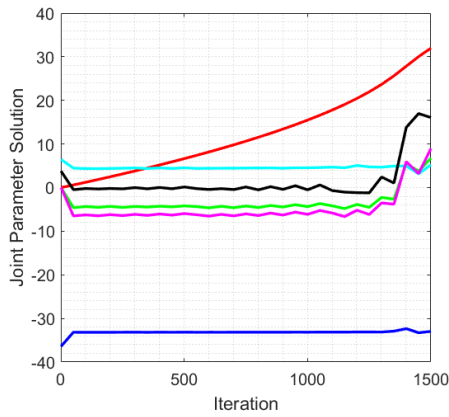
Figure 3.4: Robot Inverse Kinematics Evaluated Poses for Arbitrarily Selected Bladder Contact Locations. Note: Axes have same length for visualization purposes.



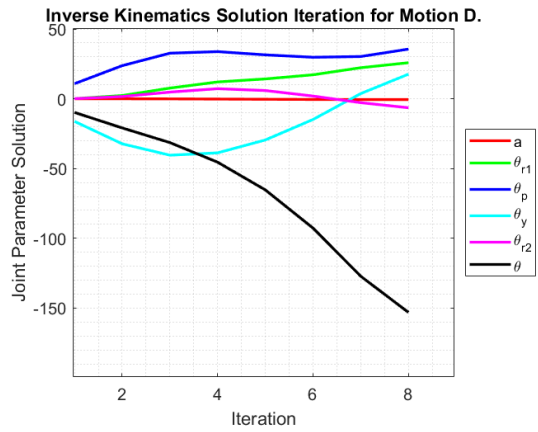
(a) Motion A



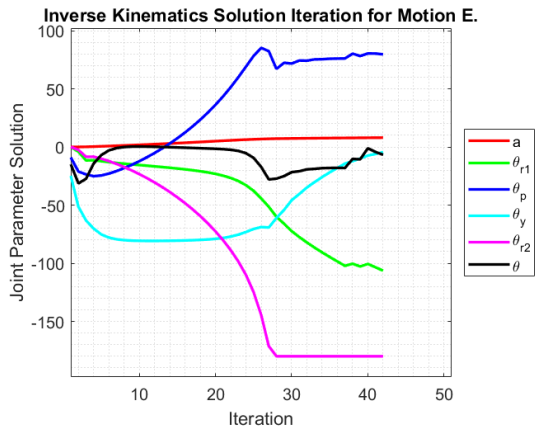
(b) Motion B



(c) Motion C



(d) Motion D



(e) Motion E

Figure 3.5: Inverse Kinematics Iterative Solution Set for Selected Poses.

### 3.2.3 Singularity and Manipulability

In addition to the motion studies of the proposed robotic manipulator, the singularity and manipulability measures are critical considerations in the design stage and control. These measures provide a quantitative determination of the ability of the robotic manipulator to position and orient the end effector [91, 92, 93]. As such, the singularity and manipulability measures are investigated using the kinematic formulation.

#### 3.2.3.1 Singularity

Evaluating the manipulator singularities aid in determining which manipulator configurations are unreachable, which end effector velocities produce infinite joint velocities, or which joint torques produce infinite end effector forces and torques [88]. In this research, the ability of the robotic manipulator to position and orient a force sensor end effector in the bladder for tissue palpation is of importance. As such, a focus on investigating the manipulator singularities for motion accessibility is pursued.

The singularities of a manipulator are evaluated from the Jacobian matrix,  $J_A(q)$ , mapping the joint velocities,  $\vec{\dot{q}}$ , to the end effector velocities,  $\vec{\dot{x}}_A$ , as a function of the joint parameters,  $\vec{q}$  [88]. The values of the joint parameters determine the maximum number of the independent columns (or rank) of  $J_A(q)$  for which the manipulator can meet any arbitrary end effector velocity. For a robotic manipulator such as the proposed one with a spherical joint, the rank of  $J_A(q)$  will always be  $\leq 6$  [88]. However, when the Jacobian loses full rank, the determinant of  $J_A(q) = 0$ , and the manipulator is said to be at a singularity point [84]. Therefore, the singularity is analyzed for the extreme motions (A-E) (Fig. 3.4) identified in section 3.2.2 and presented in Fig 3.6.

### 3.2.3.2 Manipulability

First introduced by Yoshikawa, the manipulability measure quantitatively describes the functionality of the robotic manipulator end effector to attain “best” poses in the workspace as a function of the joint configurations [91]. In this approach, how close the robot is to a singular configuration is characterized using “manipulability ellipsoids” to express the possible directions in which the end effector moves with the least or most effort [94, 95]. Consequently, manipulability is useful for determining the optimal design architecture and size of a robotic manipulator or the optimal configuration to complete a desired task [95]. Hence, it is recommended that the manipulability measure be used as an additional constraint in the proposed inverse kinematics algorithm to compute joint configuration cases for maximum manipulability of the end effector.

Yoshikawa established the manipulability measure,  $w$ , for a redundant manipulator based on the Jacobian matrix where the matrix column number,  $m >$  row number,  $n$  as [91]

$$w = \sqrt{\det(J(q)J^T(q))} \quad (3.17)$$

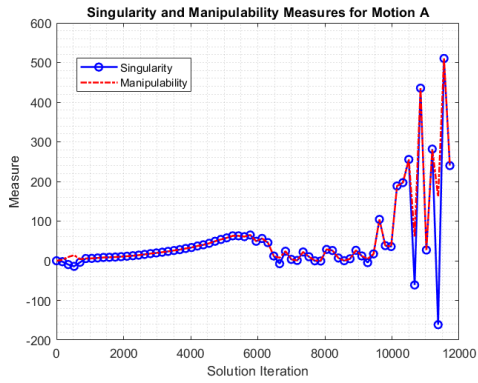
The column number,  $m$ , represents the number of joints, and the row number,  $n$ , is the number of DoF in cartesian space. In the case of a non-redundant manipulator, the number of columns is equal to the number of rows in the Jacobian ( $m = n$ ), the manipulability measure,  $w$ , reduces to the absolute value of the singularity measure and is given as [91]

$$w = |\det J(q)| \quad (3.18)$$

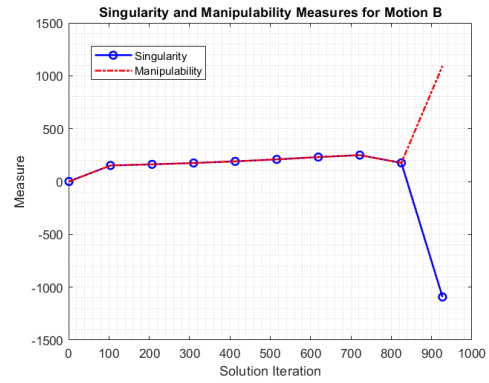
The proposed micro-robotic manipulator has 10 joints, with 4 joints dedicated to hyper-spherical motion, one prismatic motion, and a 5-joint continuum segment. The forward and inverse kinematic model developed and evaluated considers a single joint parameter,  $\theta$ , as the overall bend angle of the five joints of the continuum segment. Therefore, reducing the possible 10 joint configuration to a 6 joint configuration. Hence, the Jacobian matrix has  $m = n$  and produces manipulability measures for Motions A-E as presented in Fig. 3.6.

### **Discussion on Singularity and Manipulability**

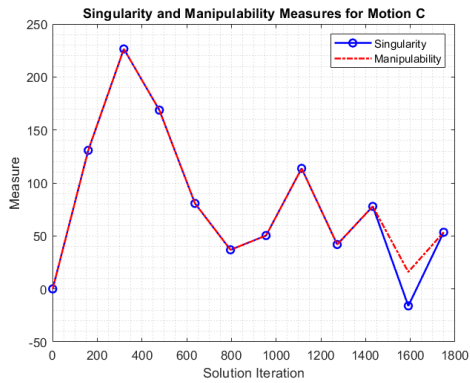
The desired locations for which singularity and manipulability measures are computed are on the bladder surface (the workspace boundary of the robot). Figures. 3.6a to 3.6e indicate Motions A through E have singularity and manipulability measures that are non-zero. These computed measures are relatively large and only suggest that there exists some degree of capability for kinematic changes in the end effector position and orientation at the computed motion joint configurations. This leads to the conclusion that the entire robot manipulator joint configuration design is a feasible design. In this research, emphasis has been placed on the continuum segment (the critical part that goes into the patient), however further development of the hyper-spherical joint is equally important to optimize the robot palpation ability of the bladder interior wall.



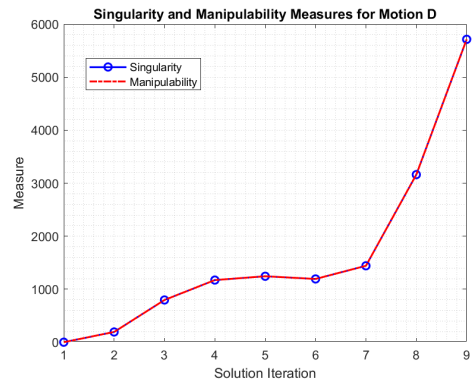
(a) Singularity and Manipulability Measures for Motion A



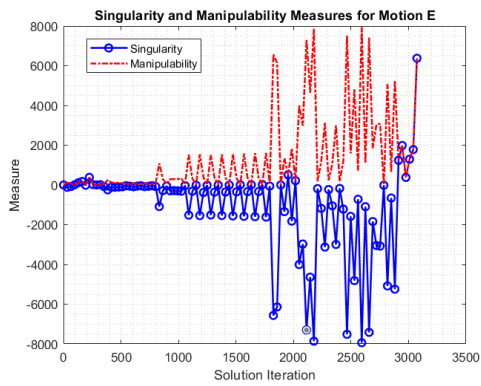
(b) Singularity and Manipulability Measures for Motion B



(c) Singularity and Manipulability Measures for Motion C



(d) Singularity and Manipulability Measures for Motion D



(e) Singularity and Manipulability Measures for Motion E

Figure 3.6: Singularity and Manipulability Measures for Motions Evaluated in Section 3.2.2

### 3.3 Quasi-Static Formulation of Continuum Segment

As described in section 2.3.3, the joint tube is a critical component of the operation of the robot continuum segment. The continuum segment is modeled as a series of vertebrae inside elastic tubes driven by flexion/extension tendons. The rotation of each single module joint depends on the bending behavior or the reaction stresses generated by the corresponding tube when the tendons are actuated. These stresses could be advantageously employed to control the joint rotation by computing the tendon or actuating force for a single module or joint considering the material properties and geometry of the elastic joint tube, the geometric parameters of the module joint, and the actuating force component. Hence, characterizing the tube and module joint interactions is important to establish the continuum segment behavior. The analysis begins by establishing a joint compliance model for each vertebra before analyzing the performance of the joint and evaluating the required applied tension force as a function of the desired bending angle.

#### 3.3.1 Joint Compliance Modeling

The elastic deformation of the encompassing tube at each continuum segment joint due to flexion and extension forces is modeled assuming the tube to be an incompressible Neo-Hookean hyperelastic material with strain energy function,  $W = (\mu/2)(I_1 - 3)$ , where  $\mu$  is the tube shear modulus, and  $I_1 (= \lambda_1^2 + \lambda_2^2 + \lambda_3^2)$  is the first invariant of the Cauchy-Green deformation tensor with  $\lambda_1, \lambda_2$ , and  $\lambda_3$  being the axial, circumferential and radial principal stretch ratios respectively [96, 97]. The principal component stresses along these directions are evaluated according to Eq. 3.19 where  $P/\lambda_\kappa$  is an augmented term with  $P$  being the Lagrange multiplier [98].

$$\sigma_\kappa = \left( \frac{\delta W}{\delta \lambda_\kappa} - \frac{P}{\lambda_\kappa} \right), \kappa = 1, 2, 3 \quad (3.19)$$

It is assumed that the tube is incompressible and maintains a uniform curvature during bending, which according to Rivlin *et al.* yields  $\lambda_1 \cdot \lambda_2 \cdot \lambda_3 = 1$ ,  $\lambda_1 = \lambda$ ,  $\lambda_2 = 1$  and  $\lambda_1 \cdot \lambda_2 \cdot \lambda_3 = \lambda \cdot \lambda_3 = 1$  [99]. These conditions imply constant joint tube volume before and after deformation. The strain energy function can then be expressed as  $W = (\mu/2)(\lambda^2 + 1^2 + 1/\lambda^2 - 3)$  yielding  $\delta W/\delta \lambda = (\mu\lambda, \mu, \mu/\lambda)$ . The axial, circumferential and radial stresses,  $\sigma_1$ ,  $\sigma_2$  and  $\sigma_3$  respectively, are then evaluated according to Eq. 3.19. Noting that  $\sigma_3 = 0$ , the Lagrange multiplier becomes  $P = \mu/\lambda^2$  which yields  $\sigma_1 = \mu(\lambda - 1/\lambda^3)$  and  $\sigma_2 = \mu(1 - 1/\lambda^2)$ . Since  $\sigma_3 = 0$  and  $\sigma_2 \ll \sigma_1$ , then  $\sigma_1$  becomes the dominant principal stress.

The presented joint compliance model is applied to an elastic tube of wall thickness,  $t$ , and length,  $L$ , undergoing a bending deformation of angle,  $\theta$ , as shown in Fig. 3.7. The distance between the point where the strain element is defined to the outer circumference of the circular section is  $c'$ , while  $c$  is the distance between that point and the interior circumference.  $r_c$  is the radius of the tube interior wall, and  $R$  is the radius of curvature of the tube under bending. The angular position of the strain element on the tube cross-section is defined as  $\phi$ . The stretch ratio,  $\lambda$ , is evaluated as the ratio of the deformed tube radius and the original radius according to Eq. 3.20 [98].



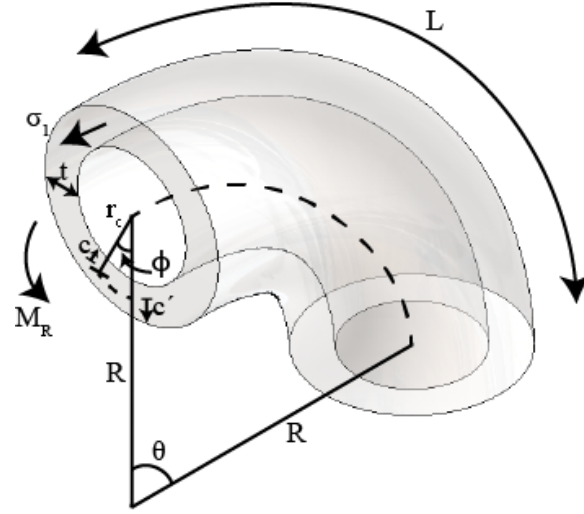


Figure 3.7: Flexible Tube Circular Cross Section.

$$\lambda = \frac{R + c'}{R} \text{ with } c' = (t + r_c) - (c + r_c)\cos\phi \quad (3.20)$$

The incremental force acting on the joint tube strain element is the product of the principal stress and the tube element cross sectional area,  $\sigma_1 dA$ . Integrating the incremental force in the circumferential and radial directions of the cross section yields the bending moment,  $M_R$ , due to the stresses experienced by the tube as presented in Eq. 3.21.

$$M_R = 2 \int_A \sigma_1 (r_c + t) c' L dA \quad (3.21a)$$

$$M_R = 2 \int_0^\pi \sigma_1 \left\{ \int_0^t ((r_c + t)(r_c + c) - (r_c + c)^2 \cos\phi) L d\phi \right\} dc \quad (3.21b)$$

The schematic of a single robot module with two vertebrae and a tube covering the joint is shown in Fig. 3.8a. The module behavior can be evaluated using the force and moment

balance for the joint tube for Vertebra 1 and Vertebra 2. The analysis for Vertebra 1 and Vertebra 2 yields Eqs. 3.22 and Eqs. 3.23 respectively.

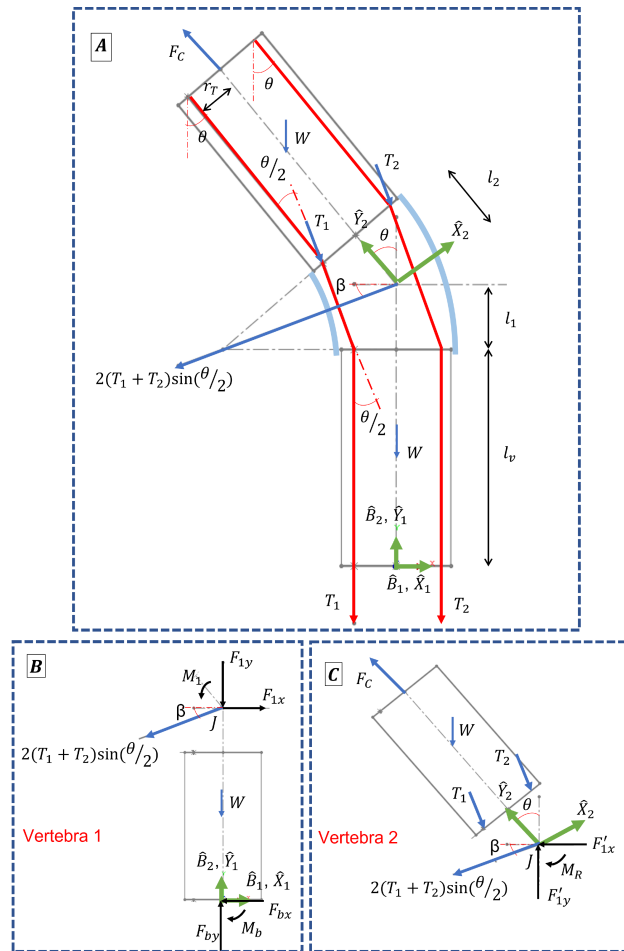


Figure 3.8: A. Schematic for a Single Module with Flexible Tube over the Joint, B. Free Body Diagram of Vertebra 1, and C. Free Body Diagram of Vertebra 2.

$$-F_{bx} + F_{1x} - 2T_{12}\sin\left(\frac{\theta}{2}\right)\cos(\beta) = 0 \quad (3.22a)$$

$$F_{by} - F_{1y} - 2T_{12}\sin\left(\frac{\theta}{2}\right)\sin(\beta) - W = 0 \quad (3.22b)$$

$$-M_b + \overrightarrow{P_{BW}} \times (-W)\hat{B}_2 + \overrightarrow{P_{BJ}} \times \left\{ \left[ F_{1x} - 2T_{12}\sin\left(\frac{\theta}{2}\right)\cos(\beta) \right] \hat{B}_1 \right. \quad (3.22c)$$

$$\left. + \left[ -F_{1y} - 2T_{12}\sin\left(\frac{\theta}{2}\right)\sin(\beta) \right] \hat{B}_2 \right\} + M_1 = 0 \quad (3.22d)$$

$$-F'_{1x} - 2T_{12}\sin\left(\frac{\theta}{2}\right)\cos(\beta) + T_{12}\sin(\theta) - F_C\sin(\theta) = 0 \quad (3.23a)$$

$$F'_{1y} - 2T_{12}\sin\left(\frac{\theta}{2}\right)\sin(\beta) - W - T_{12}\cos(\theta) + F_C\cos(\theta) = 0 \quad (3.23b)$$

$$\begin{aligned} & -M_R + \overrightarrow{P_{JW}} \times (-W)\hat{B}_2 + \overrightarrow{P_{JFC}} \times \left( -F_C\sin(\theta)\hat{B}_1 + F_C\cos(\theta)\hat{B}_2 \right) \\ & + \left( \overrightarrow{P_{JT_1}} + \overrightarrow{P_{JT_2}} \right) \times \left( T_1\sin(\theta)\hat{B}_1 - T_2\cos(\theta)\hat{B}_2 \right) = 0 \end{aligned} \quad (3.23c)$$

where,  $\overrightarrow{P_{BW}}$ ,  $\overrightarrow{P_{BJ}}$ ,  $\overrightarrow{P_{JW}}$ ,  $\overrightarrow{P_{JFC}}$ ,  $\overrightarrow{P_{JT_1}}$  and  $\overrightarrow{P_{JT_2}}$  are kinematic vectors as shown in Fig. 3.8.

$T_1$  and  $T_2$  are the applied tensions with  $T_{12} = T_1 + T_2$ ,  $W$  is the weight of the rotating vertebra,  $l_v$  is the length of the vertebra, and  $l_1$  and  $l_2$  are the vertebrae link lengths, and  $M_R$  is the reaction moment due to tube bending.

### 3.3.2 Joint Compliance Numerical Analysis

The effects of the joint length ( $L = l_1 + l_2$ ) and the elastic tube material properties on the behavior of the continuum segment as a function of applied tension are evaluated using Eqs. (3.21-3.23). Specifically, the tension-bend angle relationship is investigated for the following nominal model parameters; vertebra weight  $W = 0.30mN(29mg)$ , joint length

$L = l_1 + l_2 = 1.50 + 1.50 = 3.00mm$ , vertebra length  $l_v = 5mm$ , tube inner diameter  $d = 3.00mm$ , tube outer diameter  $D = 4.00mm$ , tube shear modulus  $\mu = 0.91Nmm^{-2}$ , and a bend angle range  $\theta = (0 \text{ to } 36^\circ)$ . The distance between the tendon attachment point and the central axis of the continuum segment is  $r_T = 1.00mm$ .

The effects of joint length on the tension-bend angle relationship are presented in Fig. 3.9 for joint lengths  $L = (3, 6, 9, \text{ and } 12)mm$  with all other parameters assigned their nominal values.

The effect of the vertebra weight,  $W_B$ , on the tension-bend angle responses for a single module with joint lengths  $L = (3, 6, 9, \text{ and } 12)mm$  was also evaluated. The weight effect depends on the robot configuration relative to the gravity field. Comparing the tension responses for  $W_B = 0N$  with that of  $W_B \neq 0N$  when the weight “assisted” the tension (or in a positive gravity field as shown in Fig. 3.8), the percentage difference was found to be 0.02 to 0.03% of the tension. When the weight was “opposing” the tension, the tension percentage difference between  $W_B \neq 0N$  and  $W_B = 0N$  was found to be 0.01 to 0.02% for the three lengths. Since the weight contribution to the tension is in the order of 0.03%, the vertebra weight was not considered in any further analysis and the presented results.

Three shear moduli in the range of values for silicone rubber were considered,  $\mu = (0.45, 0.91 \text{ and } 1.82)Nmm^{-2}$  [100]. The relative bend angle behavior as a function of applied tension for these moduli with all other model parameters assigned their nominal values is shown in Fig. 3.10.

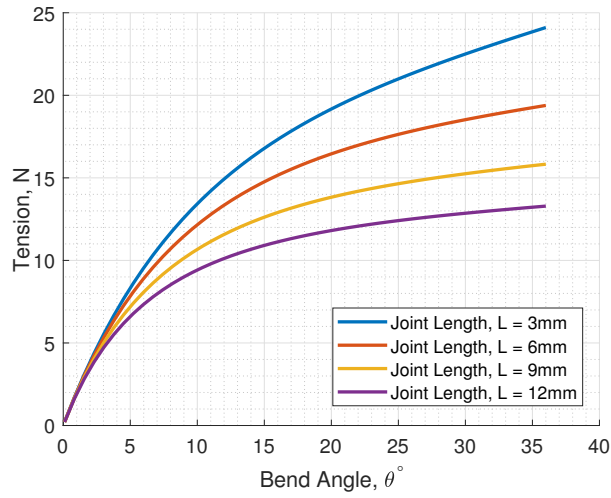


Figure 3.9: Single Module Tube Applied Tension as a Function of Bend Angle for Different Joint Lengths  $L = (3, 6, 9, 12)mm$  with all other Parameters Assigned their Nominal Values.

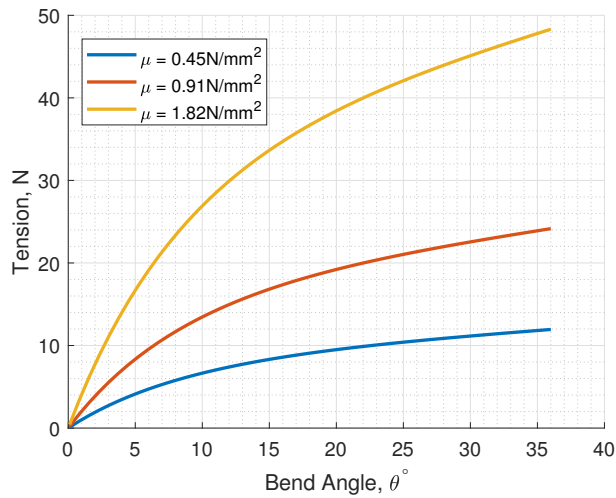


Figure 3.10: Single Module Tube Applied Tension as a Function of Bend Angle for Different Shear Moduli  $\mu = (0.45, 0.91, 1.82) Nmm^{-2}$  with all other Parameters Assigned their Nominal Values.

The single module results presented in Figs. 3.9 and 3.10 are further analyzed by evaluating closed-form expressions for the required tension as a function of the bend angle for each case. Two-term exponential functions were considered using data points at  $5^\circ$  increments. The evaluated expressions for the required tension are presented in Table 3.5. The tension magnitudes at  $5^\circ$  intervals are also compared across trends to evaluate the expected response. The tension-bend angle curve fit equations could prove useful when characterizing the joint compliance of the single module for multiple joint geometry and material properties.

Table 3.5: Two-Term Exponential Function Parameters for Tension-bend Angle Relationships based on theoretical analysis.

Continuum Configuration Parameter	General Model: $T(\theta) = ae^{b\theta} + ce^{d\theta}$				
	Parameter Value	Model Results*			
		a	b	c	d
Joint Length ( $mm$ ) ( $\mu = 0.91Nmm^{-2}$ )	3	17.00	0.10	-17.00	-11.00
	6	16.00	0.10	-16.00	-13.00
	9	13.00	0.10	-13.00	-15.00
	12	11.00	0.10	-11.00	-17.00
Shear Modulus ( $Nmm^{-2}$ ) ( $L = 3mm$ )	0.45	8.60	0.10	-8.60	-11.00
	0.91	17.00	0.10	-17.00	-11.00
	1.82	35.00	0.10	-35.00	-11.00

The model parameters are assigned their nominal values and units as appropriate (see Table 2.2)

\*The model regression coefficient for each parameter value presented is  $R^2 = 1$

The nonlinear behavior of the joint results presented in Fig. 3.9 shows that for the same tube cross section and material properties increasing the joint length leads to a nonlinear decrease in the tension required to achieve the same bend angle. The response sensitivity of the tension as a function of the bend angle decreases both as the bend angle increases as well as when the joint length is increased. However, the response sensitivity exhibits an increasing nonlinear behavior as the tube shear modulus increases. This is expected as

increasing the elastic tube shear modulus produces a stiffer joint and decreases the joint compliance as shown in Fig. 3.10. Likewise, it is observed that the response sensitivity is greater at the smaller bend angles for both joint lengths or shear moduli. The module nonlinear behavior and compliance could be attributed to the ratio of the active tube length to the tube radius and/or the radius to tube thickness as described in [101, 102].

#### 3.4 Principle of Virtual Work: Multi-Module Continuum Segment Model

In section 3.3, a quasi-static model was developed using a series of force-moment equations to evaluate the relationship between the applied tendon tension and the resulting bend angle for one continuum segment module (consisting of one joint) as a function of the joint elastic tube material and geometric properties and the joint geometries. As a reminder, the continuum segment is modeled as a series of vertebrae with each joint encompassed inside an elastic tube and driven by flexion/extension tendons. The rotation of a single module joint depends on the bending behavior or the reaction stresses generated by the corresponding tube when the tendons are actuated. The tube reaction is captured by establishing a joint compliance model due to the tube at the joint. However, the consideration of “non-active” forces and moments such as reaction forces and moments requires constraint factors to solve for more unknown variables than available equations. For instance, in the single module quasi-static model, six force and moment equations with additional constraints were used to solve for eight unknowns of which the required tension for a desired bend angle was the only unknown of interest. This modeling approach will increase in complexity should multiple continuum segment modules be evaluated.

An approach such as the principle of virtual work can be applied where reactions and internal forces are not needed in the formulation of a reduced number of equilibrium equations for a multi-body system such as the continuum segment [103]. Likewise, it is not

necessary to use free body diagrams of the multi-body system to formulate a relationship between forces and moments [103]. As a result of the reduced complexity and other benefits of the principle of virtual work, one can introduce imaginary tension components to each continuum segment module in order to establish the unique behavior of each joint of a multi-module segment in relation to the applied tension running through the entire length of the continuum segment.

Consider a mechanical system with external forces  $F_1, F_2, \dots, F_n$  acting at points  $p_1, p_2, \dots, p_n$  on the system causing virtual displacements  $q_1, q_2, \dots, q_n$  which must agree with the system kinematic constraints [104]. According to the principle of virtual work, the “given mechanical system will be in equilibrium if, and only if, the total virtual work  $W$  of all the external forces vanishes” as expressed in generalized form in Eq. 3.24 [104].

$$\delta W = F_1 \delta q_1 + F_2 \delta q_2 + \dots + F_n \delta q_n = 0 \quad (3.24)$$

### 3.4.1 Ideal Virtual Work Formulation

The schematic of a given multi-module continuum segment of the proposed robotic manipulator with  $n$  number of vertebrae or  $n - 1$  joints along with joint tubes is shown in Fig. 3.11; where  $i = 0 : 1 : n$  is the number of vertebrae,  $W_i$  is the weight of each vertebra,  $\theta_i$  is the angular displacement of each module joint due to an applied tension,  $T_i$ , and  $T_i = T$  is the imaginary tension acting on each joint, with  $\hat{x}_i$  and  $\hat{y}_i$  being the coordinate axes of the base or body attached frames. The module behavior can be evaluated using the principle of virtual work,  $\delta W = 0$ , (see Eq. 3.24) as a result of the end effector contact force,  $F_C$ , perpendicular to the  $n$ th vertebra (considered to be the attached microforce sensor), and moments,  $M_{T_i}$ ,  $M_{W_i}$ , and  $M_{R_i}$  acting on the continuum segment during small virtual displacements,  $\delta\theta_i$ ,  $\delta x_i$  and  $\delta y_i$ . The analysis for the relation between the applied tension,



$T$ , and the individual joint bend angle,  $\theta_i$ , assuming  $F_C$  to be zero can be evaluated using Eq. 3.25. The series of work done,  $\delta W_i$ , equations in Eq. 3.25 can be solved as a system of simultaneous equations.

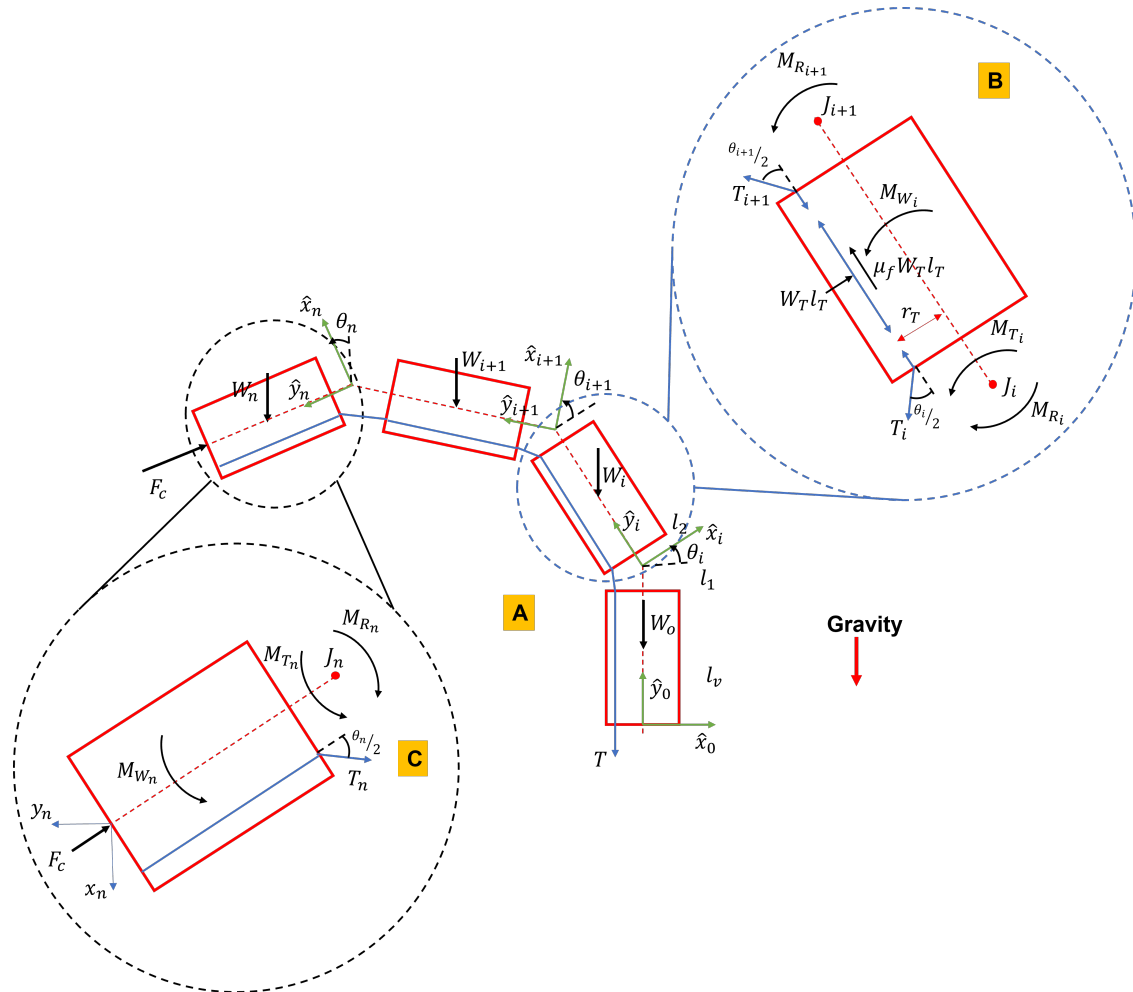


Figure 3.11: A. Schematic for n-Modules with Flexible Tube over the Joint, B.  $i^{th}$  Vertebra Showing Friction, Force and Moment Interactions, and C.  $n^{th}$  Vertebra Showing Force and Moment Interactions.

$$\delta W_i = \begin{cases} (M_{T_i} - M_{R_i} + M_{W_i} + M_{R_{i+1}}) \delta \theta_i = 0 & \text{if } i < n \\ (M_{T_i} - M_{R_i} + M_{W_i}) \delta \theta_i = 0 & \text{if } i = n \end{cases} \quad (3.25)$$

where,

$$M_{T_i} = \vec{P}_{J_i T_i} \times \vec{T}_i$$

$$M_{W_i} = \vec{P}_{J_i W_i} \times \vec{W}_i$$

and

$$\vec{P}_{J_i T_i} = -r_T \hat{x}_i + l_2 \hat{y}_i$$

$$\vec{P}_{J_i W_i} = \left( l_2 + \frac{l_v}{2} \right) \hat{y}_i$$

$$\vec{W}_i = -W_i \hat{y}_0$$

$$\vec{T}_i = -T_i \sin \left( \frac{\theta_i}{2} \right) \hat{x}_i - T_i \cos \left( \frac{\theta_i}{2} \right) \hat{y}_i$$

where  $l_v$  is the vertebra cylindrical length,  $l_1$  and  $l_2$  are the vertebra link lengths, and  $r_T$  is the distance between the vertebra central axis to the point of action of the tendon. The reaction moment due to each joint tube bending,  $M_{R_i}$ , is obtained as described in section 3.3.1 and it is a function of the joint bend angle  $\theta_i$ , the joint geometry, and the  $i^{th}$  tube material properties.

#### 3.4.2 Virtual Work Formulation Considering Frictional Cases

The virtual work formulation presented in Eq. 3.25 assumes the total tension applied to the tendon is entirely used to actuate the n-module continuum segment. Therefore, no frictional energy loss is experienced. However, energy loss should be expected due to friction

from the relative motion between the tendon and the vertebrae channel during actuation. Likewise, frictional losses are also expected at each module joint when the male snap-in feature in interference fit, rotates on the surface of the supporting female snap-in feature as a result of the opposition to the angular displacement of the rotating vertebrae. The tendon-channel and joint friction cases are derived in the following sections and incorporated in Eq. 3.25.

### 3.4.2.1 Tendon-Channel Friction

When tension is applied to the tendon to actuate the continuum segment, the tendon slides through the vertebrae channel as a result of forming the continuum segment curvature. The relative motion between the tendon and the channel generates friction which acts to oppose the applied tension and leads to energy loss. However, friction is nonexistent on the  $n$ th vertebra because the tendon is tethered at one end of the vertebra and experiences no relative motion. The schematic of this motion-friction interaction is presented in Fig. 3.12. Where the normal,  $N$ , is the weight per length of the tendon,  $W_T$ , over the tendon length,  $L_T$ . Assuming no lubrication, the friction model of the interaction can be derived as Eq. 3.26 to establish a relation between the input tension,  $T_i$ , and the output tension,  $T_{i+1}$ , as shown in Fig. 3.12.

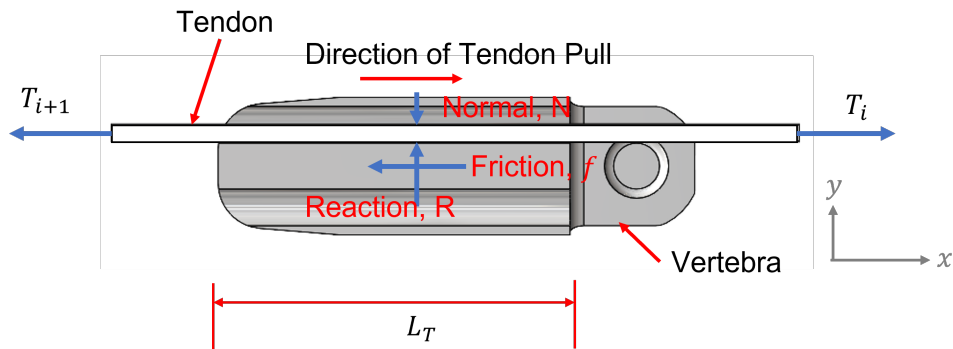


Figure 3.12: Schematic of the Tendon-Channel Friction Interaction for the  $i^{th}$  Vertebra

$$\begin{aligned}
\sum F_x &= T_i - f - T_{i+1} = 0, \\
\sum F_y &= R - N = 0, \\
\therefore T_{i+1} &= T_i - \mu_f W_T L_T
\end{aligned} \tag{3.26}$$

Where  $f = \mu_f N$  and  $N = W_T L_T$ , with  $\mu_f$  being the coefficient of static friction between the Nylon tendon and resin plastic channel surface.

### 3.4.2.2 Joint Friction

As shown in Fig. 3.13a, the female snap-in feature in the prongs of the  $i^{th}$  vertebra is supported on the male snap-in feature. As such, during actuation, the rotating  $ith$  vertebra needs to overcome a bearing friction as a result of the surface interaction between the male and female snap-in features. This interaction is exaggerated in Fig. 3.13b to show a point of contact between the two surfaces. Fig. 3.13b also shows the total weight of the ensuing vertebrae,  $F_{Load_i}$ , propagated from the force sensor through the joints to the base of the vertebrae. While at the point of contact, the normal,  $F_{N_i}$ , frictional,  $F_{f_i}$  and reaction forces,  $R_i$ , exist.  $F_{f_i}$  is tangential to the surface of the male snap-in feature at the point of contact and acts to oppose the rotation of the  $ith$  vertebra while  $F_{N_i}$  is perpendicular to  $F_{f_i}$  at that point.  $\alpha_i$  is the resultant angle between  $F_{N_i}$  and  $R_i$ . Assuming no lubrication, the moment due to friction at each joint,  $M_{f_i}$ , about the center of the joint that opposes any positive moment due to applied tendon tension is statistically derived as shown in Eq. 3.27

$$\begin{aligned}
\sum F_y &: -F_{Load_i} + R_i = 0, \\
\sum M &: M_{f_i} = r_{f_i} \hat{Y}_i \times F_{f_i} \hat{X}_i, \\
\therefore M_{f_i} &= -F_{Load_i} r_{f_i} \sin(\alpha_i) \cos^2(\theta_i) - F_{Load_i} r_{f_i} \sin(\alpha_i) \sin^2(\theta_i)
\end{aligned} \tag{3.27}$$

Where  $\mu_R$  is the coefficient of static friction between the two resin surfaces and  $\alpha_i = \tan^{-1}(\mu_R)$  and  $\sin(\alpha_i) = F_{f_i}/R_i$ .

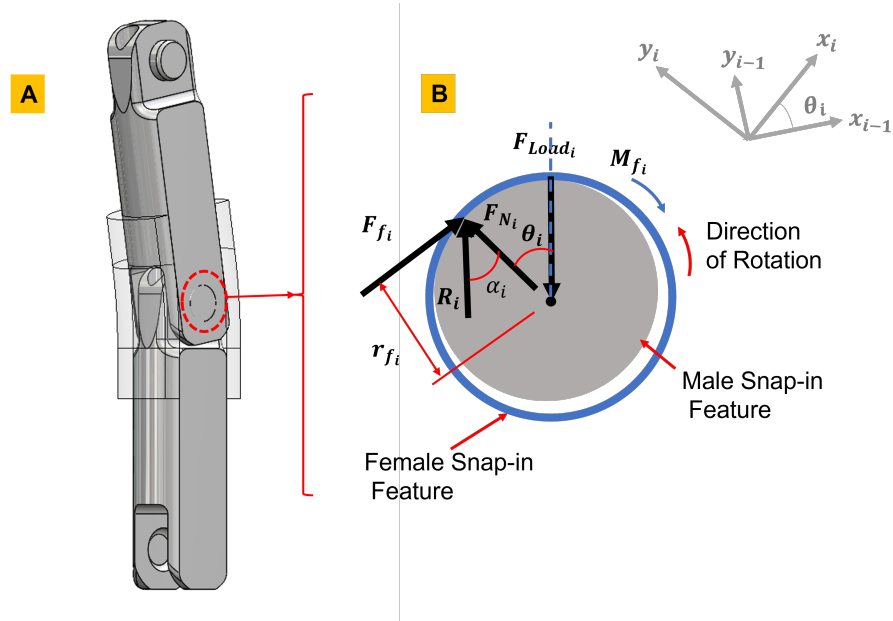


Figure 3.13: Schematic Showing Joint Friction. A. Section view of a Single Continuum Module Showing Male and Female Snap-in Interference, B. Free Body Diagram of the Resulting Force and Moment.

### 3.4.3 Evaluation of Virtual Work Formulation

The bend angle behavior of the n-module continuum segment can be evaluated for any given applied tension values assuming the material properties of the joint elastic tubes and the geometric parameters of the vertebrae and tubes are known by reformulating Eq. 3.25 as Eq. 3.28 using Eqs. 3.26 and 3.27. For an ideal bend angle behavior, Eq. 3.28 is used while assuming no friction, therefore  $\mu_f = 0$  and  $\mu_R = 0$ .

$$\delta W_i = \begin{cases} (M_{T_i} - M_{R_i} + M_{W_i} + M_{R_{i+1}} - M_{f_i})\delta\theta_i = 0 & \text{if } i < n \\ (M_{T_i} - M_{R_i} + M_{W_i} - M_{f_i})\delta\theta_i = 0 & \text{if } i = n \end{cases} \quad (3.28)$$

The performance of the model is evaluated for a number of cases where certain model parameters are varied and their effect on the bend angle-tension response is studied. MATLAB<sup>®</sup> was utilized in this process and the results of these studies are also plotted in Fig. 3.14 with the shear modulus material property chosen as  $\mu = 0.91Nmm^{-2}$  unless otherwise stated.

CASE 1: The principle of virtual work model is compared to the quasi-static model for a single module with 3, 6 and 9mm joint lengths (assuming the point of action of the tendon is at the base of the distal vertebra) and without frictional consideration ( $\mu_f = \mu_R = 0$ ).

CASE 2: The principle of virtual work model is evaluated for a single module with 6mm joint length and for an ideal situation ( $\mu_f = \mu_R = 0$ ), only joint friction ( $\mu_f = 0, \mu_R = 0.25$ ), only tendon friction ( $\mu_f = 0.25, \mu_R = 0$ ), and all friction ( $\mu_f = 0.25, \mu_R = 0.25$ ).

CASE 3: The principle of virtual work model is evaluated for a single module with 3, 6 and 9mm joint lengths and with frictional consideration ( $\mu_f = 0.25, \mu_R = 0.25$ ).

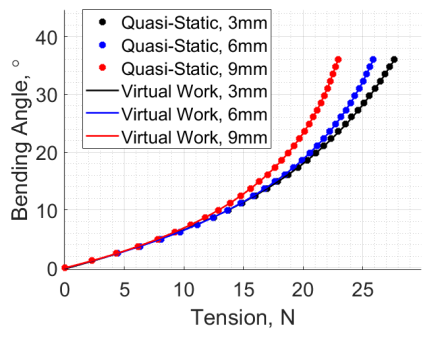
CASE 4: The principle of virtual work model is evaluated for n-module where  $n = [1, 2, 3]$  with 3mm joint length and without frictional consideration ( $\mu_f = \mu_R = 0$ ).

CASE 5: The principle of virtual work model is evaluated for n-module where  $n = [1, 2, 3]$  with 3mm joint length and with frictional consideration ( $\mu_f = 0.25, \mu_R = 0.25$ ).

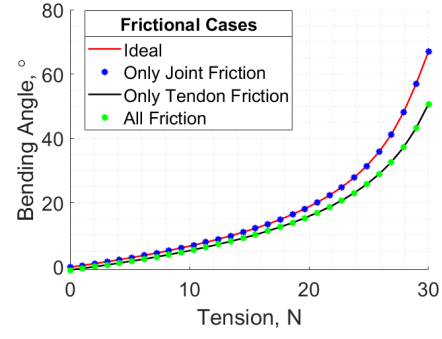
CASE 6: The principle of virtual work model is evaluated for n-module where  $n = [1, 2, 3]$  with 6mm joint length and without frictional consideration ( $\mu_f = \mu_R = 0$ ).

CASE 7: The principle of virtual work model is evaluated for  $n$ -module where  $n = [1, 2, 3]$  with  $6mm$  joint length and with frictional consideration ( $\mu_f = 0.25, \mu_R = 0.25$ ).

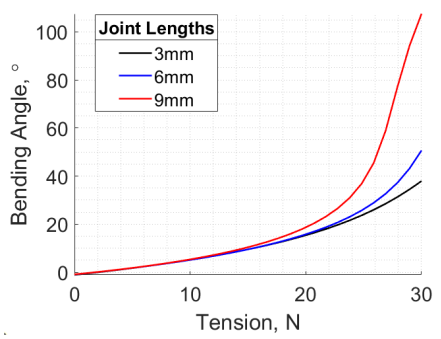
CASE 8: The principle of virtual work model is evaluated for 2-module with  $6mm$  joint length for an ideal situation with independent joint tube material properties with three sets of tube shear modulus  $(\mu_1, \mu_2) = [0.91, 0.91; 0.91, 0.5; 0.5, 0.5]N/mm^2$ .



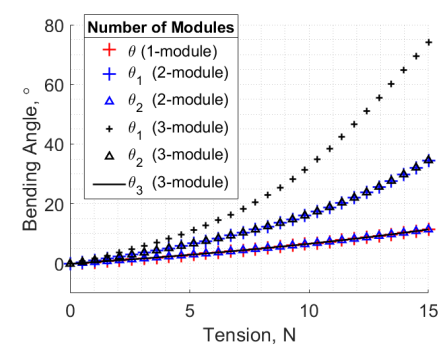
(a) Case 1



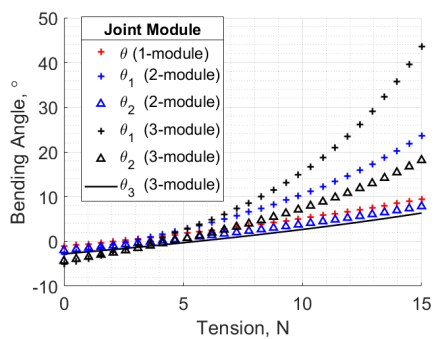
(b) Case 2



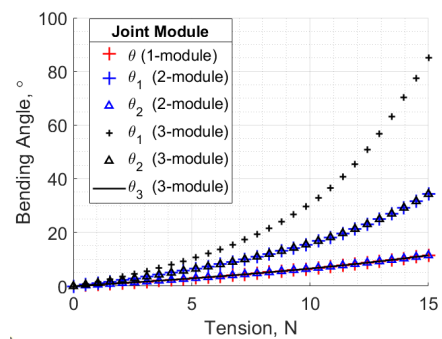
(c) Case 3



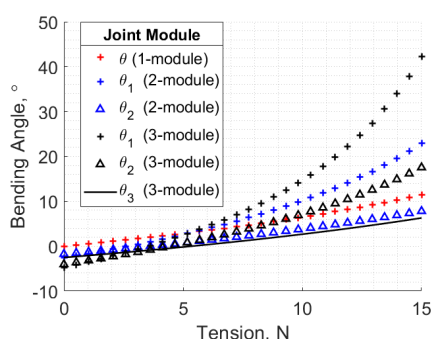
(d) Case 4



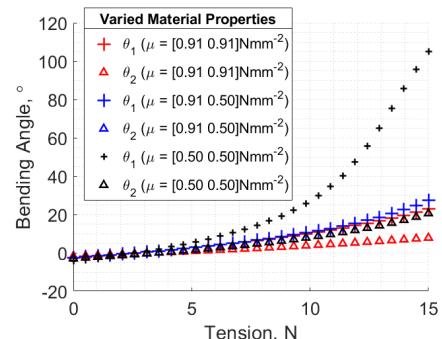
(e) Case 5



(f) Case 6



(g) Case 7



(h) Case 8

110  
Figure 3.14: Tension-Bend Angle Analysis for Cases 1-8



#### 3.4.4 Discussion on Virtual Work Model Analysis for Multi-Joint Continuum Segment Modules

For Case 1, Fig. 3.14a shows the comparison between the bend angle responses obtained using the virtual work and quasi-static model for a single module configuration with joint lengths 3, 6 and 9mm. The results show good agreement and suggest confidence in the use of the virtual work model for further evaluation of the continuum segment behavior.

The results of Case 2 for a single module in an ideal situation experiencing an observable upward nonlinear bend angle response for the tension range considered are shown in Fig. 3.14b. When the model is evaluated for the same design parameters with added friction at the joint, there is no observable difference. However, minor variations exist in the third decimal place between the bend angle-tension responses for an ideal situation and one with joint friction despite increasing the magnitude of the coefficient of static friction at the joint as shown in Table 3.6. These variations are attributed to the small mass of the vertebrae ( $\sim 299mg$ ) and the small surface of interaction between the male and female snap-in features as opposed to that between the tendon and tendon channel. Evaluating the model for the same design parameters with added friction between the tendon and the channel, an observable nonlinear variation is present between the ideal and only tendon friction configuration. This is expected since energy is lost to overcome friction due to the relative motion between the tendon and the tendon channel. This loss leads to a smaller bend angle response for the same tension for the tendon-channel frictional situation as compared to the ideal case.

For Case 3, when the joint and tendon friction are added for a more realistic behavior of the single continuum module with 3, 6 and 9mm joint lengths, it is observed that the bend angle response is larger when the joint length is increased. However, the responses in Case

3 are lower than the responses of their corresponding configuration in Case 1 as a result of the added friction.

In Case 4, it is observed that the base joint bend angle is always the largest and reduces progressively for the subsequent joints. For example, for a 2-module configuration, the base joint,  $\theta_1$  is larger than  $\theta_2$  and for a 3-module configuration,  $\theta_1 > \theta_2 > \theta_3$ . This is attributed to the inward propagation of energy from the distal joint due to the distal fixed actuating tendon progressively to the base of the continuum segment.

In Case 5, the analysis for Case 4 is repeated with friction. The observable equal response of the corresponding joints for n-modules is absent. In fact, increasing the number of modules in the continuum segment causes the distal joint bend angle to have a slightly lower response. Similarly, the corresponding joints for n-modules, when higher number of modules are used, exhibit lower bend angle response as a result of the presence of more losses in the channels and at the joints.

The responses observed for Cases 6 and 7 are greater and similar in trends to Cases 4 and 5 respectively because the analysis has the same design parameters but for different joint lengths. In Cases 6 and 7 a larger joint length of  $6mm$  was used compared to  $3mm$  used in Cases 4 and 5. Comparing Cases 5 and 7 (non-ideal evaluation), Case 7 has slightly greater responses for all corresponding configurations than Case 5 and would increase significantly for higher applied tension range. The negative bend angle values between the  $0 - 6N$  tension range of Case 7 are practically impossible but evaluated to determine the minimum applied tension required to obtain a joint response as a result of the frictional interactions and module configuration.

The results of Case 8 show the effect of independently defined joint tube material properties for a 2-module configuration. The results show that selecting more elastic (or less “stiff”)

joint tubes will result in a significant bend angle response for the base joint as compared to the distal joint or subsequent joints if other design configurations were used. While “stiffer” joint tubes will lead to smaller distal joint response. However, when one joint tube (the distal joint in this case) is less “stiff” and the base joint is stiffer, the variation in the bend angle responses of both joints reduces which suggests that the joint tubes for an n-module continuum segment configuration do not only act as an additional structural component or provide compliance to the overall continuum segment but also provide the ability to obtain unique joint configurations when the individual joint compliance is tuned with a combination of predefined joint tubes with unique material properties despite frictional effects. The tension-bend angle trends for the distal joints of the module configurations with shear moduli  $(\mu_1, \mu_2) = (0.91, 0.50)Nmm^{-2}$  and  $(\mu_1, \mu_2) = (0.50, 0.50)Nmm^{-2}$  overlap as a result of the identical distal joint tube material properties selected for each configuration.

The significance of these studies provides the basis for understanding the effects of various continuum segment design parameters on the behavior and performance of the continuum segment for possible use in different diagnostic scenarios and environments.

Table 3.6: Tension Bend Angle Behavior for a Single Module with Varying Joint Friction

Tension (N)	Bend Angle (°) $\mu_R = 0$	Bend Angle (°) $\mu_R = 0.25$	Bend Angle (°) $\mu_R = 0.5$	Bend Angle (°) $\mu_R = 1$
0.1000	0.0470	0.0468	0.0467	0.0465
1.7600	1.7234	1.7232	1.7231	1.7229
3.4100	3.6393	3.6391	3.6389	3.6387
5.0700	5.8644	5.8642	5.8640	5.8637
6.7200	8.5032	8.5030	8.5027	8.5025
8.3800	11.7217	11.7214	11.7212	11.7209
10.0300	15.8055	15.8051	15.8048	15.8044
11.6900	21.3047	21.3043	21.3039	21.3034
13.3400	29.4668	29.4661	29.4656	29.4649
15.0000	43.7495	43.7485	43.7476	43.7464

## CHAPTER 4

### EXPERIMENTAL ANALYSIS: INITIAL TENDON-BEND ANGLE CHARACTERIZATION

#### 4.1 Experimental Setup

Tension-bend angle experiments were performed using single continuum modules with joint lengths 3, 6, 9 and 12 $mm$ . The results are compared with those from the quasi-static analytical model (see section 3.3). Single vertebrae components for each joint length were fabricated using the Anycubic 3D printer (see section 2.6) and modules were assembled as described in [105]. In the tension-bend angle experiments, the single continuum module was secured at the base vertebra as shown in Fig. 4.1. A 0.58 $mm$  diameter Zebco<sup>®</sup> monofilament fishing line (with 13.6 $kg$  maximum capacity) is used as the actuating tendon. The free end of the tendon is fastened to a weight bucket. The bucket is randomly loaded with weights and used to actuate the module to obtain a bend angle response. The weights are selected such that the total load applied on the actuation tendon is 2.98 to 5.92 $N$  at increments of 0.49 $N$ . The tendon elongation was experimentally determined to be 0.02% at the maximum load used and its effects were considered to be negligible on the response of the single module.

As the single continuum module is actuated, the bend configuration is captured using an IPEVO<sup>®</sup> document camera (<https://www.ipevo.com/>) and processed using computer vision (CV) to extract the module bend angle for each load. A CV algorithm was developed and implemented in MATLAB<sup>®</sup>. The single module actuation procedure is repeated with a different loading order using the same weights to prevent biasing the results. The bend

angles obtained for the two loading cases for each weight are averaged and presented as the experimental bend angle,  $\theta_{exp}$ .

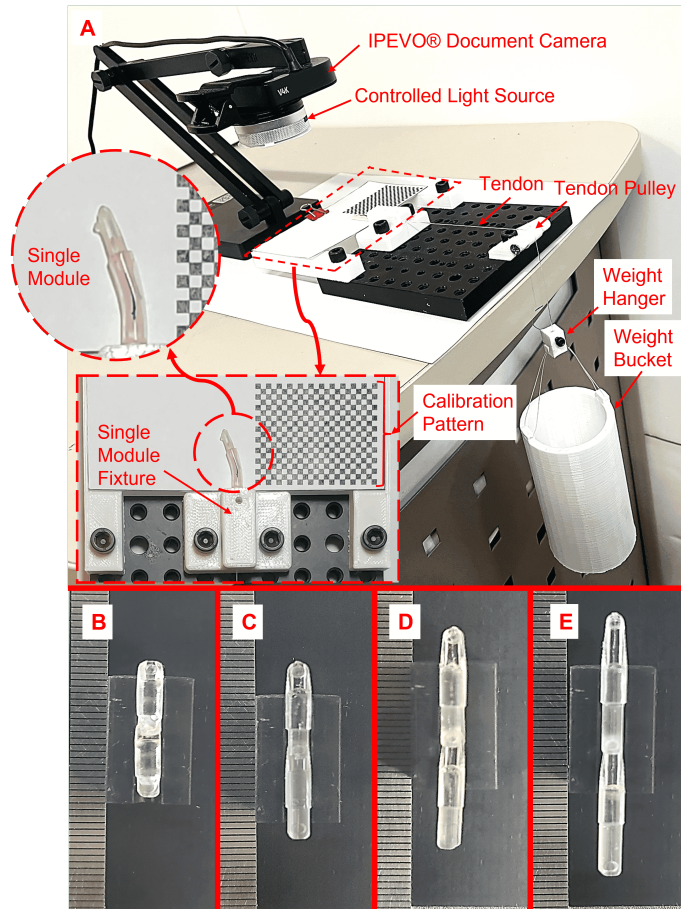


Figure 4.1: A. Experimental Setup to Characterize the Module Behavior without the Light-Controlled Environment. Single Module without Joint Tube for B.  $3mm$ , C.  $6mm$ , D.  $9mm$ , E.  $12mm$  Joint Lengths (scale in  $mm$ ).

#### 4.1.1 Bend Angle Measurement using Computer Vision

The CV algorithm (shown in Fig. 4.2) uses a  $2mm$  square calibration pattern placed at the background of the single continuum module actuation scene to obtain a relationship between pixel count and real world coordinates. A thin red colored line of known length,

$L_{cur}$ , is drawn along the robot central axis and on the entire length of the module joint. After the module is actuated, the curvature of the red colored line at the joint is captured by the camera and processed in MATLAB<sup>®</sup>. The CV algorithm first applies a color balance and light noise reduction on the actuated module captured image to improve image quality and then processes the output image to minimize distortion due to the camera lens. A red color segmentation is then applied to the image to obtain the pixels representing only the manipulator bend curvature as world coordinates. The world coordinates are then circle fitted using the least square method to obtain the radius of curvature,  $R_{cur}$ , and the center of the circle  $(h, k)$ . The experimental bend angle due to an applied tendon tension is computed as  $\theta_{exp} = L_{cur}/R_{cur}$ .

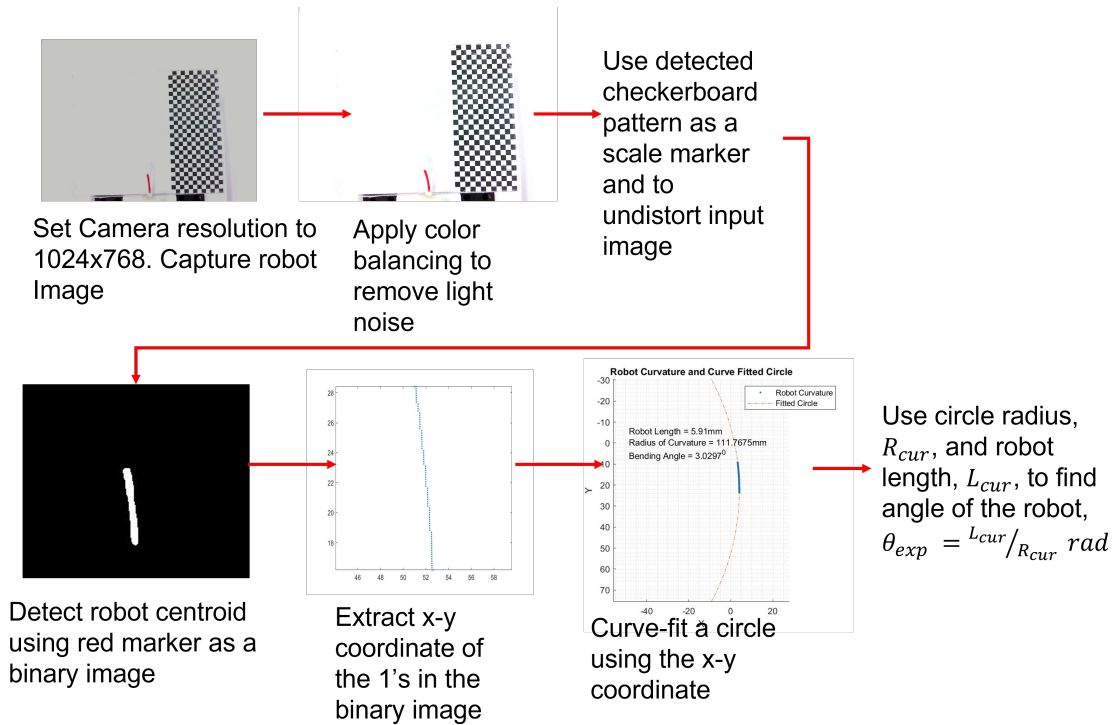


Figure 4.2: Computer Vision Flowchart for Bending Angle Measurement.

Figure 4.3 presents the schematic of the curvature and bend angle extraction. The orange dots are the computer vision-acquired pixels and their real-world coordinates,  $(x_i, y_i)$ .  $R$  is the radius formed by connecting two joining lines from the beginning and end of the computer vision pixel curve fit curve. The intersection of these two lines is the center of a circle. Using Fig. 4.3, the solution for the radius of curvature,  $R_{cur}$  and center of the curve fitted circle  $(h, k)$  using least-square method fit is established from the generalized equation of a circle shown in Eq. 4.1. First, the coordinates  $(h, k)$  of the center of the circle are established and then the radius of the circle is evaluated.

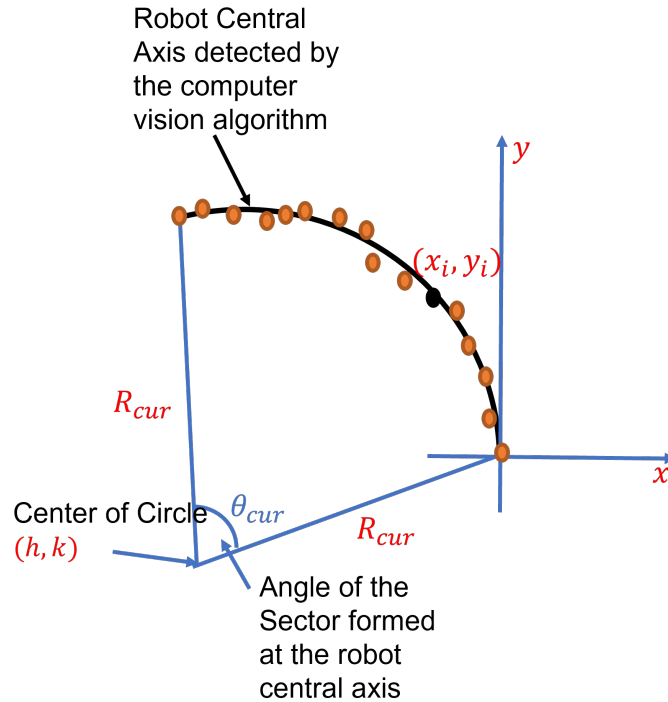


Figure 4.3: Schematic for the Analysis of Robot Curvature Geometric Parameters.

$$x^2 + y^2 = (R_{cur}^2 - (h^2 + k^2)) + 2hx + 2ky \quad (4.1)$$



Considering the computer vision extracts the  $(x_i, y_i)$  coordinates of the robot central axis, Eq. 4.1 can be written for each extracted coordinate as Eq. 4.2 where  $e = (R_{cur}^2 - (h^2 + k^2))$  and in matrix form as shown in Eqs. 4.3 and 4.4 . As a result,  $(h, k)$ ,  $e$ , and by extension,  $R_{cur}$  can be evaluated. Equation 4.4 is solved for  $h$ ,  $k$ , and  $e$  and then  $R_{cur}$  is estimated. The angle of the sector,  $\theta_{cur}$ , formed between the two radii extended from the base and top of the robot curved central axis to the center,  $(h, k)$ , is the robot bend angle.

$$\begin{aligned}
2hx_1 + 2ky_1 + e &= x_1^2 + y_1^2 \\
2hx_2 + 2ky_2 + e &= x_2^2 + y_2^2 \\
&\vdots \\
2hx_n + 2ky_n + e &= x_n^2 + y_n^2
\end{aligned} \tag{4.2}$$

$$\begin{bmatrix} 2hx_1 & 2ky_1 & e \\ 2hx_2 & 2ky_2 & e \\ \vdots & \vdots & \vdots \\ 2hx_n & 2ky_n & e \end{bmatrix} = \begin{bmatrix} 2x_1 & 2y_1 & 1 \\ 2x_2 & 2y_2 & 1 \\ \vdots & \vdots & \vdots \\ 2x_n & 2y_n & 1 \end{bmatrix} \cdot \begin{bmatrix} h \\ k \\ e \end{bmatrix} = \begin{bmatrix} x_1^2 + y_1^2 \\ x_2^2 + y_2^2 \\ \vdots \\ x_n^2 + y_n^2 \end{bmatrix} \tag{4.3}$$

$$\begin{bmatrix} h \\ k \\ e \end{bmatrix} = inv \left( \begin{bmatrix} 2x_i & 2y_i & 1 \end{bmatrix} \right) \cdot \begin{bmatrix} x_i^2 + y_i^2 \end{bmatrix} \tag{4.4}$$

## 4.2 Single Continuum Module Equivalent Shear Modulus Estimation

Visual inspection of the module joint reveals an interesting behavior as the module bends due to applied tension; the sides of the tube undergoing extension and compression interact with the stationary or rotating vertebra differently. The profile of a single module for  $(3, 6, 9, 12)mm$  joint lengths is shown in Fig. 4.4. The side of the joint tube in tension

interacts with the vertebrae as outlined in green, while the tendon (in red) interacts with the side of the tube in compression as shown. The bending profiles of the continuum module were recreated in the CAD model using tension-bend angle data from experiments and show that both the tendon and vertebra interact with the tube by recessing into the tube. Examining the joint interactions across the different joint lengths shows that at  $2.92N$  the  $3mm$  joint length experiences relatively minimal vertebra-tube interaction and no tendon-tube interaction. However, it is observed that the vertebra and tendon push further into the tube as the length increases. When the applied load is increased to  $5.92N$ , the interactions become more prominent for the larger joint lengths.

These interactions introduce constrictions along the tube active bend regions that influence the characteristics of the joint tube as a function of both the joint bend angle and active length.

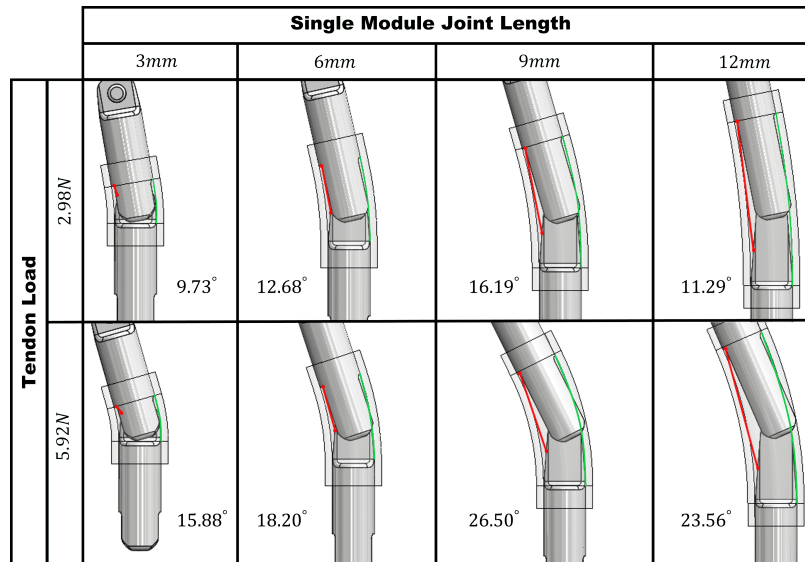


Figure 4.4: Joint Tube Interaction with Vertebrae and Tendon during Bending; red and green solid lines represent the tendon path and interior tube wall.

The experimentally determined tension-bend angle measurements for the prototyped single module with joint lengths measuring (3, 6, 9, and 12)mm were used along with Eqs. (3.21 - 3.23) to estimate an experimental shear modulus,  $\mu_{exp}$ , of the joint tube. This evaluation is important to analytically estimate the continuum module responses to applied tension. It is expected that  $\mu_{exp}$  for each module joint configuration will vary due to the geometric parameters (i.e active length, ID, OD, and/or thickness) of the tube, the module bend angle, and the joint interaction between the vertebrae during bending. As such an equivalent shear modulus that captures all interactions is estimated. The joint tube ID and OD are fixed for all module configurations. The estimated equivalent shear modulus,  $\mu_{est,eq}$ , can be empirically characterized in a generalized form for different joint lengths as a bivariate polynomial function of the module joint length, ( $L = l_1 + l_2$ ), and bend angle,  $\theta$ , using Eq. 4.5 as proposed by Akima [106].

$$\mu_{est,eq}(L, \theta) = \sum_{\bar{n}=0}^2 \left( \sum_{\bar{m}=0}^{4-\bar{n}} p_{\bar{n}\bar{m}} L^{\bar{n}} \theta^{\bar{m}} \right) \quad (4.5)$$

where  $\bar{n}$  and  $\bar{m}$  are the order of the  $L$  and  $\theta$  variables in the polynomial.  $p_{\bar{n}\bar{m}}$  are the coefficients and estimated as  $(p_{00}, p_{01}, p_{02}, p_{03}, p_{04}, p_{10}, p_{11}, p_{12}, p_{13}, p_{20}, p_{21}, p_{22}) = (2.73, -26.03, 89.28, -101.30, 2.54, -0.77, 6.76, -18.02, 15.02, 0.03, -0.25, 0.42)$ .

### 4.3 Experimental and Quasi-Static Model Tension-Bend Angle Results of a Single Continuum Module

The tension-bend angle experimental results (see Table 4.1) are compared to results obtained using the quasi-static analysis with the average experimental bend angles as inputs into Eqs. (3.21-3.23). Figure 4.5 presents the experimental and quasi-static tension-bend angle responses for each joint length.

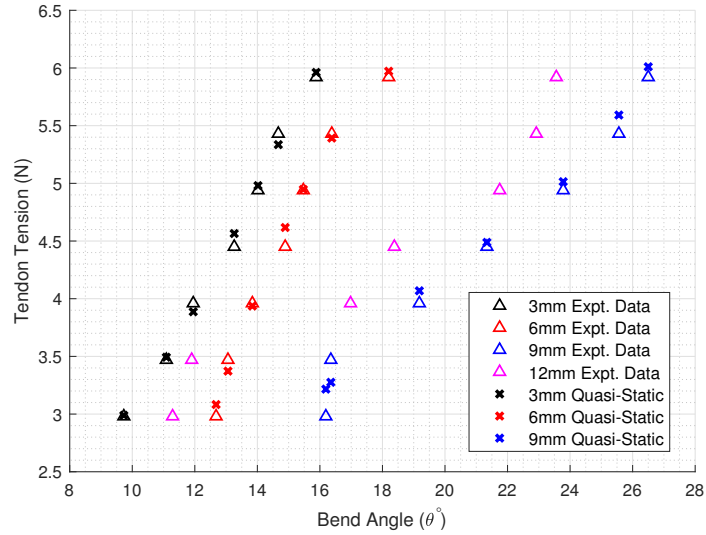


Figure 4.5: Experimental and Quasi-Static Model Evaluated Tension-Bend Angle Responses for (3, 6, 9, 12)mm Joint Lengths.

The average experimental bend angle obtained for the tendon tension as presented in Table 4.1 shows repeatability with a maximum difference of ( $2^\circ$ ,  $1^\circ$ ,  $0.9^\circ$ , and  $0.9^\circ$ ) during successive bend angle measurements for the (3, 6, 9, and 12)mm joint length respectively. The bend angles obtained using the same tension range increase as the joint length increases from 3 to 9mm and is attributed to the larger moment arm generated during bending by the increased joint length and the easier-to-bend longer joint elastic tubes. However, the 12mm joint length has a response that does not follow the trends observed for the (3, 6, 9)mm joint lengths, where joint interactions between the tube, vertebrae, and tendon are considerably more notable. The regions of the tube undergoing uniform compression and extension during bending essentially alter the expected uniform bending behavior of the tube. This behavior is also observed when comparing the experimentally estimated shear moduli,  $\mu_{exp}$ , shown in Table 4.1, for each joint length. As the tension increases, the  $\mu_{exp}$  ranges from  $0.21 - 0.31 Nmm^{-2}$  for 3mm,  $0.20 - 0.34 Nmm^{-2}$  for 6mm,  $0.21 - 0.36 Nmm^{-2}$  for 9mm, and  $0.27 - 0.44 Nmm^{-2}$  for 12mm joint lengths.

Table 4.1: Tension-bend Angle Comparison from Experimental and Quasi-Static Model Analysis

Exp. Tendon Tension, (N)	3mm Joint Length					6mm Joint Length					9mm Joint Length					12mm Joint Length				
	Experimental Bend Angle, (°)		Exp. Shear Modulus ( $Nmm^{-2}$ )	Quasi Static Model Tension (N)	Experimental Bend Angle, (°)		Exp. Shear Modulus ( $Nmm^{-2}$ )	Quasi Static Model Tension (N)	Experimental Bend Angle, (°)		Exp. Shear Modulus ( $Nmm^{-2}$ )	Quasi Static Model Tension (N)	Experimental Bend Angle, (°)		Exp. Shear Modulus ( $Nmm^{-2}$ )	Quasi Static Model Tension (N)	Experimental Bend Angle, (°)		Exp. Shear Modulus ( $Nmm^{-2}$ )	Quasi Static Model Tension (N)
	Case 1	Case 2			Case 1	Case 2			Case 1	Case 2			Case 1	Case 2			Case 1	Case 2		
2.98	9.12	10.33	9.73	0.20	2.96	12.47	12.90	12.68	0.20	3.04	16.04	16.33	16.19	0.21	3.13	11.05	11.52	11.29	0.27	2.98
3.47	10.42	11.76	11.09	0.22	3.48	12.75	13.37	13.06	0.23	3.34	16.19	16.50	16.35	0.24	3.19	11.46	12.33	11.90	0.31	3.41
3.96	11.19	12.72	11.95	0.24	3.86	13.77	13.91	13.84	0.25	3.91	19.18	19.17	19.18	0.26	3.98	16.88	17.09	16.98	0.32	4.50
4.45	12.25	14.27	13.26	0.26	4.53	14.93	14.86	14.89	0.27	4.58	20.88	21.80	21.34	0.29	4.38	18.32	18.44	18.38	0.35	4.44
4.94	13.02	15.03	14.02	0.28	4.94	15.43	15.50	15.47	0.30	4.90	23.33	24.24	23.78	0.31	4.90	21.59	21.91	21.75	0.37	4.85
5.43	13.69	15.66	14.67	0.30	5.30	16.50	16.27	16.38	0.32	5.34	25.28	25.84	25.56	0.33	5.46	23.11	22.73	22.92	0.40	5.42
5.92	14.94	16.81	15.88	0.31	5.93	18.72	17.68	18.20	0.34	5.91	26.35	26.65	26.50	0.36	5.84	23.44	23.67	23.56	0.44	5.87
			Mean	0.26				Mean	0.27				Mean	0.29				Mean	0.35	
			SD	0.04				SD	0.05				SD	0.05				SD	0.05	

The average experimental shear moduli,  $\mu_{exp}$ , for each joint length were also compared and found to be  $(0.26, 0.27, 0.29, \text{ and } 0.35)Nmm^{-2}$  with standard deviation, SD,  $(0.04, 0.05, 0.05, \text{ and } 0.05)Nmm^{-2}$  for the joint lengths of  $(3, 6, 9, \text{ and } 12)mm$  respectively. It is observed that the average  $\mu_{exp}$  for  $12mm$  is significantly larger than those for the other joint lengths with an estimated difference of  $\sim 21\%$ . As a result, larger joint lengths ( $> 9mm$ ) do not follow the observed trends and should be carefully analyzed if they are to be considered during the design phase of the continuum segment of the robot.

As such, the experimentally evaluated shear modulus for the  $12mm$  joint length is not used in estimating an equivalent or generalized shear modulus for the single module as a function of the joint length and bend angle using the bivariate equation Eq. 4.5.

The goodness of fit parameters for the generalized  $\mu_{est,eq}(L, \theta)$  are evaluated as  $SSE = 1.5 \times 10^{-3}$ ,  $R^2 = 0.99$  with an adjusted  $R_{adj}^2 = 0.97$  and  $RMSE = 10.0 \times 10^{-3}$ . These parameters indicate that the generalized  $\mu_{est,eq}(L, \theta)$  expression (Eq. 4.5) fits well the data while the high value for  $R_{adj}^2$  indicates a correlation between the different joint lengths and bend angle that does not adversely affect  $\mu_{est,eq}(L, \theta)$  [107]. Therefore, the generalized  $\mu_{est,eq}(L, \theta)$  is a good predictor of joint compliance behavior for the range of joint lengths considered and the evaluated bend angles.

The obtained  $\mu_{est,eq}(L, \theta)$  function is then validated with a set of independent shear moduli values obtained from seven (7) new sets of experimental tension-bend angle data for each of the  $(3, 6, 9)mm$  joint lengths with non-previously used weights following the procedure described in section 4.2. The comparison between these independent shear moduli and the  $\mu_{est,eq}(L, \theta)$  values obtained from the joint lengths and unique experimental bend angle values is performed by evaluating the sum of squares error,  $SSE_{Val}$ , and root mean square error,  $RMSE_{Val}$ , to be  $10.2 \times 10^{-3}$  and  $19.1 \times 10^{-3}$  respectively, indicating the low deviation between  $\mu_{est,eq}(L, \theta)$  and the experimentally obtained shear modulus.

This analysis reinforces the use of the generalized  $\mu_{est,eq}$  function in Eq. 4.5 to estimate the experimental equivalent shear modulus of the joint tube to describe the behavior and tension-bend angle response of the single module.

The quasi-static evaluated tension-bend angle responses using the  $\mu_{est,eq}(L, \theta)$  correlate well with the experimental tension-bend angle response as shown in Fig. 4.5. The maximum error between the experimental and quasi-static responses for (3, 6, 9)mm joint lengths are 0.10N, 0.13N, and 0.28N respectively.

#### 4.4 Multi-Module Continuum Segment Prototyping and Initial Characterization

Multi-joint continuum modules with joint lengths 3 and 6mm were fabricated and prototyped following the procedure discussed in section 4. These modules were chosen for further analysis particularly because of the absence of interaction between the tube and the vertebrae that allows for a true characterization of the joints of the continuum segment. The joints of the modules are highlighted with different colors along the robot central axes for bending angle image capture. Two and three joint configurations of these modules as presented in Fig. 4.6 are characterized using the same methods discussed in section 4. The tension-bend angle relationship from the experimental analysis is presented in Tables 4.2 and 4.3 (for 2-module configuration), and Tables 4.4 and 4.5 (for 3-module configuration), with the experimental relationships plotted in Fig. 4.7.

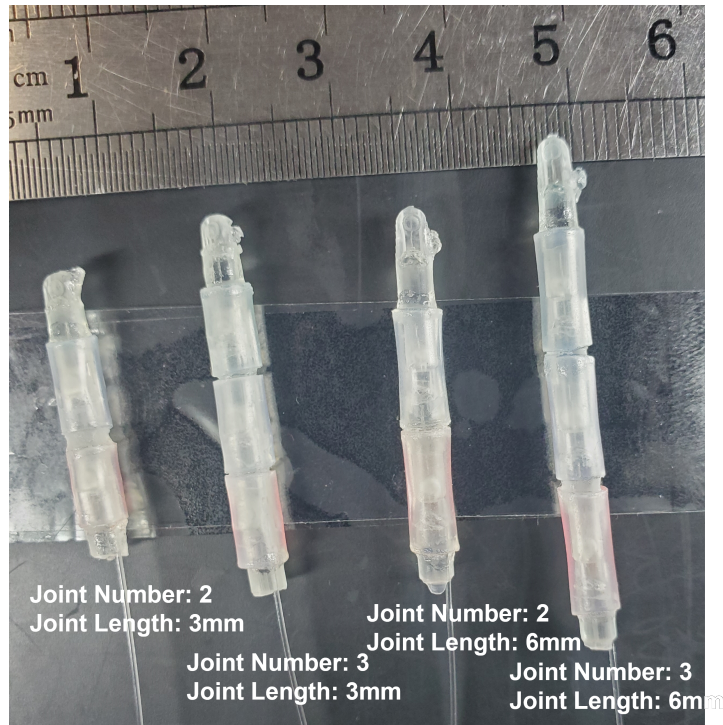


Figure 4.6: Prototyped Continuum Segment Modules for 2 and 3 Joints with 3 and 6mm Joint Lengths

Table 4.2: Experimental Tension-Bend Angle Results for Two Joint Modules with 3mm Joint Lengths

Number of Joint	Exp. Tendon Tension (N)	3mm Joint Length						
		Experimental Bend Angle, (°)						Overall Bend Angle
		Case 1		Case 2		Avg. Joint 1	Avg. Joint 2	
		Joint 1	Joint 2	Joint 1	Joint 2			
2	4.94	8.74	4.49	7.78	3.88	8.26	4.19	12.44
	5.43	12.75	3.73	6.68	4.34	9.71	4.04	13.75
	5.92	10.02	4.28	6.16	4.47	8.09	4.37	12.46
	6.41	12.53	4.51	6.63	4.36	9.58	4.44	14.02
	6.90	11.47	4.29	6.04	4.77	8.75	4.53	13.28
	7.40	11.12	5.16	6.39	5.29	8.76	5.23	13.99
	7.89	10.44	5.15	7.32	6.07	8.88	5.61	14.49



Table 4.3: Experimental Tension-Bend Angle Results for Two Joint Modules with 6mm Joint Lengths

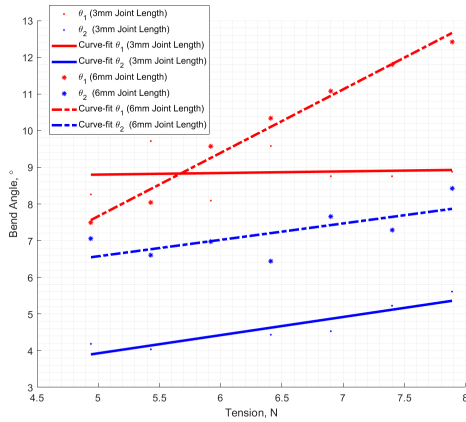
Number of Joint	Exp. Tendon Tension (N)	6mm Joint Length						
		Experimental Bend Angle, (°)						
		Case 1		Case 2		Avg. Joint 1	Avg. Joint 2	Overall Bend Angle
		Joint 1	Joint 2	Joint 1	Joint 2			
2	4.94	7.19	7.22	7.79	6.88	7.49	7.05	14.54
	5.43	7.98	6.86	8.10	6.35	8.04	6.60	14.65
	5.92	9.17	7.00	9.99	6.96	9.58	6.98	16.56
	6.41	9.51	6.24	11.18	6.64	10.34	6.44	16.79
	6.90	10.52	7.47	11.64	7.85	11.08	7.66	18.74
	7.40	12.01	7.17	11.60	7.41	11.81	7.29	19.09
	7.89	12.24	7.98	12.60	8.86	12.42	8.42	20.84

Table 4.4: Experimental Tension-bend Angle Results for Three Joint Modules with 3mm Joint Lengths

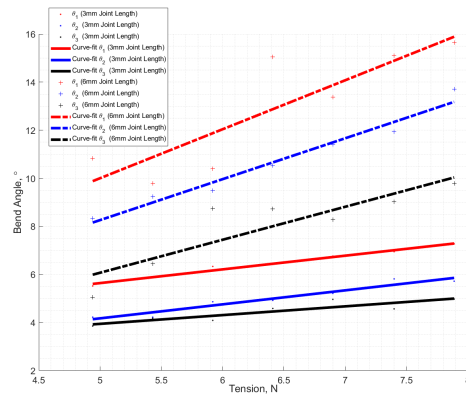
Number of Joint	Exp. Tendon Tension (N)	3mm Joint Length									
		Experimental Bend Angle, (°)									
		Case 1			Case 2			Avg. Joint 1	Avg. Joint 2	Avg. Joint 3	Overall Bend Angle
		Joint 1	Joint 2	Joint 3	Joint 1	Joint 2	Joint 3				
3	4.94	5.40	4.17	3.62	5.64	4.28	4.09	5.52	4.23	3.86	13.60
	5.43	5.72	3.96	4.06	6.02	4.49	4.30	5.87	4.22	4.18	14.28
	5.92	6.11	4.87	3.88	6.56	4.86	4.30	6.33	4.87	4.09	15.29
	6.41	6.42	4.91	4.23	6.41	4.93	4.94	6.42	4.92	4.58	15.92
	6.90	6.72	4.93	5.09	6.81	5.49	4.84	6.77	5.21	4.97	16.94
	7.40	6.96	5.75	4.40	6.93	5.88	4.74	6.95	5.82	4.57	17.33
	7.89	7.48	5.66	4.84	7.07	5.78	5.11	7.27	5.72	4.97	17.96

Table 4.5: Experimental Tension-bend Angle Comparison for Three Joint Modules with 6mm Joint Lengths

Number of Joint	Exp. Tendon Tension (N)	6mm Joint Length									
		Experimental Bend Angle, (°)									Overall Bend Angle
		Case 1			Case 2			Avg. Joint 1	Avg. Joint 2	Avg. Joint 3	
Joint 1	Joint 2	Joint 3	Joint 1	Joint 2	Joint 3	Joint 1	Joint 2	Joint 3	Joint 3		
3	4.94	10.56	8.60	4.38	11.09	8.07	5.72	10.83	8.33	5.05	24.21
	5.43	9.67	8.63	4.15	9.90	9.85	8.75	9.79	9.24	6.45	25.48
	5.92	9.50	9.40	8.90	11.30	9.58	8.60	10.40	9.49	8.75	28.64
	6.41	16.16	10.43	8.02	13.93	10.64	9.43	15.04	10.54	8.73	34.31
	6.90	12.71	11.95	8.54	14.03	10.88	8.01	13.37	11.42	8.28	33.06
	7.40	14.60	12.37	9.66	15.59	11.50	8.40	15.10	11.94	9.03	36.06
	7.89	16.04	14.26	8.95	15.24	13.15	10.62	15.64	13.71	9.78	39.13



(a) Experimental Tension-Bend Angle Behavior for 2 Joint Modules with 3 and 6mm Joint Lengths



(b) Experimental Tension-Bend Angle Behavior for 3 Joint Modules with 3 and 6mm Joint Lengths

Figure 4.7: Experimental Tension-Bend Angle Behavior for 2 and 3 Joint Modules with 3 and 6mm Joint Lengths

#### 4.4.1 Experimental Analysis with Multi-Joint Continuum Segment Modules Discussions

The average experimental bend angles obtained for the tendon tension for a 2-module configuration as presented in Tables 4.2 and 4.3 show repeatability with a maximum difference of ( $6^\circ$  and  $1.68^\circ$ ) during successive bend angle measurements for the 3 and 6mm joint

length respectively. The higher error in the base joint bend angle of the  $3mm$  joint length 2-module configuration is due to the bifurcation at larger stresses in the tube that leads to instability in the joint compliance. As predicted by the virtual work model, the bend angle for the base joint is always greater than that for the distal joint in both the 3 and  $6mm$  joint length configurations. The overall bend angles obtained using the same tension range increase as the joint length increases from 3 to  $6mm$  and is attributed to the larger moment arm generated during bending by the increased joint length and the easier bending of the longer tube. Furthermore, the bend angle trend for the base joint,  $\theta_1$ , of the  $6mm$  joint length configuration is greater than the base joint,  $\theta_1$ , of the  $3mm$  joint length configuration due to the relation between the propagation of energy from the distal joint towards the base joint and the joint tube length to diameter ratio all acting to affect the magnitude of the base joint.

When the module number in the continuum segment is increased from 2 to 3, the base joint continues to exhibit the largest response as shown in Tables 4.4 and 4.5, and Figs. 4.7a and 4.7b. However, the bend angle for each joint of the  $6mm$  joint length, 3-module configuration is greater than their corresponding joint of the  $3mm$  joint length configuration.

The virtual work model evaluated tension-bend angle trends correlated to the trends of the experimental tension-bend angle analysis for the same continuum segment configurations. Albeit, there is a disassociation between the magnitudes of the responses for the theoretical and experimental analysis because the coefficient of friction at the joints and between the tendon and channels, and the tube material properties are not known but assumed.

## CHAPTER 5

### CONCLUSIONS

The aim of this dissertation was to investigate accessing the bladder through the urethra natural orifice with minimum patient trauma toward quantitative viscoelastic tissue assessment. A robotic manipulator was conceptualized in the form of NOTES and SPA technologies with two subsystems; a hybrid-rigid continuum segment and a hyper-spherical actuation mechanism that could be outfitted with an end-of-arm force sensor for direct transurethral bladder wall interrogation.

The usefulness of this robot arises from the lack of tools for quantitative characterization of localized viscoelastic bladder tissue properties through contact palpation for improved disease prognosis and diagnosis. The architecture and motion study of the robot consisting of a multi-vertebrae continuum segment and a rigid hyper-spherical joint arrangement for normal bladder tissue wall palpation were investigated. Structural analysis was used to evaluate and iterate the design of the continuum segment to arrive at an acceptable design architecture that met the design requirements for a 1N end effector reaction load considering the manufacturing methods used. Consecutive vertebrae form rotational joints held together using elastic tubes. The behavior of a joint depends on the bending characteristics of the encompassing elastic tube which in turn depends on tube material and geometric properties and joint geometry. Further investigation to estimate an acceptable continuum segment geometry was carried out by formulating a geometry design optimization considering motion constraints.

Manufacturing experiments were carried out to investigate the manufacturing of the components of the continuum segment using multiple inverted vat-polymerization technologies to improve part quality with minimal defects. The results show that considerable trade-offs exist across these technologies for the different process parameters considered.

A Jacobian-based inverse differential kinematics methodology is developed to ensure continuous joint motion and to prevent discontinuities and singularities while meeting the desired pose for palpation. The inverse kinematics approach was successfully demonstrated to achieve user-defined error levels in position and orientation. An analytical strain energy quasi-static model for the continuum segment was developed and analyzed for three different tube material properties and four joint geometries. The discrete results from the model were used to predict an exponential relationship between the joint bend angle and the applied tension and joint geometry. A single module of the continuum segment was prototyped for four different joint lengths for tension-bend angle characterization using a custom-developed experimental setup and computer vision. The experimental results were used to develop a bivariate equivalent bending modulus relationship for the encompassing elastic tube as a function of joint geometry and bend angle. The experimental and analytical quasi-static analysis shows a high correlation, particularly for joint lengths (3, 6, 9)mm. However, the single module with joint length 12mm was observed to have significant interactions between the elastic tube, vertebrae geometry and actuating tendon that affect the joint behavior.

The principle of virtual work was also used to formulate a model of a multi-module continuum segment considering frictional interactions. Hence improving the Quasi-static model and associated analysis. While further experimental analysis was conducted using 2 and 3 joints continuum modules for 3mm and 6mm joint lengths. The results of the analysis of the virtual work model and the experiments show trends with high fidelity. These results

show that as the joint length increases, the continuum module overall bend angle increases with the base joint experiencing significant bending. The results also show that as the joint number of the continuum segment is increased, each joint also experiences an increase in bend angle while frictional loss exists.

The results of the presented work contribute to the understanding of the parameters that affect the behavior of the proposed robot due to its unique continuum architecture and robots with similar design and mechanical architecture. Further studies, development, and prototyping of the robot manipulator actuation mechanism are needed to evaluate the overall functionality of the manipulator. For clinical usefulness, the fully functional robot manipulator would require the integration of the force sensor and examinations to assess the robot safety and performance in a simulated environment.

## REFERENCES

- [1] “Interactive 3d anatomy - disease platform,” Nov 2022. [Online]. Available: <https://www.biodigital.com/>
- [2] “Cystoscopy & ureteroscopy,” Nov 2022. [Online]. Available: <https://www.niddk.nih.gov/health-information/diagnostic-tests/cystoscopy-ureteroscopy>
- [3] Ge logiq s8 ultrasound machine. [Online]. Available: <https://www.iusimaging.com/product/ge-logiq-s8-ultrasound-machine-2/>
- [4] Cystectomy. [Online]. Available: <https://brisbaneurologyclinic.com.au/procedures-we-perform/cystectomy/>
- [5] S. A. Adejokun, “Flexible-continuum robot for bladder tissue diagnostics,” Master’s thesis, University of Texas, Arlington, 2017.
- [6] Formlabs, grey resin, safety data sheet. [Online]. Available: <https://formlabs-media.formlabs.com/datasheets/1801046-SDS-ENUS-0.pdf>
- [7] P. Veerabhadram, “Applications of robotics in medicine,” International Journal of Scientific & Engineering Research, vol. 2, no. 8, 2011.
- [8] J. Bonatti, G. Vetovec, C. Riga, O. Wazni, and P. Stadler, “Robotic technology in cardiovascular medicine,” Nature Reviews Cardiology, vol. 11, no. 5, pp. 266–275, 2014.

- [9] C. Duret and J. Gracies, “Does upper limb robot-assisted rehabilitation contribute to improve the prognosis of post-stroke hemiparesis?” Revue Neurologique, vol. 170, no. 11, pp. 671–679, 2014.
- [10] N. Simaan, R. M. Yasin, and L. Wang, “Medical technologies and challenges of robot-assisted minimally invasive intervention and diagnostics,” Annual Review of Control, Robotics, and Autonomous Systems, vol. 1, pp. 465–490, 2018.
- [11] A. Jiang, S. Adejokun, A. Faragasso, K. Althoefer, T. Nanayakkara, and P. Dasgupta, “The granular jamming integrated actuator,” in 2014 International Conference on Advanced Robotics and Intelligent Systems (ARIS). IEEE, 2014, pp. 12–17.
- [12] S. Kolachalama and S. Lakshmanan, “Continuum robots for manipulation applications: a survey,” Journal of Robotics, vol. 2020, 2020.
- [13] G. Robinson and J. B. C. Davies, “Continuum robots-a state of the art,” in Proceedings 1999 IEEE international conference on robotics and automation (Cat. No. 99CH36288C), vol. 4. IEEE, 1999, pp. 2849–2854.
- [14] “Urinary incontinence,” Dec 2021. [Online]. Available: <https://www.mayoclinic.org/diseases-conditions/urinary-incontinence/symptoms-causes/syc-20352808>
- [15] M. E. Ellis, “Causes of urinary incontinence, treatments, and more,” Feb 2022. [Online]. Available: <https://www.healthline.com/health/urinary-incontinence>
- [16] “Urinary incontinence.” [Online]. Available: <https://www.urologyhealth.org/urology-a-z/u/urinary-incontinence>
- [17] “Surgery for female urinary incontinence.” [Online]. Available: <https://drmarcuscarey.com/bladder-problems/surgery-for-female-urinary-incontinence/>



- [18] I. Milsom, K. S. Coyne, S. Nicholson, M. Kvasz, C.-I. Chen, and A. J. Wein, “Global prevalence and economic burden of urgency urinary incontinence: a systematic review,” European urology, vol. 65, no. 1, pp. 79–95, 2014.
- [19] I. Nenadic, L. Mynderse, D. Husmann, M. Mehrmohammadi, M. Bayat, A. Singh, M. Denis, M. Urban, A. Alizad, and M. Fatemi, “Noninvasive evaluation of bladder wall mechanical properties as a function of filling volume: potential application in bladder compliance assessment,” PLoS One, vol. 11, no. 6, p. e0157818, 2016.
- [20] C. Li, G. Guan, F. Zhang, S. Song, R. K. Wang, Z. Huang, and G. Nabi, “Quantitative elasticity measurement of urinary bladder wall using laser-induced surface acoustic waves,” Biomedical optics express, vol. 5, no. 12, pp. 4313–4328, 2014.
- [21] M. A. Soebadi, T. Weydts, L. Brancato, L. Hakim, R. Puers, and D. De Ridder, “Novel implantable pressure and acceleration sensor for bladder monitoring,” International Journal of Urology, vol. 27, no. 6, pp. 543–550, 2020.
- [22] C. Sozer, M. Ghorbani, G. Alcan, H. Uvet, M. Unel, and A. Kosar, “Design, prototyping and control of a flexible cystoscope for biomedical applications,” IOP Conference Series: Materials Science and Engineering, vol. 224, p. 012050, jul 2017. [Online]. Available: <https://doi.org/10.1088/1757-899x/224/1/012050>
- [23] D. Georgescu, E. Alexandrescu, R. Muțescu, and B. Geavlete, “Cystoscopy and urinary bladder anatomy,” in Endoscopic Diagnosis and Treatment in Urinary Bladder Pathology. Elsevier, 2016, pp. 1–24.
- [24] H. Lee, Y. Choi, and B.-J. Yi, “Stackable 4-bar manipulators for single port access surgery,” IEEE/ASME Transactions on Mechatronics, vol. 17, no. 1, pp. 157–166, 2011.

- [25] B. Cheon, E. Gezgin, D. K. Ji, M. Tomikawa, M. Hashizume, H.-J. Kim, and J. Hong, “A single port laparoscopic surgery robot with high force transmission and a large workspace,” Surgical endoscopy, vol. 28, no. 9, pp. 2719–2729, 2014.
- [26] D. R. Hickling, T.-T. Sun, and X.-R. Wu, “Anatomy and physiology of the urinary tract: relation to host defense and microbial infection,” Urinary tract infections: Molecular pathogenesis and clinical management, pp. 1–25, 2017.
- [27] Overactive bladder. [Online]. Available: <https://www.urologygroupvirginia.com/urologic-care/incontinence/overactive-bladder-sensory-urgency>
- [28] N. Simaan, R. M. Yasin, and L. Wang, “Medical technologies and challenges of robot-assisted minimally invasive intervention and diagnostics,” Annual Review of Control, Robotics, and Autonomous Systems, vol. 1, pp. 465–490, 2018.
- [29] Y. Zhong, L. Hu, and Y. Xu, “Recent advances in design and actuation of continuum robots for medical applications,” in Actuators, vol. 9, no. 4. MDPI, 2020, p. 142.
- [30] J. Burgner-Kahrs, D. C. Rucker, and H. Choset, “Continuum robots for medical applications: A survey,” IEEE Transactions on Robotics, vol. 31, no. 6, pp. 1261–1280, 2015.
- [31] Z. Li, L. Wang, L. Wu, F. Alambeigi, and S. S. Cheng, “Flexible surgical robotics: Design, modeling, sensing and control,” Frontiers in Robotics and AI, vol. 9, 2022.
- [32] Y. Goergen, R. Chadda, R. Britz, D. Scholtes, N. Koev, P. Motzki, R. Werthschützky, M. Kupnik, and S. Seelecke, “Shape memory alloys in continuum and soft robotic applications,” in Smart Materials, Adaptive Structures and Intelligent Systems, vol. 59131. American Society of Mechanical Engineers, 2019, p. V001T04A014.

- [33] N. Simaan, K. Xu, W. Wei, A. Kapoor, P. Kazanzides, R. Taylor, and P. Flint, “Design and integration of a telerobotic system for minimally invasive surgery of the throat,” The International journal of robotics research, vol. 28, no. 9, pp. 1134–1153, 2009.
- [34] J. Zhang, Q. Fang, P. Xiang, D. Sun, Y. Xue, R. Jin, K. Qiu, R. Xiong, Y. Wang, and H. Lu, “A survey on design, actuation, modeling, and control of continuum robot,” Cyborg and Bionic Systems, vol. 2022, 2022.
- [35] S. Li and G. Hao, “Current trends and prospects in compliant continuum robots: A survey,” in Actuators, vol. 10, no. 7. MDPI, 2021, p. 145.
- [36] L. Blanc, A. Delchambre, and P. Lambert, “Flexible medical devices: Review of controllable stiffness solutions,” in Actuators, vol. 6, no. 3. MDPI, 2017, p. 23.
- [37] A. Stilli, H. A. Wurdemann, and K. Althoefer, “A novel concept for safe, stiffness-controllable robot links,” Soft robotics, vol. 4, no. 1, pp. 16–22, 2017.
- [38] A. S. Huan, W. Xu, and H. Ren, “Investigation of a stiffness varying mechanism for flexible robotic system,” in 2016 IEEE International Conference on Mechatronics and Automation. IEEE, 2016, pp. 828–833.
- [39] A. Jiang, G. Xynogalas, P. Dasgupta, K. Althoefer, and T. Nanayakkara, “Design of a variable stiffness flexible manipulator with composite granular jamming and membrane coupling,” in 2012 IEEE/RSJ International Conference on Intelligent Robots and Systems. IEEE, 2012, pp. 2922–2927.
- [40] P. Dario, M. C. Carrozza, M. Marcacci, S. D’Attanasio, B. Magnani, O. Tonet, and G. Megali, “A novel mechatronic tool for computer-assisted arthroscopy,” IEEE

transactions on information technology in biomedicine, vol. 4, no. 1, pp. 15–29, 2000.

- [41] M. D. Kutzer, S. M. Segreti, C. Y. Brown, M. Armand, R. H. Taylor, and S. C. Mears, “Design of a new cable-driven manipulator with a large open lumen: Preliminary applications in the minimally-invasive removal of osteolysis,” in 2011 IEEE International Conference on Robotics and Automation. IEEE, 2011, pp. 2913–2920.
- [42] D. B. Camarillo, C. F. Milne, C. R. Carlson, M. R. Zinn, and J. K. Salisbury, “Mechanics modeling of tendon-driven continuum manipulators,” IEEE transactions on robotics, vol. 24, no. 6, pp. 1262–1273, 2008.
- [43] H.-S. Yoon and B.-J. Yi, “A 4-dof flexible continuum robot using a spring backbone,” in 2009 International Conference on Mechatronics and Automation. IEEE, 2009, pp. 1249–1254.
- [44] W. S. Rone and P. Ben-Tzvi, “Mechanics modeling of multisegment rod-driven continuum robots,” Journal of Mechanisms and Robotics, vol. 6, no. 4, p. 041006, 2014.
- [45] Y. Ganji, F. Janabi-Sharifi, et al., “Catheter kinematics for intracardiac navigation,” IEEE Transactions on Biomedical Engineering, vol. 56, no. 3, pp. 621–632, 2009.
- [46] D. C. Rucker, R. J. Webster III, G. S. Chirikjian, and N. J. Cowan, “Equilibrium conformations of concentric-tube continuum robots,” The International journal of robotics research, vol. 29, no. 10, pp. 1263–1280, 2010.
- [47] G. S. Chirikjian and J. W. Burdick, “Kinematically optimal hyper-redundant manipulator configurations,” IEEE transactions on Robotics and Automation, vol. 11, no. 6, pp. 794–806, 1995.

- [48] J. Jung, R. S. Penning, and M. R. Zinn, “A modeling approach for robotic catheters: effects of nonlinear internal device friction,” Advanced Robotics, vol. 28, no. 8, pp. 557–572, 2014.
- [49] T. Zheng, D. T. Branson, R. Kang, M. Cianchetti, E. Guglielmino, M. Follador, G. A. Medrano-Cerda, I. S. Godage, and D. G. Caldwell, “Dynamic continuum arm model for use with underwater robotic manipulators inspired by octopus vulgaris,” in 2012 IEEE international conference on robotics and automation. IEEE, 2012, pp. 5289–5294.
- [50] K. Xu and N. Simaan, “Analytic formulation for kinematics, statics, and shape restoration of multibackbone continuum robots via elliptic integrals,” Journal of Mechanisms and Robotics, 2010.
- [51] J. P. Desai, Encyclopedia Of Medical Robotics, The (In 4 Volumes). World Scientific, 2018.
- [52] S.-J. Baek and S.-H. Kim, “Robotics in general surgery: An evidence-based review,” Asian journal of endoscopic surgery, vol. 7, no. 2, pp. 117–123, 2014.
- [53] A. Degani, H. Choset, A. Wolf, and M. A. Zenati, “Highly articulated robotic probe for minimally invasive surgery,” in Proceedings 2006 IEEE International Conference on Robotics and Automation, 2006. ICRA 2006. IEEE, 2006, pp. 4167–4172.
- [54] N. K. Ozturk and A. S. Kavakli, “Use of bladder volume measurement assessed with ultrasound to predict postoperative urinary retention,” Northern clinics of Istanbul, vol. 3, no. 3, p. 209, 2016.
- [55] R. G. Hudson, M. J. Conlin, and D. H. Bagley, “Ureteric access with flexible ureteroscopes: effect of the size of the ureteroscope,” BJU international,

vol. 95, no. 7, pp. 1043–1044, may 2005. [Online]. Available: <https://pubmed.ncbi.nlm.nih.gov/15839928/>

- [56] V. De Coninck, E. X. Keller, B. Somani, G. Giusti, S. Proietti, M. Rodriguez-Socarras, M. Rodríguez-Monsalve, S. Doizi, E. Ventimiglia, and O. Traxer, “Complications of ureteroscopy: a complete overview,” World journal of urology, vol. 38, no. 9, pp. 2147–2166, 2020.
- [57] S. K. Lildal, K. H. Andreassen, H. Jung, M. R. Pedersen, and P. J. S. Osther, “Evaluation of ureteral lesions in ureterorenoscopy: impact of access sheath use,” Scandinavian Journal of Urology, vol. 52, no. 2, pp. 157–161, 2018.
- [58] J. S. Engelsjerd and C. M. Deibert, Cystoscopy. StatPearls Publishing, Treasure Island (FL), 2022. [Online]. Available: <http://europepmc.org/books/NBK493180>
- [59] B. Siciliano, “Kinematic control of redundant robot manipulators: A tutorial,” Journal of intelligent and robotic systems, vol. 3, no. 3, pp. 201–212, 1990.
- [60] L.-T. Schreiber and C. Gosselin, “Passively driven redundant spherical joint with very large range of motion,” Journal of Mechanisms and Robotics, vol. 9, no. 3, p. 031014, 2017.
- [61] I. D. Walker, “Continuous backbone “continuum” robot manipulators,” International Scholarly Research Notices, vol. 2013, 2013.
- [62] A. Bajo and N. Simaan, “Hybrid motion/force control of multi-backbone continuum robots,” The International journal of robotics research, vol. 35, no. 4, pp. 422–434, 2016.

- [63] S. S. Kumat and P. S. Shiakolas, “Design, inverted vat photopolymerization 3d printing, and initial characterization of a miniature force sensor for localized in vivo tissue measurements,” 3D Printing in Medicine, vol. 8, no. 1, pp. 1–14, 2022.
- [64] R. H. Byrd, M. E. Hribar, and J. Nocedal, “An interior point algorithm for large-scale nonlinear programming,” SIAM Journal on Optimization, vol. 9, no. 4, pp. 877–900, 1999.
- [65] R. H. Byrd, J. C. Gilbert, and J. Nocedal, “A trust region method based on interior point techniques for nonlinear programming,” Mathematical programming, vol. 89, no. 1, pp. 149–185, 2000.
- [66] R. A. Waltz, J. L. Morales, J. Nocedal, and D. Orban, “An interior algorithm for nonlinear optimization that combines line search and trust region steps,” Mathematical programming, vol. 107, no. 3, pp. 391–408, 2006.
- [67] S. Pansart, “Prepreg processing of advanced fibre-reinforced polymer (FRP) composites,” Advanced Fibre-Reinforced Polymer (FRP) Composites for Structural Applications, pp. 125–154, jan 2013.
- [68] P. S. Shiakolas, K. L. Conrad, and T. Yih, “On the accuracy, repeatability, and degree of influence of kinematics parameters for industrial robots,” International journal of modelling and simulation, vol. 22, no. 4, pp. 245–254, 2002.
- [69] R. Paul and S. Anand, “Optimal part orientation in rapid manufacturing process for achieving geometric tolerances,” Journal of Manufacturing Systems, vol. 30, no. 4, pp. 214–222, 2011.

- [70] F. P. Melchels, J. Feijen, and D. W. Grijpma, “A review on stereolithography and its applications in biomedical engineering,” Biomaterials, vol. 31, no. 24, pp. 6121–6130, 2010.
- [71] 3d printing of medical devices. [Online]. Available: <https://www.fda.gov/medical-devices/products-and-medical-procedures/3d-printing-medical-devices>
- [72] C. Guttridge, A. Shannon, A. O’Sullivan, K. J. O’Sullivan, and L. W. O’Sullivan, “Biocompatible 3d printing resins for medical applications: A review of marketed intended use, biocompatibility certification, and post-processing guidance,” Annals of 3D Printed Medicine, vol. 5, p. 100044, 2022.
- [73] The complete resin 3d printing settings guide for beginners. [Online]. Available: <https://ameralabs.com/blog/the-complete-resin-3d-printing-settings-guide-for-beginners/>
- [74] Anycubic photon s. [Online]. Available: <https://www.anycubic.com/products/anycubic-photon-s>
- [75] Compare formlabs dental 3d printer tech specs. [Online]. Available: <https://dental.formlabs.com/products/form-3b/tech-specs/>
- [76] Phenom by peopoly. [Online]. Available: <https://peopoly.net/products/phenom>
- [77] Analysis of variance table for fit regression model. [Online]. Available: <https://support.minitab.com/en-us/minitab/21/help-and-how-to/statistical-modeling/regression/how-to/fit-regression-model/interpret-the-results/all-statistics-and-graphs/analysis-of-variance-table/>
- [78] T. Sellke, M. Bayarri, and J. O. Berger, “Calibration of  $\rho$  values for testing precise null hypotheses,” The American Statistician, vol. 55, no. 1, pp. 62–71, 2001.



- [79] Understanding hypothesis tests: Significance levels (alpha) and p values in statistics. [Online]. Available: <https://blog.minitab.com/en/adventures-in-statistics-2/understanding-hypothesis-tests-significance-levels-alpha-and-p-values-in-statistics>
- [80] Create a main effects plot. [Online]. Available: <https://support.minitab.com/en-us/minitab/21/help-and-how-to/statistical-modeling/anova/how-to/main-effects-plot/perform-the-analysis/create-the-graph/>
- [81] S. Schricker, “Composite resin polymerization and relevant parameters,” Orthodontic Applications of Biomaterials, pp. 153–170, 2017.
- [82] H. Nagem Filho, H. D. Nagem, P. A. S. Francisconi, E. B. Franco, R. F. L. Mondelli, and K. Q. Coutinho, “Volumetric polymerization shrinkage of contemporary composite resins,” Journal of Applied Oral Science, vol. 15, pp. 448–452, 2007.
- [83] How long does it take to cure resin 3d prints? [Online]. Available: <https://3dprinterly.com/how-long-does-it-take-to-cure-resin-3d-prints/#:~:text=Depending%20on%20what%20method%20and,rays%20penetrate%20the%20resin%20better.>
- [84] J. J. Craig, Introduction to robotics: mechanics and control. Pearson Educacion, 2005.
- [85] A. Klimchik, “Enhanced stiffness modeling of serial and parallel manipulators for robotic-based processing of high performance materials,” Ph.D. dissertation, Ecole Centrale de Nantes (ECN); Ecole des Mines de Nantes, 2011.
- [86] Encoder resolution, encoder accuracy & repeatability. [Online]. Available: [https://www.dynapar.com/knowledge/encoder\\_resolution\\_encoder\\_accuracy\\_repeatability/](https://www.dynapar.com/knowledge/encoder_resolution_encoder_accuracy_repeatability/)

- [87] Introduction to accuracy and repeatability in linear motion systems. [Online]. Available: <https://www.tolomatic.com/info-center/resource-details/accuracy-repeatability-linear-motion-systems/>
- [88] M. W. Spong, S. Hutchinson, and M. Vidyasagar, Robot modeling and control. John Wiley & Sons, 2020.
- [89] D. N. Nenchev, A. Goswami, and P. Vadakkepat, “Differential kinematics,” in Humanoid Robotics: A Reference. Springer, 2018, pp. 1–47.
- [90] S. R. Buss, “Introduction to inverse kinematics with jacobian transpose, pseudoinverse and damped least squares methods,” IEEE Journal of Robotics and Automation, vol. 17, no. 1-19, p. 16, 2004.
- [91] T. Yoshikawa, “Manipulability of robotic mechanisms,” The international journal of Robotics Research, vol. 4, no. 2, pp. 3–9, 1985.
- [92] J. Villalobos, I. Y. Sanchez, and F. Martell, “Singularity analysis and complete methods to compute the inverse kinematics for a 6-dof ur/tm-type robot,” Robotics, vol. 11, no. 6, p. 137, 2022.
- [93] L. Miteva, G. Pavlova, R. Trifonov, and K. Yovchev, “Manipulability analysis of redundant robotic manipulator,” in Proceedings of the 21st International Conference on Computer Systems and Technologies, 2020, pp. 135–140.
- [94] K. M. Lynch and F. C. Park, Modern robotics. Cambridge University Press, 2017.
- [95] L. Rozo, N. Jaquier, S. Calinon, and D. G. Caldwell, “Learning manipulability ellipsoids for task compatibility in robot manipulation,” in 2017 IEEE/RSJ International Conference on Intelligent Robots and Systems (IROS). IEEE, 2017, pp. 3183–3189.

- [96] R. W. Ogden, Non-linear elastic deformations. Courier Corporation, 1997.
- [97] L. G. Treloar, The physics of rubber elasticity. OUP Oxford, 1975.
- [98] P. Polygerinos, Z. Wang, J. T. Overvelde, K. C. Galloway, R. J. Wood, K. Bertoldi, and C. J. Walsh, “Modeling of soft fiber-reinforced bending actuators,” IEEE Transactions on Robotics, vol. 31, no. 3, pp. 778–789, 2015.
- [99] R. S. Rivlin and D. Saunders, “Large elastic deformations of isotropic materials,” in Collected papers of RS Rivlin. Springer, 1997, pp. 157–194.
- [100] Properties: Silicone rubber. [Online]. Available: <https://www.azom.com/properties.aspx?ArticleID=920>
- [101] M. K. Wadee, M. A. Wadee, A. P. Bassom, and A. A. Aigner, “Longitudinally inhomogeneous deformation patterns in isotropic tubes under pure bending,” Proceedings of the Royal Society A: Mathematical, Physical and Engineering Sciences, vol. 462, no. 2067, pp. 817–838, 2006.
- [102] J. M. Rotter, A. J. Sadowski, and L. Chen, “Nonlinear stability of thin elastic cylinders of different length under global bending,” International Journal of Solids and Structures, vol. 51, no. 15-16, pp. 2826–2839, 2014.
- [103] J. J. Cervantes-Sánchez, J. M. Rico-Martínez, S. Pacheco-Gutiérrez, and G. Cerdilla-Villafaña, “Static analysis of spatial parallel manipulators by means of the principle of virtual work,” Robotics and Computer-Integrated Manufacturing, vol. 28, no. 3, pp. 385–401, 2012.
- [104] C. Lanczos, The variational principles of mechanics. Courier Corporation, 2012.

- [105] S. Adejokun, S. Kumat, and P. Shiakolas, “A microrobot with an attached micro-force sensor for natural orifice access to the bladder interior wall,” Presented ASME International Mechanical Engineering Congress and Exposition, 10 2022.
- [106] H. Akima, “A method of bivariate interpolation and smooth surface fitting for irregularly distributed data points,” ACM Transactions on Mathematical Software (TOMS), vol. 4, no. 2, pp. 148–159, 1978.
- [107] H. Heinzl and M. Mittlböck, “Adjusted  $r^2$  measures for the inverse gaussian regression model,” Computational Statistics, vol. 17, no. 4, pp. 525–544, 2002.

## BIOGRAPHICAL STATEMENT

Samson Adejokun received a bachelor's degree from Ajayi Crowther University (ACU), Nigeria in 2011. He graduates with a First class in Physics with Electronics. In 2013, he received a master's degree in Robotics from King's College London. While at King's, Samson researched soft robotic actuators with variable stiffness for minimally invasive surgery. Samson joined the University of Texas at Arlington (UTA) in 2015 and has continued to focus his research interest on the medical application of robots. He worked as a graduate teaching assistant for the Measurement and Instrumentation II lab at UTA from 2016-2023. Samson has also worked as a robotics research intern at the University of Texas Arlington Research Institute (UTARI) where he was involved in developing soft pneumatic actuators and a robotic rehab glove for applications in rehabilitative and assistive medical care. Samson currently has several years of electro-mechanical engineering experience and in future plans to pursue a career in robotics research and development.